SAW PROPAGATION AND DEVICE MODELLING ON ARBITRARILY ORIENTED SUBSTRATES

Maurício Pereira da Cunha
B. Eng., M. Eng. (University of São Paulo, Brazil)

Department of Electrical Engineering
McGill University, Montreal

A Thesis submitted to the Faculty of Graduate Studies and Research
in partial fulfilment of the requirements of the degree of
Doctor of Philosophy

July, 1994

ISBN 0-612-00123-7

ABSTRACT

A detailed theoretical analysis is presented for calculating the surface acoustic wave (SAW) reflection coefficient of thin metallic layers. Based on this analysis, directions of propagation are classified as symmetric or asymmetric. An augmented scalar transmission line circuit model which contains a new lumped network element that accounts for asymmetry is introduced to describe SAW reflection and transmission through a strip. The resulting network model is used to analyze grating and transducer structures. Computed results based on this new network model are in excellent agreement with measured data, not only on devices oriented along symmetric directions, but also on devices which exhibit directivity due to asymmetric orientations. A simple procedure, based on physical arguments, is outlined for the identification of high directivity orientations. An algebraic construction is given which demonstrates that the coupling-of-modes (COM) modelling of gratings and transducers is derivable from the new network model. Approximate explicit analytical expressions, in terms of the network model, are given for the COM model parameters. The properties of pseudo-surface-waves are re-examined and a new high-velocity pseudo-surface acoustic wave (HVPSAW) is described. It is shown that this mode, not referenced in the SAW device literature, has a low attenuation along certain directions, and is thus very attractive for high-frequency low-loss SAW devices.

RÉSUMÉ

Cette thèse présente une analyse théorique détaillée pour le calcul du coefficient de réflexion d'onde acoustique de surface (OAS) de couches métalliques minces. En se fondant sur cette analyse, on classe les directions de propagation en direction symétrique et direction asymétrique. Un modèle scalaire augmenté de circuit de ligne de transmission qui contient un nouvel élément de réseau localisé rendant compte de l'asymétrie est introduit afin de décrire la réflexion et la transmission de l'OAS à travers une bande métallique. Le modèle de réseau ainsi obtenu est utilisé pour analyser des structures de treillis et de transducteur. Les résultats calculés à l'aide de ce nouveau modèle de réseau présentent un haut degré de concordance avec les données mesurées, non seulement pour des dispositifs orientés le long d'axes symétriques, mais également pour des dispositifs qui présentent une directivité due à une orientation asymétrique. Un procédé simple, fondé sur des arguments physiques, est proposé pour l'identification d'orientations à haute directivité. Une construction algébrique est donnée, qui démontre que la modélisation par couplage de mode (CM) de treillis et de transducteurs est dérivable à partir du nouveau modèle de réseau. Des expressions analytiques explicites approximatives par rapport au modèle de réseau sont données pour les paramètres de modèle CM. Les propriétés d'ondes pseudo-superficielles sont réexaminées et une nouvelle onde acoustique pseudo-superficielle à haute vélocité (OAPSHV) est décrite. L'auteur démontre que ce mode, dont il n'est pas fait mention dans les publications sur les OAS, présente une faible atténuation le long de certains axes, ce qui le rend très attrayant pour des dispositifs à OAS à faible perte et haute fréquence.

ACKNOWLEDGEMENTS

I wish to express my sincere gratitude to Prof. Eric Adler, my thesis supervisor, for his encouragement, guidance, and patience throughout the course of this research.

In addition, I would like to thank Professors G. W. Farnell, O. Schwelb, P. P. Silvester, and J. P. Webb for the many fruitful discussions.

I am indebted to the Electrical Engineering Department for the technical support provided. In particular I have to extend my thanks to Jacek Slaboszewicz and Carl Jorgensen for their assistance with computer systems, and Kezia Cheng and Guy Rodrigue for their assistance in fabricating some of the test devices.

On a personal note, I have to acknowledge the infinite patience, comprehension, and support that I have received from my wife, Alessandra, and from my parents, José and Marilda, to whom I dedicate this thesis.

The financial assistance from Conselho Nacional de Desenvolvimento Científico e Tecnológico (CNPq), and from the Natural Sciences and Engineering Research Council of Canada is also gratefully acknowledged.

TABLE OF CONTENTS

CHAPTER 1 INTRODUCTION 1

CHAPTER 2 STRIP AND STEP DISCONTINUITIES ON THE MATERIAL SURFACE 8

2.1 Introduction 8

2.2 The Discontinuity Concept and Structures 10

2.3 The Reciprocity Relation and the Reflection Coefficient 13

2.4 Evaluating the Reflections Coefficient, Γ_{strip} 14

2.5 The Perturbation Theory Approach 17

2.6 Arbitrary Orientations 20

2.6.1 Forward orientations 22

2.6.2 Backward orientations 24

2.7 Network Model Representation and Arbitrary Orientations 26

2.7.1 Symmetric orientations 26

2.7.2 Asymmetric orientations 29

2.8 Mode-Matching Method (MMM) 32

2.9 Numerical Results 34

2.10 Summary and Concluding Remarks 47

CHAPTER 3 THE SHORT-CIRCUITED GRATING 48

3.1 Introduction 48

3.2 The Structure and the Respective Network Model 49

3.3 Differential Description 53
3.4 Review of the COM Approach 55
3.5 Solution to the COM Equation 58
3.6 Determination of k_{11} and k_{12} 60
3.7 Extension of the Farnell (GWF) Approximation 61
3.8 Comparison of Different Methods 64
3.8.1 Comparison of different methods 64
3.8.2 Frequency responses for the COM parameters 72
3.9 Summary and Concluding Remarks 77

CHAPTER 4 ARBITRARILY ORIENTED INTERDIGITAL TRANDUCER ... 79
4.1 Introduction 79
4.2 The Interdigital Transducer - Initial Considerations 80
4.3 The Regular IDT 81
4.4 The Split-Finger IDT 84
4.5 Some IDT Characteristics 84
4.6 High Directivity (NSPUDT) Orientations 88
4.7 The COM Description 92
4.8 First-Order Approximations 97
4.8.1 Approximate network model parameters 97
4.8.2 Approximate COM parameters 97
4.9 A Delay Line on Arbitrary Orientations 98
4.10 Open-Circuited Gratings 101
4.10.1 Network Model 101
4.10.2.Coupling-of-Modes 101
4.11 Numerical and Experimental Results 103

4.11.1 Comparison with COM, approximate model,
and published experiments 104
4.11.2 Other regular IDT delay lines:
comparison with measured data 110
4.11.3 Some numerical results for NSPUDT search orientations 111
4.12 Summary and Concluding Remarks 116

CHAPTER 5 SAW, PSAW, AND A NEW HIGH VELOCITY PSAW MODE 118
5.1 Introduction 118
5.2 Pseudo-SAW Solutions 119
5.3 Numerical and Experimental Discussion 120
5.4 MMM2 140
5.5 Summary and Concluding Remarks 143

CHAPTER 6 SUMMARY AND CONCLUSIONS 145

APPENDIX I 149

APPENDIX II 155

REFERENCES 156

LIST OF FIGURES

Fig. 2.1 Strip discontinuity structure. 11

Fig. 2.2 Step discontinuity structure. 12

Fig. 2.3 Forward and backward incident SAW. 21

Fig. 2.4 Particle displacement motion (included in the figure is the equation of an ellipse for a sagittally polarized wave): a) symmetric orientations; b) asymmetric orientations. 25

Fig. 2.5 Scalar network transmission line model: a) impedance discontinuities; b) inclusion of B_e. 27

Fig. 2.6 Scalar network model: a) introduction a new network element B_r to account for bilateral asymmetry; b) B_e included. 31

Fig. 2.7 Magnitude of the normal stress components versus normalised thickness: T'_{xz} (solid curve), T'_{yz} (dashdot curve), T'_{zz} (dashed curve), Perturbation Theory (dotted curves). 36

Fig. 2.8 Magnitude of the propagation direction stress components versus normalised thickness: T'_{xx} (solid curve), T'_{xy} (dashdot curve), T'_{xz} (dashed curve), Perturbation Theory T'_{xx} (dotted curve). 37

Fig. 2.9 Magnitude of the particle velocity field components: v_x (solid curve), v_y (dashdot curve), v_z (dashed curve). 38

Fig. 2.10 Reflection coefficient, Γ_u , magnitude and phase: non-perturbation theory (RRM, (2.9), solid curves); perturbation theory ((2.16), dashed curves). 40

Fig. 2.11 Reflection coefficient magnitude and phase: non-perturbation theory (RRM, (2.9), solid curves); without the δ-function contribution (dashed curves); δ-function contribution alone (circles); and mode-matching method (dashdot curves). 41

Fig. 2.12 Reflection coefficient magnitude (2.9) (solid curve); and including the effect of energy storage, (2.9) for quartz, (Euler angles: [0° 132.75° 25°]) (dashed curve), and (2.9) for quartz in the reverse direction, (Euler angles: [0° 132.75° -155°]) (dashdot curve). 44

Fig. 3.1 a) Short - circuited SAW grating structure; b) Scalar model for the arbitrarily oriented short - circuited grating cell. 50

Fig. 3.2 Calculated a) magnitude and b) phase of S_{11}; network model (solid curve), COM (ooo), and GWF model (+++). 66

Fig. 3.3 Calculated a) magnitude and b) phase of S_{21}; network model (solid curve), COM (ooo), and GWF model (+++). 67

Fig. 3.4 Forward ($\bar{R}$) and backward ($\bar{S}$) wave amplitudes as a function of position, at f_n=0.998, with the incident forward wave amplitude normalized so that it carries unit power; network model (solid curve), COM (ooo curve), and GWF model (+++ curve). 68

Fig. 3.5 Net forward power, $|\bar{R}|^2$-$|\bar{S}|^2$, in the short-circuited grating as a function of position (incident forward wave amplitude normalized so that it carries unit power); network model (solid curve) COM model (ooo curve), and GWF (+++ curve). 69

Fig. 3.6 Percentage differences, over 30% frequency band with respect to network model, for the magnitude of the calculated differences with the COM model (solid curve) and the GWF model (broken curve). 70

Fig. 3.7 Same as Fig. 3.6, but shown over a 6% frequency band. 71

Fig. 3.8 Comparison of $k_{11}.p$ calculated from the network model (solid curve) and from a corrected version of formula given in [31] as deduced from the GWF approximation (broken curve). 74

Fig. 3.9 a) Re{$k_{12}.p$} calculated from the network model (solid curve), the formula given in [31] (dashdot curve), and the formula obtained by extending the GWF approach (dashed curve); b) Im{$k_{12}.p$} from the network model (solid curve) and the corrected version of the formula given in [31] (dashed curve). 75

Fig. 3.10 Quartz ST-X: k_{12} is pure real; network model (solid curve), the formula given in [31] (dashdot curve), and the formula obtained by extending the GWF approach, (dashed curve). 76

Fig. 4.1 Regular IDT structure and the corresponding network model for a positive polarity half-period cell. 82

Fig. 4.2 Split-finger IDT structure and the corresponding network model for a positive polarity half-period cell. 85

Fig. 4.3 a) IDT as a three port device; b) absorption of the acoustic port 1; c) absorption of the acoustic port 2; d) two port representation which results from the absorption of one acoustic port. 86

Fig. 4.4 Locations of reflections due to discontinuities in the IDT structure (energy storage effect neglected in this figure). 89

Fig. 4.5 a) Regular two-port one-pole resonator; b) Synchronous placement of the IDTs and standing wave diagram; c) standing wave diagram for asynchronous placement of the IDTs; d) NSPUDT resonator structure [66]. 93

Fig. 4.6 Coupling-of-modes (COM) variables for the IDT structure. 96

Fig. 4.7 Transmission matrix blocks used for constructing a SAW delay line. 100

Fig. 4.8 IDT electrical to mechanical insertion loss for both the network model (solid curve) and the COM description (ooo curve); a) forward propagation direction; b) reverse propagation direction. 105

Fig. 4.9 IDT electrical to mechanical insertion loss using full network model (solid curve) and the approximate network model parameters (ooo points); a) forward propagation direction; reverse propagation direction. 105

Fig. 4.10 Directivity plot for the IDT structure; network model (solid curve) and experimental results (ooo points). 107

Fig. 4.11 IDT input admittance: network model (solid curves), experimental result (ooo points), network model plus typical parasitic circuit (broken curves). 108

Fig. 4.12 Delay line insertion loss for both propagation directions: a) forward and b) reverse (positions of split-finger IDT interchanged); network model (solid curves) and experimental results (ooo points). 109

Fig. 4.13 Predicted delay line insertion loss versus frequency (quartz ST-X). 112

Fig. 4.14 Measured delay line insertion loss versus frequency (quartz ST-X). 112

Fig. 4.15 Predicted delay line insertion loss versus frequency (quartz ST-25°). 113

Fig. 4.16 Measured delay line insertion loss versus frequency (quartz ST-25°). 113

Fig. 4.17 Predicted delay line insertion loss versus frequency (YZ $LiNbO_3$). 114

Fig. 4.18 Measured delay line insertion loss versus frequency (YZ $LiNbO_3$). 114

Fig. 5.1 Boundary function value as a function of the phase velocity, v_p, and attenuation, α, for the pseudo-SAW (PSAW) (free surface quartz, Euler angles:[0° 132.75° 25°]). 122

Fig. 5.2 Boundary function value as a function of the phase velocity, v_p, and attenuation, α, for the high velocity pseudo-SAW (HVPSAW) (aluminium layer on quartz, Euler angles:[0° 132.75° 25°]). 123

Fig. 5.3 Boundary function value as a function of the phase velocity, v_p, for the regular SAW (free surface, quartz, Euler angles:[0° 132.75° 25°]). 124

Fig. 5.4 Boundary function showing the several generalized surface wave (GSW) modes as a function of thickness x frequency (hf) for a fixed phase velocity, v_p=3.2 km/s; aluminium layer on quartz, Euler angles:[0° 132.75° 25°]. 124

Fig. 5.5 Detail near the solution region for the boundary function value as a function of the phase velocity, v_p, and attenuation, α, for the pseudo-SAW (PSAW) (free surface quartz, Euler angles:[0° 132.75° 25°]). 125

Fig. 5.6 Detail around the solution for the boundary function value as a function of the phase velocity, v_p, and attenuation, α, for the high velocity pseudo-SAW (HVPSAW) (aluminium layer on quartz, Euler angles:[0° 132.75° 25°]). 126

Fig. 5.7 Plot of the normalized effective permitivity function, $\varepsilon_{eff}/\varepsilon_o$, versus the phase velocity, v_p, (quartz, Euler angles:[0° 132.75° 25°]). 128

Fig. 5.8 Phase velocity and attenuation for the HVPSAW mode versus the angle of propagation ψ for short-circuited ST cut quartz plane (Euler angles: [0° 132.75° ψ]) (solid and **x** curves); longitudinal BAW (dashed curve). 133

Fig. 5.9 Phase velocity and attenuation versus (thickness x frequency) for an aluminum layered quartz substrate with propagation at (Euler angles: [0° 132.75° 25°]); solid: first and second generalized SAW modes; dashed: PSAW mode; dash-dot: HVPSAW mode; larger-dots: bulk acoustic wave (BAW) velocities for this orientation. 134

Fig. 5.10 Measured insertion loss frequency response plot for a quartz ST-X delay line (dimensions of the structure described in the text). 135

Fig. 5.11 Poynting vector ([TW/m^2]) in the direction of propagation versus the normalized depth inside the substrate for the pseudo-SAW (PSAW) (free surface, quartz, Euler angles: [0° 132.75° 25°], fields normalized with respect to $|u_1|=1$). .. 137

Fig. 5.12 Poynting vector ([TW/m^2]) in the direction of propagation versus the normalized depth inside the substrate for the high velocity pseudo-SAW (HVPSAW) (aluminum layered surface, h/λ_{SAW}=1%, quartz, Euler angles: [0° 132.75° 25°], fields normalized with respect to $|u_1|=1$). 137

Fig. 5.13 Measured insertion loss frequency response plot for quartz, Euler angles:[0° 132.75° 25°], delay line (dimensions of the structure described in the text). 138

Fig. 5.14 a) Receiving IDT at an offset angle with respect to the direction of propagation; b) Measured insertion loss frequency response plot on quartz, Euler angles:[0° 132.75° 25°], for the structures positioned as in a). 139

Fig. 5.15 Declination of the Poynting vector as a function of normalized depth for the high velocity pseudo-SAW (HVPSAW); aluminum layered surface, h/λ_{SAW}=1%, $Li_2B_4O_7$, Euler angles:[0° 45° 90°], fields normalized with respect to $|u_1|=1$. 141

Fig. 5.16 Declination of the Poynting vector as function of normalized depth for the high velocity pseudo-SAW (HVPSAW); aluminum layered surface, h/λ_{SAW}=1%, quartz, Euler angles:[0° 132.75° 25°], fields normalized with respect to $|u_1|=1$. 141

Fig. I.1 Structure considered and coordinate system. 151

LIST OF TABLES

2.1 Free surface SAW solutions and the reflection coefficient, Γ_u 45

5.1 Pseudo-SAW (PSAW) solution for some selected materials and orientations. . 131

5.2 High velocity pseudo-SAW (HVPSAW) solution for some selected materials and orientations. 132

CHAPTER I

INTRODUCTION

Microwave Ultrasonics, and in particular applications of surface acoustic wave (SAW) devices for communications and signal processing, is now a well-established field. A SAW is a guided wave with its associated energy concentrated within a few wavelengths of the surface, and its fields vanishing exponentially with increasing depth. The original formulation of the acoustic surface wave phenomenon was done more than one century ago by Lord Rayleigh [1], who conjectured that such Rayleigh surface waves would be especially important in seismic wave propagation because, unlike bulk acoustic waves, they would diffract on the surface, not into the volume of the earth. Lord Rayleigh's work was followed by other major contributions, such as the work of Love [2] and Stoneley [3] on the acoustic propagation in layered structures; the major interest of these works was in geophysics.

Except for ultrasonic delay lines and quartz crystal oscillators [4,5], very few applications existed during the early part of the century, most of the work remaining of academic interest only. This situation changed dramatically after 1965 when White and Voltmer [6] demonstrated that surface acoustic waves (SAW) were efficiently and selectively excited by the use of voltage-excited metal-film interdigital transducers (IDTs) deposited on the top of piezoelectric substrates. Such waves are a generalization of Rayleigh waves, in the sense that they propagate on substrates that are anisotropic and piezoelectric.

In the years that followed the demonstration of the effectiveness of the IDT in exciting SAW, very intense research work was done in investigating the nature of the surface wave propagation in isotropic, anisotropic, piezoelectric and layered media [7,8,9,10].

In parallel with the study of surface acoustic propagation, an intense activity was also aimed towards modelling the IDT, since all practical device analyses and designs depend on the IDT behaviour. Difficulties have been found with respect to the IDT modelling, since the IDT: (i.) may assume an endless variety of forms [11,12]; (ii.) SAW reflections due to electrical and mechanical loading must be accounted for in many of the required device analyses and designs; (iii.) and a variety of physical phenomena, like diffraction, other acoustic modes, electrostatic effects (as "end effects") may occur. Due to these difficulties, and whenever the application allowed, simpler IDT models have been used, like the delta-function model [13], which does not consider the three previous items mentioned. Increasing in complexity, appears the work of Smith and his colleagues [14], and the Leedom, Krimholtz, and Matthaei (KLM) model [15], which permitted the calculation of the transducer admittance, and the insertion loss for a two-transducers device. These models do not consider the effect of bulk wave generation that usually accompanies the SAW generation. The bulk wave generation was included in a more complex work by Milsom and colleagues [16], through the Green's function method, where the Green's function is derived from the effective permittivity function [16,70]. The use of the effective permittivity allows for the calculation of SAW excitation in piezoelectric materials, bulk wave generation and electrostatic effects; however the mechanical loading effect due to the finite IDT finger mass, which is very important in many devices, is excluded. Moreover all the models mentioned above assume bidirectionality, in the sense that the power generated by a symmetric IDT structure divides equally between both propagation directions. *In this thesis a new IDT network model element is devised and a scalar model created which accounts for unidirectional excitation in symmetric IDT structures.*

Although the IDTs are the most important structures in SAW devices due to the fact that they are responsible for the electrical to mechanical transduction of the signal and vice-versa, other structures exist which play relevant roles in SAW devices and which have been extensively discussed in the literature [11,70,83]. Just to mention a few of these structures: the short-circuited and open-circuited gratings, used in resonators and filters, and which are also discussed in this thesis for arbitrary directions; the multi-strip coupler and the reflecting track changer [71,72,70], used as track changers; the beamwidth compressor [73] and the strip waveguide structure [74], used for example in convolver applications.

Together with this development, many applications flourished. Initially, consumer market focused on low-cost, high volume intermediate frequency (IF) filters for domestic TV receivers. Low volume, high cost devices were usually designed for military applications [11]. From the 70's to the 80's, the spectrum of major SAW device applications for consumer, commercial, and military uses, increased rapidly, including [17]: intermediate frequency (IF) filters for a variety of applications (for instance, TV and VCR , voice and data communication equipment, satellite receivers); resonators for frequency control in oscillator applications (voltage controlled crystal oscillators in cordless phones, stable oscillators in measurement equipment such as spectrum analyzers and RF synthesizers); RF filters used as front end filters (pocket pagers, antenna duplexers); spectral shaping filters (quadrature amplitude modulation [18]); signal processing device applications (direct sequence spread spectrum convolvers, pulse expansion and compression filters for radars, programmable tapped delay lines); just to enumerate a few of the applications listed in the recent reviews [11,17].

SAW devices present several advantages. One of them is the ability of providing very complex signal processing functions in one chip, substituting an entire system or sub-system (for example, in the case of a convolver or pulse compression filter), or several inductors and capacitors in the case of a bandpass filter. Another positive aspect refers to the fact that since semiconductor technology is used, one can infer that prices will drop dramatically with large volume production. Indeed, many SAW consumer devices are sold for less than a US$1.00. In addition the technology generally permits very good reproducibility, since standard semiconductor technology is used, covering a frequency range from 10 MHz to a few GHz. Good reproducibility of SAW devices implies in a more consistent system performance. Another advantage of SAW devices are the mechanical attributes: ruggedness, light weight, and small size, which together with the previous mentioned advantages result in systems which are smaller, lighter, cheaper and consume less power.

On the other hand the technology has its shortcomings. One limitations is that

SAW devices are normally fixed from manufacturing, not allowing further simple adjustments, in a system production, for example. Designing and tooling a SAW device may be time consuming, when compared to other technologies. Another drawback is that the majority of SAW applications refer to bandpass functions due to the nature of the device. But maybe the strongest problem the technology had to face until recently was the high insertion loss ($\approx$15 to 40 dB), which has limited SAW device applications in signal processing functions in general. These points deserved and still deserve quite a lot of attention from both commercial and academic groups. Fortunately, much progress has been made in the past few years to overcome these limitations. Referring to the insertion loss, devices based on resonators have been designed which achieved insertion losses lower than 3 dB, at moderate bandwidths (<0.5%) [19], and at frequencies as high as 1.9 GHz [20]. The SAW resonator consists of two arrays of periodic reflecting structures, called gratings, on either side of a gap, which is the cavity, where the transducer structures are inserted [83,70]. Resonator based filters [75,20], for low loss ($\approx$3.4 dB), narrow bandwidth applications; the so-called Single-Phase Unidirectional Transducers (SPUDT's) [76,27,20], with insertion losses better than 6 dB, small delay distortions, good design predictions; and the Interdigitated Interdigital Transducers (IIDT's) [77,20], with enhanced power handling capabilities and insertion losses as low as 1 dB; among other structures, represent some of the positive results from the effort to overcome the insertion loss problem [20,11]. Applications of such devices are: remote control systems, like garage doors, gates, automobile locking and security systems; mobile communication and all sorts of hand held UHF transmitters and receivers; Local Area Networks (LANs); pagers; computed related items [21].

These successful results increased the applications options of SAW, allowing the technology to conquer an important place in several systems [22,23,24,21], not only in more restricted markets (telecommunications, military) but especially in the consumer market, where good profit can be made from the high volume capability of the SAW technology. However, as mentioned in [20], "further effort has to be spent on the improvement of existing SAW filters concerning lower insertion loss, reduced size, and increased stopband attenuation, and on the search of new SAW structures with the capability for these challenging specifications".

In addition to the efforts of improving the SAW device designs, quite a lot of energy has gone in the search for new materials and material orientations which have faster acoustic wave velocities. The use of pseudo-SAW waves [25], with quasi-horizontally shear polarisations, received quite a lot of attention [26,11,5], because having faster phase velocities, they allow devices to operate at frequencies 60% higher than regular SAWs for the same photolithographic requirements in fabrication. Among other desirable aspects of these modes, one can mention: high electro-mechanical coupling, temperature stable substrates, high power handling capabilities. *In this thesis a new and even higher velocity strongly longitudinally polarized pseudo-SAW mode solution is described, which may also have low propagation loss and thus have an enormous impact in still higher-frequency operating SAW devices.*

One of the structures mentioned in the previous paragraphs that has been used to reduce the insertion loss is the Single-Phase Unidirectional Transducer (SPUDT). These transducers, due to a proper geometrical design or by the use of more than one kind of metallic layer [27,20], can deliver more power in one direction with respect to the other (finite directivity), and are therefore called "unidirectional". In 1985 a very interesting alternative to the SPUDT design structures was presented by P. Wright [28]. Instead of achieving transducer unidirectionality by means of different geometrical structures or different deposited kinds of layers, the regular IDT, regarded until then in the literature as a bidirectional structure, is employed. The unidirectionality is accomplished by means of the choice of crystal cut and propagation direction. These high directivity orientations have been named NSPUDT - Natural Single Phase Unidirectional Transducer - orientations, the term "Natural" being used because the directionality effect appears as a result of the material orientation, as opposed to the device geometry or construction. The name 'NSPUDT orientation', or equivalently 'high directivity orientation', is used throughout this thesis to designate SAW propagating directions where a significantly higher amount of power is launched in one direction with respect to the other.

All the IDT network models available, some of them mentioned earlier [14,13,29], are inherently scalar approximations which model IDT structures as sections of transmission lines, coupled through a transformer to an electrical port. These models have symmetric topologies and work well along crystal directions where the SAW "behaves" identically for "forward" and "reverse" directions. In these cases the power generated divides equally between the two directions (bidirectionality). The directivity phenomenon reported in [28] cannot be accounted for with symmetric network models. The tool used to deal with this problem has been the coupling-of-modes (COM) analysis [28,31], which is a differential equation modelling description. The COM analysis is essentially phenomenological, i.e., the parameters for the COM model are usually measured. Although practical and computationally efficient, this differential model does not describe the discrete nature of the IDT structure, thus compromising the physical understanding of the directivity phenomenon observed.

A motivation for this thesis is the study of the directivity phenomenon determined by material properties, and the modelling of SAW structures oriented along directions where this phenomenon occurs. It is quite clear that an understanding of the directivity phenomenon itself is very important from both an academic and a commercial points of view. Of academic interest because a number of questions regarding the directivity phenomenon were unanswered, such as: what are the underlying physical principles that give rise to the existence of a high directivity orientation? How does that occur? For which orientations does high directivity (NSPUDT) take place? What are the material or orientation requirements? How to find NSPUDT directions with respect to maximizing the directivity in a plane? How does the geometry and the material parameters affect this phenomenon? Of commercial interest because quite a number of successful devices oriented along NSPUDT directions are being commercially exploited. Some of the available devices are low-loss resonator filters, low-loss delay lines, and notch filters [30,31,32,33,19,34].

The objectives of this thesis are the study of SAW and pseudo-SAWs along arbitrary directions, the analysis of reflectivity from thin metallic layers, and the modelling of SAW structures along arbitrary directions of propagation, thus including the high directivity orientations mentioned in the preceding paragraph.

In Chapter II an analysis for SAW reflectivity due to thin metallic films is developed based on a reciprocity relation method. From this method, an approximate perturbation equation is derived, and the limits on the validity of its approximate results are verified against the more complete analysis. In addition another method of calculating the reflectivity, namely a mode-matching technique, is introduced and its results compared to the reciprocity relation method. From this reflectivity analysis SAW directions of propagation are classified into symmetric or asymmetric types, the second including high directivity or NSPUDT orientations. Along asymmetric directions it is shown that the reflection coefficient due to the thin metallic films is not the same for incident forward and backward SAW waves. To account for this asymmetric behaviour of the reflection coefficient, a new reactive lumped network element is introduced in a scalar transmission line model.

In Chapter III a scalar model is developed for the short-circuited grating oriented along arbitrary directions. This task is accomplished by using the scalar model developed in the previous chapter to predict short-circuited grating structure responses. Developing a model for the short-circuited grating is an important step towards the scalar modelling of the arbitrarily oriented IDT, which is carried out in Chapter IV. The splitting of the treatment of short-circuited grating structures in Chapter III and IDT structures in Chapter IV is solely for clarity of presentation. The coupling-of-modes modelling of grating and transducers is shown to be derivable from the network model developed. Approximated analytical expressions in terms of the network model are also deduced which predict the dependency of the COM model parameters on frequency, material parameters, and geometry. A simple procedure is outlined for finding high directivity orientations, based on reflection arguments and on the geometric structure of the IDT.

In Chapter V SAW and pseudo-SAW waves along free and layered surfaces are investigated along arbitrary orientations. A new and even higher velocity strongly longitudinally polarised pseudo-SAW mode solution is presented, which in addition to the high velocity possesses low-loss in certain directions, thus suggesting that this mode is useful for low-loss high-operating-frequency devices.

Chapter VI concludes this thesis summarizing the main results and contributions of this work, and suggests topics to be explored for extending the research in the area.

CHAPTER II

STRIP AND STEP DISCONTINUITIES ON THE MATERIAL SURFACE

2.1 INTRODUCTION

This chapter is devoted to the study of a certain type of surface acoustic wave (SAW) perturbation, which occurs when the SAW is propagating on a free, semi-infinite piezoelectric surface, and encounters a thin metallic layer or strip in its path. The layer results in a small perturbation effect, since its thickness with respect to the wavelength herein considered is at most a few percent. The reasons to restrict the analysis to thin metallic films are:

. all structures considered in this thesis use thin metallic layers on the surfaces of piezoelectric substrates;

. in practice, SAW devices use thin metallic films, and the use of these films is sufficient to manipulate the signal;

. these layers are too thin to support higher order SAW propagating modes and they do not seem to scatter significant SAW power into bulk modes, allowing one to neglect these phenomena.

A SAW propagating in a layered region has a slightly different phase velocity, as well as a different field profile solution, as compared to the free surface acoustic wave solution. Because of these differences, a backward reflected SAW appears when a surface wave propagating in a free region meets a layer or a strip. From the forward and backward waves a reflection coefficient can be calculated, and this is the main concern in this chapter. The reason why the reflection coefficient calculation is so important is that it is a scalar quantity, and therefore it offers a suitable means of expressing the layer perturbation effect into a tractable scalar network formulation. The latter is then used in the approximate scalar network modelling of arbitrary oriented gratings and transducers in the next chapters.

Different approaches have been explored in order to determine the reflection coefficient: the use of reciprocity relations together with perturbation approximations [35], finite element method (FEM) [78], boundary element method (BEM) [79], variational formulation method [80], and phenomenological parameter fitting techniques for the COM method which relies in part on measured data [81].

In this thesis the reflection coefficient due to a metallic layer on a piezoelectric substrate is studied from two different perspectives. The first one employs the Reciprocity Relation Method (RRM) [35], to calculate the reflection coefficient of a strip using the exact fields for a layered piezoelectric. One should stress that the RRM is not a Perturbation Theory analysis. In the Perturbation Theory procedure, the fields are approximated by use of the Tiersten Boundary Conditions, the velocity fields are considered the same under free and metallized regions, and a superposition principle due to small perturbations is invoked in order to calculate independently mechanical and electrical contributions to reflectivity. None of the above mentioned approximations are invoked in the RRM analysis presented in this thesis. The second approach introduced to evaluate the reflection coefficient is a Mode-Matching Method (MMM). This technique has been extensively used successfully to solve discontinuity problems in electromagnetic waveguides, but to the best of the author's knowledge has not been applied to SAW problems.

In Section 2.2 the kind of structures and the problem analyzed in this chapter are presented. Section 2.3 reviews the reciprocity relation used in the reflection coefficient calculation for a thin metallic strip. The RRM reflection coefficient expression is evaluated for a thin metallic strip in Section 2.4, and a perturbation theory analytical equation is derived from it in Section 2.5. The impact of arbitrary orientations in both forward and backward directions is discussed in Section 2.6, where the concepts of symmetric and asymmetric orientations are introduced. In Section 2.7, the reflection coefficient calculation at arbitrary orientations is translated into a convenient scalar model description, with the inclusion of a new network element to account for asymmetry. The scalar model developed in this section constitutes the basis of the Network Model analysis carried out in the following two chapters. In Section 2.8 another technique is introduced to evaluate the reflection coefficient at a discontinuity, namely a Mode-Matching Method (MMM). Numerical results which compare the different methods (RRM, MMM, perturbation theory) and their limitations are presented in Section 2.9. In Sections 2.10 concluding remarks are given.

2.2 THE DISCONTINUITY CONCEPT AND STRUCTURES

The structures discussed in this chapter are shown in Fig. 2.1 and in Fig. 2.2. In Fig. 2.1 a thin metallic layer strip is shown on top of a semi-infinite substrate, usually piezoelectric. For convenience the coordinate system origin is in the center of the strip of width "a" and height "h". In Fig. 2.2, a thin metallic layer of height "h" is shown on top of the substrate; here the coordinate system origin is at the edge of the layer. In both Fig. 2.1 and Fig. 2.2 an incident SAW propagates in the x direction from the free region towards the perturbation.

The presence of a film covering a substrate produces a change in the SAW phase velocity and mode profiles solution when compared to the free surface solution, due to both piezoelectric shorting in the case of a metallic overlay, and to mechanical loading. As shown in Figs. 2.1 and 2.2, a SAW propagating in a free region which encounters a thin layered region will be partly reflected, due to the differences between the SAW mode solutions in the free and the layered areas mentioned before.

The position in the x direction (x=0 in Fig. 2.2) where reflections take place is referred to as a **discontinuity plane**, normal to the propagation direction, although strictly speaking there is no material discontinuity in the substrate at the start of the layered region. In regard to the structures shown in this thesis the free-to-layered transitions are considered to be abrupt.

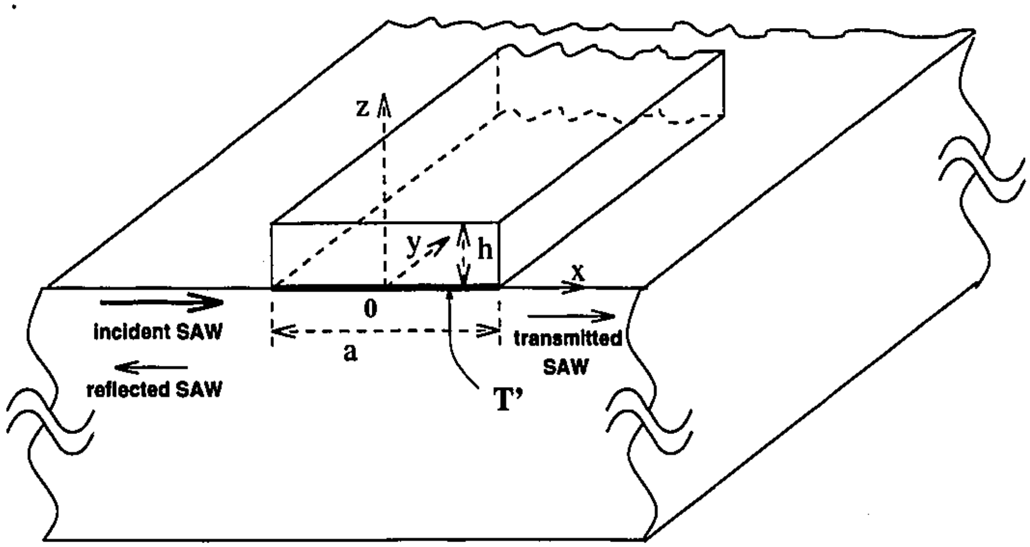

Fig. 2.1 Strip discontinuity structure.

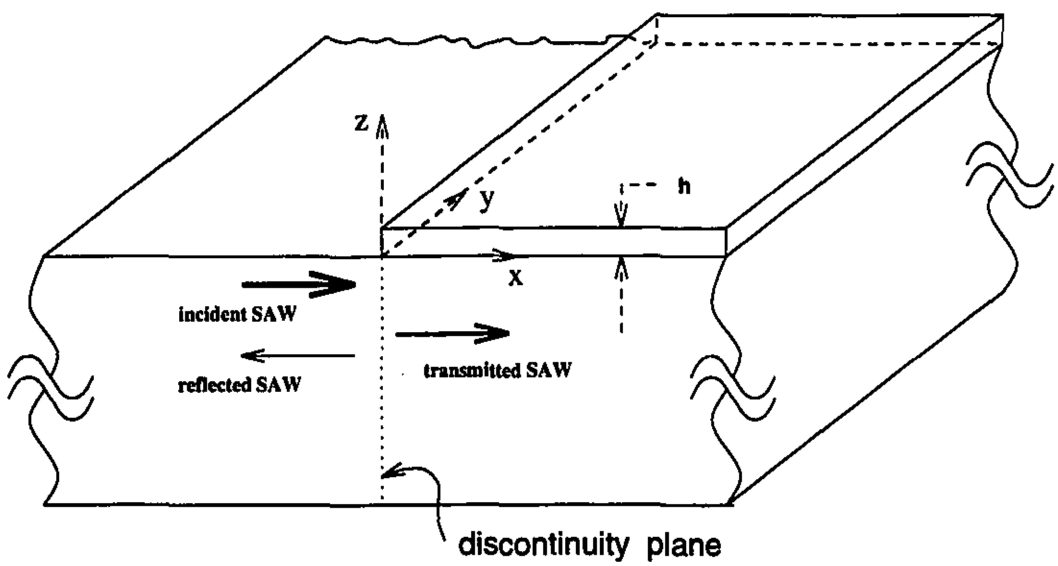

Fig. 2.2 Step discontinuity structure.

2.3 THE RECIPROCITY RELATION AND THE REFLECTION COEFFICIENT

The Reciprocity Relation applied to acoustic problems is a powerful and generic approach, which can be used in solving a variety of field problems, such as acoustic waveguide problems, scattering issues, and resonator related problems [35]. Applied to the specific scattering problem of calculating the reflection coefficient per unit width, Γ_{strip}, of a strip on a piezoelectric substrate (Fig. 2.1), the reciprocity relation approach leads to the following expression

$$\Gamma_{strip}=-\frac{1}{2}\int_{-\frac{a}{2}}^{\frac{a}{2}}(\boldsymbol{v}.\boldsymbol{T}'-\boldsymbol{v}'.\boldsymbol{T}+j\omega\phi\boldsymbol{D}'-j\omega\phi'\boldsymbol{D})\ .\ \boldsymbol{z}_1\,dx \qquad (2.1)$$

where the unprimed fields are the solutions when the strip is removed, and the primed fields are the solutions when the strip is present. In (2.1) all the field quantities are evaluated at the substrate surface (z=0), with **v** and **v'** the SAW velocity field vectors, **T** and **T'** the full stress tensors, ϕ and ϕ' the potentials, D and D' are the electric displacement vectors, and $\mathbf{z}_1$ is the unit magnitude vector in the z direction. The RMS field values in (2.1) are *normalized so that the SAW wave carries unit time-average power*. There are a few differences between (2.1) and the equivalent statement in Auld's book [35, Ch.12, pp. 304]. First there is a sign difference, which results from the derivation of (2.1) using the real reciprocity relation instead of the complex reciprocity relation, and which is missing in [35, Ch.10 ,pp. 177, immediately before eq. (10.142(a))]. Also a factor of a half is present in (2.1) instead of one fourth, due to fact that RMS fields are used.

For the unprimed solution, the normal stress term $\mathbf{T}.\mathbf{z}_1$ is zero due to the free surface boundary condition, thus simplifying (2.1) to

$$\Gamma_{strip}=-\frac{1}{2}\int_{-\frac{a}{2}}^{\frac{a}{2}}(\boldsymbol{v}.\boldsymbol{T}'+j\omega\phi\boldsymbol{D}'-j\omega\phi'\boldsymbol{D})\ .\ \boldsymbol{z}_1\,dx \tag{2.2}$$

In the case of a metallic strip, the potential $\phi'=0$, thus further simplifying (2.1) to

$$\Gamma_{strip}=-\frac{1}{2}\int_{-\frac{a}{2}}^{\frac{a}{2}}(\boldsymbol{v}.\boldsymbol{T}'+j\omega\phi\boldsymbol{D}')\ .\ \boldsymbol{z}_1\,dx \tag{2.3}$$

It is worth stressing that the above expressions (2.1) to (2.3) are not perturbation formulas. As quoted in [35, Ch.12, pp. 303], "These S-parameter formulas are exact if the exact primed and unprimed fields are used." In [35] Γ_{strip} is calculated using perturbation approximations. In the next section, a method which is not a perturbation procedure is developed to calculate (2.3). Such a method allows one to estimate the accuracy of the perturbation approximations (Sections 2.5 and 2.9).

2.4 EVALUATING THE REFLECTION COEFFICIENT, Γ_{strip}

In the preceding section, equation (2.3) for Γ_{strip} , was given. The actual evaluation of the reflection coefficient caused by the metallic strip using (2.3) requires calculating **v**, **T'.z**$_1$, ϕ and **D'.z**$_1$. The fields **v** and ϕ at z=0 are calculated numerically in a standard way for the free surface wave with phase velocity v_p, and $D'.z_1=D_3$ for the layered condition (Appendix I). Calculating **T'.z**$_1$=**T'**$_z$ (z=0), the interface stress vector, requires care. Recalling that the sinusoidal steady state dynamic equation of motion for the layer material in the absence of any external forces is ∇.**T'**=$j\omega\rho$'**v'**, with ρ' the layer material density, then for a *small* volume of the strip of height "h", one can write the *"force=(mass)x(acceleration)"* statement as

$$\int_0^h \left(\frac{\partial T'_x}{\partial x} + \frac{\partial T'_y}{\partial y} + \frac{\partial T'_z}{\partial z} \right) \delta x \delta y dz = \int_0^h \rho' j\omega \mathbf{v}' \delta x \delta y dz \qquad (2.4)$$

Since there is no variation in the y direction, $\partial/\partial y=0$, and (2.4) simplifies to

$$\int_0^h \left(\frac{\partial T'_x(x,z)}{\partial x} \right) dz - T'_z(0) = j\omega\rho' \int_0^h \mathbf{v}'(x,z)\, dz \qquad (2.5)$$

Equation (2.5), which follows directly from the dynamic equation of motion, shows that in order to calculate $\mathbf{T'}_z(z=0)$ two integrations with respect to the thickness of the layer must be performed, one of which contains the derivative of $\mathbf{T'}_x(x,z)$ with respect to x. For $|x| < a/2$, $\mathbf{T'}_x(x,z)$ is approximated by its value for an infinitely layered substrate in the same way $\mathbf{D'}.\mathbf{z}_1=D_3$ is calculated. However at the very ends of the strip in the x direction, $\mathbf{T'}_x(x,z)$ must vanish. If the correct functional variation of $\mathbf{T'}_x(x,z)$ with x were known, then the derivative with respect to x in (2.5) could be calculated precisely. Approximating $\mathbf{T'}_x(x,z)$ by the infinitely layered solution **and** saying that it goes to zero abruptly at the strip edges, is equivalent to the step functional form for $\mathbf{T'}_x(x,z)$ as

$$T'_x(x,z) = \{\overline{T}_x(z) \,.\, \exp(-j\beta' x)\}.\{u(x+\tfrac{a}{2}) - u(x-\tfrac{a}{2})\} \qquad (2.6)$$

with u(x-a/2) and u(x-a/2) describing the step variation of $\mathbf{T'}_x(x,z)$ at the strip edges, $\beta'=\omega/v'_p$, and

$$\overline{T}_x(z) = \mathbf{p}_L \,.\, \exp(j\omega \mathbf{A}_L z) \,.\, \tau(0) \qquad (2.7)$$

$\mathbf{p}_L$, $\mathbf{A}_L$ are matrices uniquely determined by the layer material properties and v'_p, and $\tau(0)$ is the vector of field components which must be continuous at the interfaces (Appendix I).

Differentiating (2.7) gives

$$\frac{\partial \boldsymbol{T}'_z(x,z)}{\partial x} = \overline{\boldsymbol{T}}_z(z)\,.\{-j\beta'[u(x+\frac{a}{2})-u(x-\frac{a}{2})]+ \\ +[\delta(x+\frac{a}{2})-\delta(x-\frac{a}{2})]\}.\exp(-j\beta' x) \tag{2.8}$$

in which two delta function terms appear at the strip edges, as a result of the differentiation of the step functions. Substituting (2.8) in (2.5), and noting that **v'** is given by the last three elements of $\exp(j\omega A_L z).\tau(0)$ for a non-piezoelectric layer (Appendix I), the required integrations with respect to the layer thickness in (2.5) are performed and the surface traction force $\mathbf{T'}_z(z=0)$ obtained. With these vectors all the information for calculating (2.3) is known. In addition Γ_{strip} is expressible in terms of the reflection at an upstep discontinuity alone, Γ_u, with the strip upstep as the phase reference. This is given by $\Gamma_{strip}=j2\Gamma_u\sin(\beta' a)$, where the propagation constants for the free and for the layered regions have been assumed to be approximately equal, $\beta' \approx \omega/v_p$. The expression for the upstep reflection coefficient, Γ_u, is then formally given by

$$\Gamma_u = j\frac{v_p}{4\omega}\,(\tau_v)_{free}\,.\,(\tau_n)_{layer} \\ -\frac{1}{2}\{\,[\tau_v(1:3)]_{free}\,.\,\boldsymbol{p}_L\,.\,(j\omega\boldsymbol{A}_L)^{-1}\,.\,[\exp(j2\pi v_p\boldsymbol{A}_L\frac{h}{\lambda})-I]\,.\,\tau(0)\} \tag{2.9}$$

where $\tau_v=[\mathbf{v}\ \ j\omega\phi]^t$ at z=0 for a free surface, and $\tau_n=[\mathbf{T}_z\ \ D_3]^t$ at z=0 for an infinitely layered surface. Since matrices $\mathbf{p}_L$ and $\mathbf{A}_L$ are solely determined by the material layer properties and v'_p, (2.9) is valid for any arbitrary anisotropic layer material. Also, since in evaluating (2.9) the exact z dependency is taken into account in all the fields required, this equation is valid for any thickness. Expression (2.9) is referred to in this work as the Reciprocity Relation Method (RRM) reflection coefficient for a thin metallic upstep [36]. When a -> 0, Γ_{strip} in (2.3) also goes to zero, and so does Γ_u .

Expanding the exponential matrix in (2.7) $\exp\{j2\pi v_p\mathbf{A}_L(h/\lambda)\}$ as a power series in

(h/λ), yields a power series for any of the fields of interest. The Tiersten boundary condition approximation [37] for a thin layer is easily derived by retaining only terms linear in (h/λ). The Tiersten boundary condition, together with the added approximation that $\mathbf{v}'=\mathbf{v}$, constitutes the basis of the perturbation theory approach [35]. In reference [35] the additional simplification of ignoring the electrical perturbation in evaluating the mechanical perturbation and vice-versa is used; the argument being that small perturbations are additive. None of the above perturbation theory assumptions are present in (2.9).

2.5 THE PERTURBATION THEORY APPROACH

First order perturbations analyses for the reflection coefficient have been developed by Datta and Hunsinger [38] for non-piezoelectric materials, and extended by Auld [35] to include piezoelectricity. In this section an approximate expression for the reflection coefficient is derived from (2.9), using the perturbation theory approach. In spite of the many approximations in the perturbation method, and which were briefly mentioned at the end of the previous section, the simplified approximate expression obtained has the merit of permitting an easy identification of orientations where the directivity phenomenon may occur. This feature is developed in the next section.

Carrying out the perturbation theory procedure in this case, requires finding approximations to the fields $\mathbf{v}'$, $\mathbf{T}'_z$, and D'_3. The first perturbation approximation is that the fields $\mathbf{v}'$ and $\mathbf{v}$ are made equal, based on the a priori assumption that the reflection coefficient for a thin metallic layer is small [35]. The second calculation to be done is that of finding an approximate T'_z. For a non-piezoelectric layer the exponential matrix $\exp\{j\omega A_L h\}$ is expanded as a power series in h

$$\exp\{\pm j\omega \boldsymbol{A}_L h\} = \boldsymbol{I}_6 + (\pm j\omega \boldsymbol{A}_L h) + (\pm j\omega \boldsymbol{A}_L h)^2 + \ldots \qquad (2.10)$$

Recalling that the field solution in the layer is given by $\tau(z)=\exp(j\omega A_L z).\tau(0)$ (Appendix I), one has that $\tau(0)=\exp(-j\omega A_L h).\tau(h)$, and using (2.10) for this last exponential and retention of the linear term only

$$\tau(0) = \begin{bmatrix} T_z'(z=0) \\ v_z'(z=0) \end{bmatrix} \approx \begin{bmatrix} I_3.T_z'(z=h) - j\omega h A_L(1{:}3,4{:}6).v'(z=0) \\ I_3.v_z'(z=h) - j\omega h A_L(1{:}3,4{:}6).v'(z=0) \end{bmatrix} \qquad (2.11)$$

with

$$A_L(1{:}3,4{:}6) = \rho' I_3 - \frac{\Gamma_T}{v_p^2} \qquad (2.12a)$$

and

$$\Gamma_T = \Gamma^{11} - \Gamma^{13} X \Gamma^{31} \qquad (2.12b)$$

Γ^{11}, Γ^{13}, **X**, and Γ^{31} as defined in the Appendix I. In (2.11) and (2.12), the Matlab software matrix notation is adopted, with $A_L(1{:}3,4{:}6)$ meaning the matrix which contains the first to third rows of A_L and the fourth to sixth columns of A_L . Actually (2.11) allows one to note that to the zero order approximation $v'(z=0) \approx v'_z(z=h)$, although the argument that $v'=v$ made above is even stronger. Noting also that $T'_z(z=h)\equiv 0$ due to the free boundary conditions, $\mathbf{T'}_z(z=0)$ is finally approximated by

$$T_z'(z=0) \approx -j\omega h\left[\rho' I_3 - \frac{\Gamma_T}{v_p^2}\right].v \qquad (2.13)$$

Equation (2.13) is exactly the *Tiersten Boundary Condition* generalized to any anisotropic non-piezoelectric layer [37,35]. It is interesting to point out that the matrix method (Appendix I) does provide a straightforward way of performing this derivation. The analytical evaluation of the term $\Gamma_T = \Gamma^{11} - \Gamma^{13} X \Gamma^{31}$ is easily obtained for an isotropic layer, but is somewhat more difficult for the case of an arbitrary anisotropic overlay. Using commercially available software the task is considerably simplified, and for an anisotropic overlay the resulting Γ_{Taniso} is given in Appendix II. For an isotropic layer one obtains

$$\Gamma_{Tiso} = \begin{bmatrix} \frac{4\mu'(\lambda'+\mu')}{(\lambda'+2\mu')} & 0 & 0 \\ 0 & \mu' & 0 \\ 0 & 0 & 0 \end{bmatrix} = \begin{bmatrix} \alpha_x' & 0 & 0 \\ 0 & \alpha_y' & 0 \\ 0 & 0 & 0 \end{bmatrix} \qquad (2.14)$$

where λ' and μ' are the Lamé constants for the isotropic layer.

Now that the required fields have been calculated, (2.9) may also be simplified. The matrix expansion of (2.10) with retention of up to the linear term is used once again, and substituted back in (2.9), and recalling that due to the free mechanical boundary condition at the top of the layer the zeroth order term for $\tau(0)$ is $\tau(0) = [\ 0\ 0\ 0\ \mathbf{v}]^t$ (superscript "t" indicating transpose)

$$\Gamma_u = \frac{jv_p}{4\omega}\{v.T_z' + j\omega\phi D_3'\} + \frac{h}{2v_p}\{v.\Gamma_T.v\} \qquad (2.15)$$

with Γ_T equal to Γ_{Tiso}, (2.14), or Γ_{Taniso}, Appendix II, depending on whether the layer is isotropic or anisotropic.

Using (2.13), (2.14), the weak coupling approximation [35] which approximates $D'_3 \approx \omega/v_p.(\varepsilon_{eff}+\varepsilon_o).\phi$ for a metallic overlay, and setting $\mathbf{v}=j\omega\mathbf{u}$, (2.15) becomes

$$\Gamma_u = -\frac{h\omega^2}{4v_p}[(\rho'v_p^2+\alpha_x')(u_x)^2+(\rho'v_p^2+\alpha_y')(u_y)^2+(\rho'v_p^2)(u_z)^2]-\frac{\omega}{4}(\varepsilon_{eff}+\varepsilon_0)(\phi)^2 \tag{2.16}$$

Equation (2.16) is the Perturbation expression for the upstep reflection coefficient in the situation of an isotropic metallic layer on the top of a piezoelectric substrate. It is worth noting that in this last equation the reflection coefficient is expressed in terms of free surface fields only. *Such a feature, as mentioned at the beginning of this section, permits an easy way of identifying and classifying planes where the directivity phenomenon is observed (including NSPUDT orientations), which is explored in the next two sections.* Due to the many simplifications involved which have been presented above, results using (2.16) are only approximate; they are checked against those using (2.9) in the last Section of this Chapter.

2.6 ARBITRARY ORIENTATIONS

In this section the impact of *arbitrary orientations* in the SAW reflection coefficient calculation is analyzed, based on the results and discussions of the previous sections, for both forward and backward incident waves (Fig. 2.3).

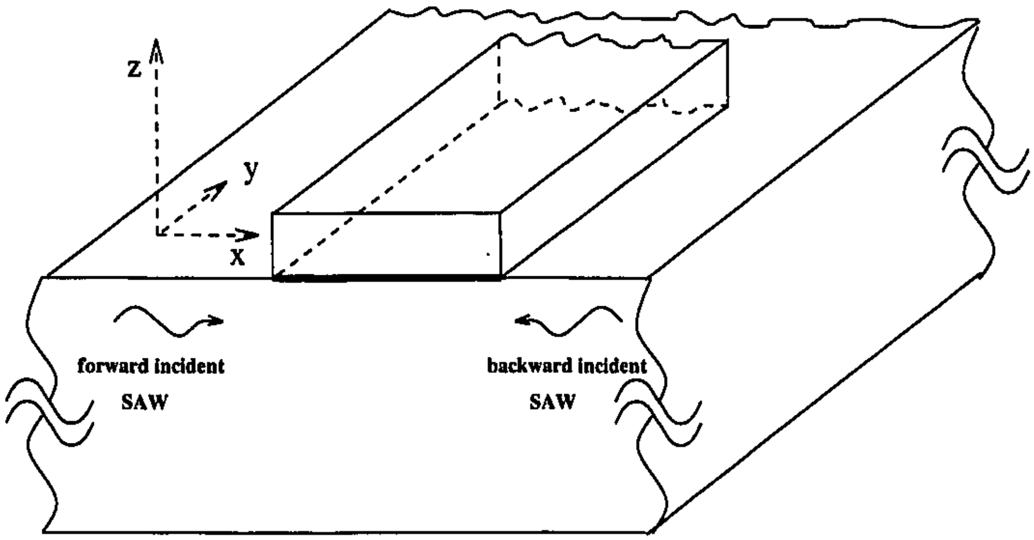

Fig. 2.3 Forward and backward incident SAW.

2.6.1 Forward orientations

For an arbitrary orientation, the forward travelling SAW solution, either in the free or in the layered regions, have fields (Appendix I)

$$v_{for} = \bar{v}_{for}(z)\ \exp[j(\omega t-\beta x)] \tag{2.17a}$$

$$T_{for} = \bar{T}_{for}(z)\ \exp[j(\omega t-\beta x)] \tag{2.17b}$$

$$\phi_{for} = \bar{\phi}_{for}(z)\ \exp[j(\omega t-\beta x)] \tag{2.17c}$$

$$D_{for} = \bar{D}_{for}(z)\ \exp[j(\omega t-\beta x)] \tag{2.17d}$$

with the field phasors $\bar{\mathbf{v}}_{for}$, $\bar{\mathbf{T}}_{for}$, $\bar{\phi}_{for}$, and $\bar{\mathbf{D}}_{for}$ having in principle arbitrary phase relations among themselves. Replacing these field phasors in the expressions for the reflection coefficient derived in the previous sections, (2.9) or (2.16), one can infer that the reflection coefficient in an arbitrary direction may have an associated phase angle, θ_r, which is not necessarily 0° or 180°. The existence of a complex reflection coefficient in arbitrary directions has important implications in SAW device operations and modelling as is discussed further in this chapter and in the remainder of this thesis.

As a first and general statement, a necessary and sufficient condition for θ_r to be different from 0° or 180° is that the SAW fields and material constants involved in evaluating (2.9) or (2.16) do not combine in a way which cancels the imaginary part of these expressions. Looking at the simplified perturbation theory reflection coefficient expression for a thin isotropic metallic film (2.16), one can see by inspection that for a complex reflection coefficient to exist, the relative phases of at least some of the fields must be different from 0°, 180° or 90°, with respect to the phase of one of the fields taken as reference. This fact leads to the conclusion that an **isotropic substrate** will <u>never</u> have a complex reflection coefficient, since the acoustic fields u_1 and u_3 are always in quadrature [8,9]. Therefore **anisotropy** is a necessary condition to obtain a complex reflection coefficient. But it is not a sufficient condition, since even for anisotropic materials there are directions for which the relative phases of the fields are equal to 0°, 180° or 90°.

Inspecting more carefully these directions in anisotropic materials where the phase of the fields with respect to each other are either 0°, 180° or 90°, one finds that these orientations occur *when the sagittal plane bulk-wave slowness curves have mirror symmetry with respect to the direction of propagation*. Due to this symmetry property, these directions shall be referred to, in this thesis, as *symmetric directions* or *symmetric orientations*, and the ones which do not satisfy this property will be consistently called as *asymmetric directions* or *asymmetric orientations*. For symmetric directions the complex eigenvalues[1] appear not only in negative conjugate pairs, but also in conjugate pairs; for asymmetric directions, the complex eigenvalues appear only in negative conjugate pairs. Therefore in order to have a complex reflection coefficient, one necessary condition for the material is to be anisotropic, and another is that the sagittal plane bulk-wave slowness curves <u>do not</u> have mirror symmetry with respect to the direction of propagation. If the surface is a mirror plane, by virtue of crystal symmetry, the sagittal plane bulk-wave slowness curves have mirror symmetry with respect to any direction of propagation in the plane, and therefore such planes do not have asymmetric orientations. Isotropic materials fit this 'symmetric orientation' classification, since any direction of propagation in an isotropic material presents a mirror plane characteristic.

It is certainly helpful to search for some means of physically visualizing what is happening along symmetric and asymmetric orientations. Assuming a pure Rayleigh mode in a non-piezoelectric material (u_2=0), and taking the phase of u_1 as a reference, the time dependent field equations for u_1 and u_3 can be written as

$$u_{1for} = |\bar{u}_{1for}(z=0)| \cos(\omega t-\beta x) \tag{2.18a}$$

$$u_{3for} = |\bar{u}_{3for}(z=0)| \cos(\omega t-\beta x+\phi) \tag{2.18b}$$

where Φ is the phase relation between the phasors u_3 and u_1. For symmetric orientations, which includes isotropic materials, Φ=90°, the fields u_1 and u_3 are in quadrature, and

[1] The eigenvalues referred to here are the values of Λ discussed in Appendix I, equation (I.11).

therefore a particle displacement movement is of the form of an ellipse with axes parallel to the x and z directions, as shown in Fig. 2.4a. For an asymmetric orientation Φ may assume any value different from 0°, 180° or 90°. The effect of having $\Phi \neq 90°$ is therefore to shift the main axes of the ellipse away from the directions x and z (Fig. 2.4b). In the case of a generalised SAW, a particle displacement in the u_2 direction is also present, and the elliptic motion is contained in an arbitrary plane in space.

2.6.2 Backward orientations

The fact that the reflection coefficient calculated from (2.9) or (2.16) may be complex, raises the question of what happens with the phase of the reflection coefficient for an incident SAW propagating in the backward or reverse direction as shown in Fig. 2.3. To discuss that, it is necessary to know what happens to the fields of such wave. The fields for a reverse propagating guided acoustic wave are related to the forward ones by [35, pp. 188]

$$\boldsymbol{v}_{back} = -\overline{\boldsymbol{v}}^{*}_{for}(z)\, \exp[j(\omega t+\beta x)] \tag{2.19a}$$

$$\boldsymbol{T}_{back} = \overline{\boldsymbol{T}}^{*}_{for}(z)\, \exp[j(\omega t+\beta x)] \tag{2.19b}$$

$$\phi_{back} = \overline{\phi}^{*}_{for}(z)\, \exp[j(\omega t+\beta x)] \tag{2.19c}$$

$$\boldsymbol{D}_{back} = \overline{\boldsymbol{D}}^{*}_{for}(z)\, \exp[j(\omega t+\beta x)] \tag{2.19d}$$

Replacing then the required backward wave fields phasors from above in the reflection coefficient expressions (2.9) or (2.16), leads to **the complex conjugate value of the forward reflection coefficient,** $\Gamma_{ubk}=\Gamma_u^*$, with associated phase angle $-\theta_r$. One can verify this result by inspection from substituting (2.19) in (2.16).

The fact that the upstep reflection coefficient for an incident reverse propagating SAW has the same magnitude as that of the forward wave but a phase angle with opposite sign, is of critical importance in the scalar modelling developed in the next section and used in other chapters of this thesis.

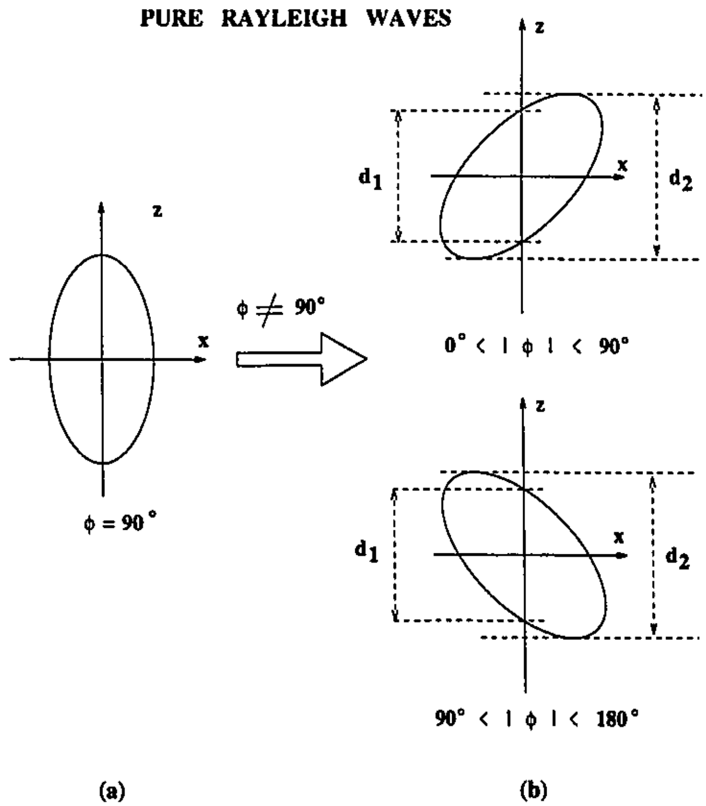

$$u_1 = |\bar{u}_1| \cos(\omega t - \beta x) \qquad u_3 = |\bar{u}_3| \cos(\omega t - \beta x + \phi)$$

$$\left(\frac{u_1}{|u_1|}\right)^2 + \left(\frac{u_3}{|u_3|}\right)^2 - 2\left(\frac{u_1}{|u_1|}\right)\left(\frac{u_3}{|u_3|}\right)\cos\phi = \sin^2\phi$$

$$\phi = \sin^{-1}\left(\frac{d_1}{d_2}\right)$$

Fig. 2.4 Particle displacement motion (included in the figure is the equation of an ellipse for a sagittally polarized wave): a) symmetric orientations; b) asymmetric orientations.

2.7 NETWORK MODEL REPRESENTATION AND ARBITRARY ORIENTATIONS

As mentioned in the introduction to this chapter, a major interest in calculating the reflection coefficient comes from the fact that it is a *scalar* quantity, and as such it allows the extraction of important SAW information in a condensed and simplified form. Actually, once the reflection coefficient is obtained, either by using the reciprocity relation method expression (2.9) or the simplified perturbation theory equation (2.16), an equivalent network model for the structures shown in Fig. 2.1 and Fig. 2.2 follows, as described in this section. An important issue addressed in the next paragraphs refers to the development of an original network element to account for SAW **arbitrary orientations**, which includes the asymmetric orientations defined in Section 2.6. This modelling is essential for the work presented in Chapters III and IV.

2.7.1 Symmetric orientations

For both structures in Fig. 2.1 and Fig. 2.2, the reflection coefficient for an incident SAW that reaches the film, is due to both distributed and localized effects. The distributed effects which contribute to the reflection coefficient are modelled as small changes in a real characteristic impedance in the perturbed transmission line region, Z_o to $Z_m=Z_o(1+\Delta_z)$, Fig. 2.5a. This change of the characteristic impedance in the metallized region with respect to the free region is attributed to the combined effects of piezoelectric shorting in the case of a conductive overlay, and of mechanical loading due to the dissimilar material properties of the overlay. The impedances Z_o and Z_m must be real since the SAW in both regions is assumed lossless. Also shown in Fig. 2.5a is the fact that the phase velocity in the perturbed region, v_m, is different from the velocity in the free region, v_o, i.e., $v_m=v_o(1+\Delta_v)$. The equivalent force and velocity mechanical network variables for this scalar model are defined as F_1 , v_1 , F_2 , v_2 , in the usual two-port network sense. The localized effects, which also contribute to the reflection coefficient, are related to the step discontinuities in the film and deserve some discussion.

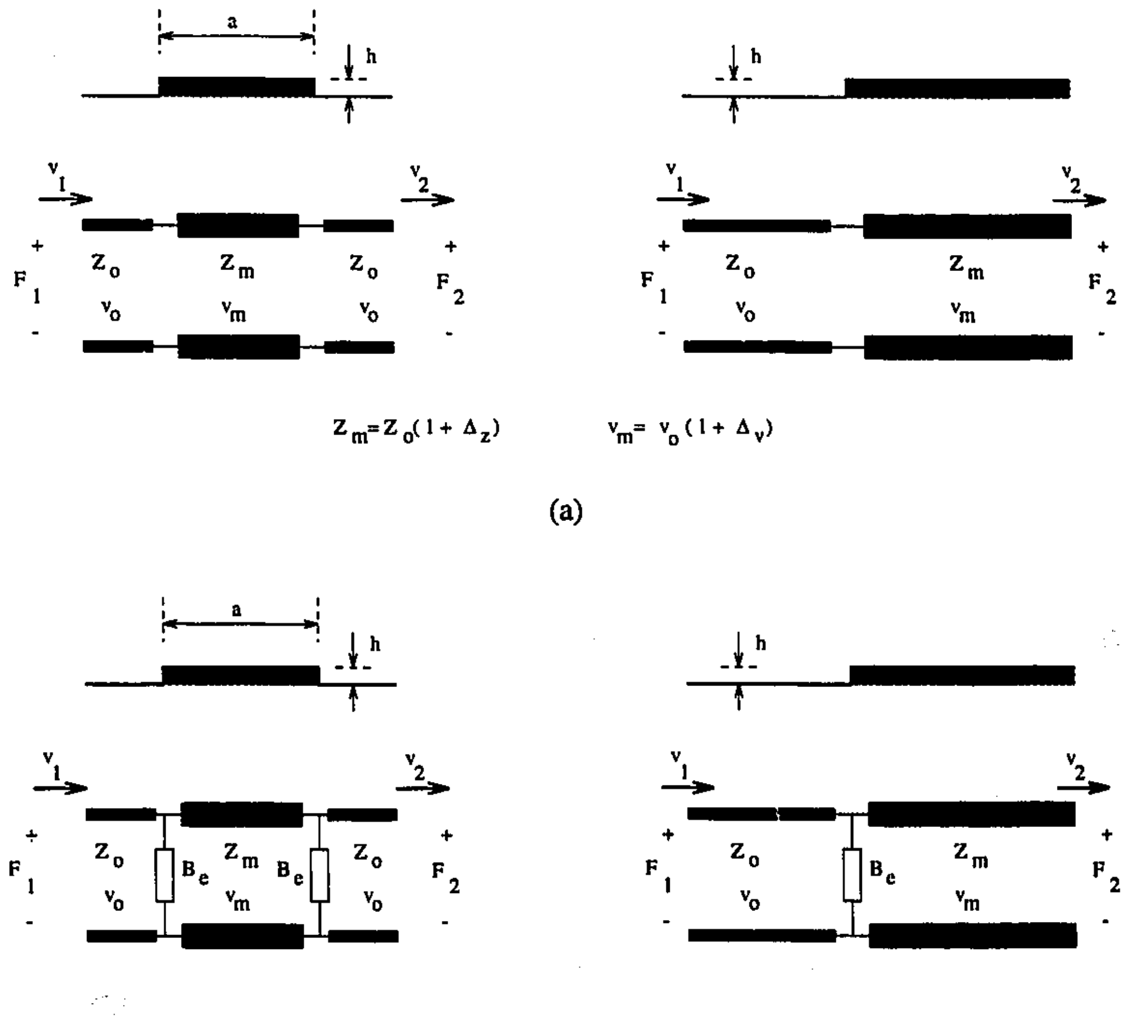

Fig. 2.5 Scalar network transmission line model: a) impedance discontinuities; b) inclusion of B_e.

From a historical perspective, researchers working along directions essentially symmetric, observed a slight downshift in the frequency response for the structures (grooved gratings) they were working with [39,40]. Such an experimentally observed phenomenon was referred to as a small **second order effect** and physically attributed to non-propagating or evanescent modes, which reactively store energy in the vicinity of the structures discontinuities. By analogy with electromagnetic problems, in particular microwave networks, a suggested scalar model parameter to describe the phenomenon consisted in the inclusion at the discontinuities of a shunt capacitive susceptance, B_e, which loads the line and slows down the wave (Fig. 2.5b) [40].

Values of B_e were empirically determined [40,41,42,43], usually accompanied by large experimental uncertainties. A theoretical analysis was proposed by Shimizu and Takeuchi [44] based on evanescent bulk modes but restricted to isotropic media, thus requiring some fitting in order to deal with piezoelectric substrates. Datta and Hunsinger [45] developed a theoretical procedure for analyzing an infinite periodic structure, consisting of repeated strips, in which they account for space harmonics of the periodic structure. In addition to the forward and backward surface waves (main harmonics), they include in the analysis other space harmonics, which couple to evanescent modes of the periodic structure, thus storing reactive power close to the surface. Although considering anisotropic substrates, piezoelectricity is excluded in [45], thus including only mechanical effects. The theoretical method derived in [45] has been reviewed, compared to variational results [46], and used by other researchers [47]. More recently a finite element method (FEM) procedure has been introduced [48,49] reporting theoretical results for the energy storage element. The method again assumes infinite periodic structures, and is used to calculate the dispersion curves of different kinds of arrays. Modelling circuit parameters are then determined by equating network predictions with FEM calculation for the dispersion curves. All the above mentioned theories give consistent results among themselves and experimental data, although the spread in these experimental and theoretical results for the values of B_e is relatively high (9% to 40% for the B_e calculation at h/λ=.01 on quartz ST-X, for example).

It should be noted that the reflection coefficient calculated in Section 2.4, and the perturbation theory approximation resulting from it (Section 2.5), consider only the forward and the backward modes in the analysis; evanescent modes are excluded, and thus those expressions do not yield the second order energy storage effect, B_e. Therefore along symmetric directions only the impedance mismatch represented in Fig. 2.5a is obtained from those expressions.

Based on reflection coefficient calculations or measurements, the concepts of a change in the transmission line real impedance and lumped susceptances is easily implemented, approximating the more complex SAW problem by a scalar network model. Such modelling has been used successfully in grating and resonator analysis and design along "symmetric" directions [50,51].

2.7.2 Asymmetric orientations

The model of Fig. 2.5 assumes that the reflection coefficient is the same for an incident SAW either in the forward or in the backward direction and restricts Fig. 2.5 to *symmetric* orientations. Along arbitrary directions the reflection coefficient may no longer be real (Section 2.6), and for an incident reverse propagating SAW, Γ_{ubk} is the complex conjugate of the reflection coefficient of the forward wave. Therefore, along arbitrary orientations, the structures of Fig. 2.1 and Fig. 2.2 may not be bilaterally symmetric.

Since no losses are being considered for the propagating SAWs in asymmetric orientations, Z_m and Z_o are still real. To account for Γ_u being complex in these directions, and to account for the fact that when approaching the disturbed region from an unperturbed region from the right, the reflection coefficient is the conjugate of that obtained when approaching the perturbed region from the left, a new reactive lumped element is added into the network model presented previously [52]. This new element is a shunt susceptance $j\,B_r$ and its conjugate $-j\,B_r$ at the two discontinuities, as shown in Fig. 2.6a. A shunt susceptance has been selected to model the asymmetry, although a series lumped reactance could also have been used. Subsequent to the publication of this new network element [52], and its inclusion in transducer models to account for directivity [53], other researchers [54] have used the opposite sign network elements to model the lack of bilateral symmetry in the structure.

From network theory, the real impedance mismatch $Z_m=Z_o(1+\Delta_z)$ and the susceptance B_r which account for asymmetric directions can then be given in terms of the reflection coefficient Γ_u by

$$\frac{Z_m}{Z_o} = \frac{|1+\Gamma_u|^2}{(1-|\Gamma_u|^2)} \tag{2.20}$$

$$b_r = B_r Z_o = 2\frac{Im\{\Gamma_u^*\}}{|1+\Gamma_u|^2} \tag{2.21}$$

with Γ_u given either by the reciprocity relation method (RRM) expression (2.9) or by the simplified perturbation theory equation (2.16). Note that b_r vanishes when the structure is aligned along symmetric orientations, where the reflection coefficient is real. Since for practical purposes, namely the thin metallic layers under consideration, Γ_u is much less than unity, the normalized susceptance, b_r , and Δ_z may be approximated by $b_r \cong Im\{2\Gamma^*_u\}$ and $\Delta_z \cong Re\{2\Gamma_u\}$, or $2\Gamma_u^* \cong \Delta_z + jb_r$. And since Δ_z and $b_r \ll 1$, the model satisfies $\Gamma_{ubk} = \Gamma_u^*$ very closely.

In Fig. 2.6b the second order energy storage effect discussed previously and modelled by the susceptance B_e , is included in parallel with the susceptance B_r for completeness. The change in the phase velocity in the perturbed region, $v_m=v_o(1+\Delta_v)$, is calculated numerically by solving the SAW problem in the free and metallized regions. Finding the proper phase velocity is actually the first step after which the fields can be evaluated, as it is illustrated in Section 2.9.

Finally it is worth noting in this section that orientations where the directivity phenomenon is observed, including therefore high directivity (NSPUDT) orientations, require the lack of bilateral symmetry. *Acknowledging such fact leads to the important and original conclusion that high directivity orientations do not exist in symmetric directions as defined in Section 2.6.*

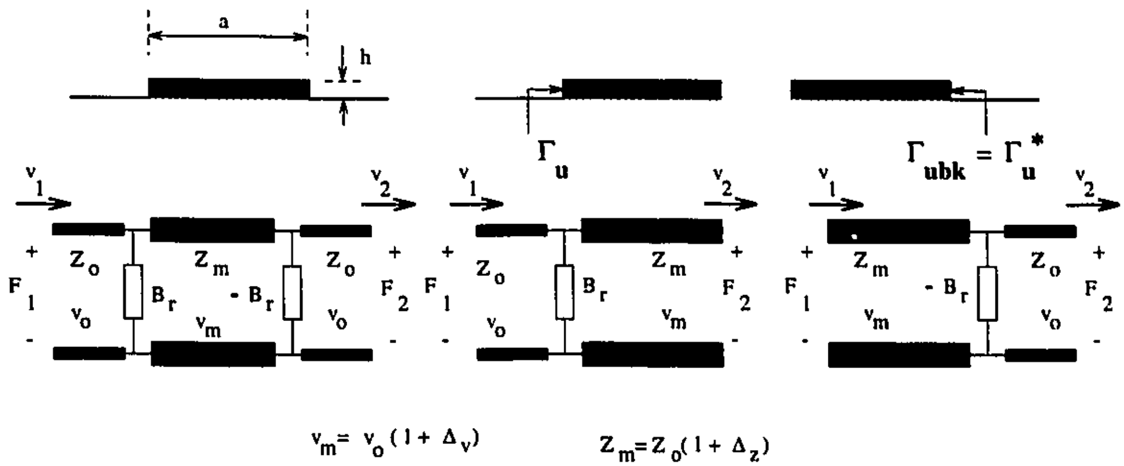

(a)

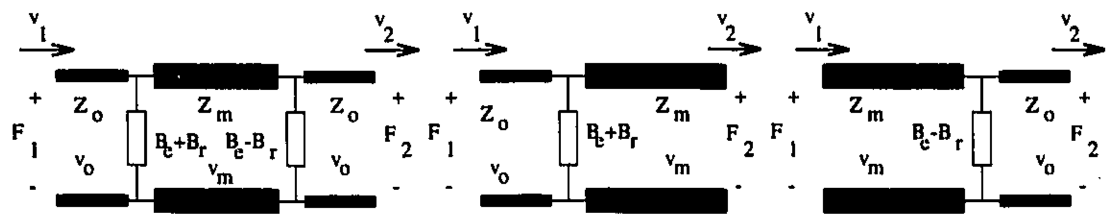

(b)

Fig. 2.6 Scalar network model: a) introduction a new network element B_r to account for bilateral asymmetry; b) B_e included.

2.8 MODE-MATCHING METHOD (MMM)

In an attempt to gain more insight into the scattering that occurs when a surface wave propagating in a free surface region encounters a semi-infinite thin metallic layered region, a mode-matching technique is used [36]. This method has been extensively applied in electromagnetic waveguide discontinuity problems for about half a century, and some of the fundamental papers describing this technique are in [55]. Basically, the waveguide fields at a discontinuity between two guides are written as a superposition of the available modes over the region which is common to both waveguides, and field continuity statements are made. An appropriate scalar product is then defined, and together with the field continuity statements, coefficients in the linear superposition terms of the waveguide modes, the unknowns, are numerically evaluated. This numerical evaluation consists of an optimization procedure, where the goal is to minimize an "error" function based both on the continuity equations and on the scalar products defined, and employing power statements as constraints. Once the scalar coefficients for the waveguide modes are obtained, the mode scattering coefficients are also determined. These steps are detailed in this section.

For the present SAW problem depicted in Fig. 2.2, the only modes taken into account in these numerical experiments are the lossless generalized Rayleigh wave modes. In this case a SAW incident from the left is scattered into a reflected SAW and a transmitted SAW in the layered region, all other modes being ignored. Such approximation is based on experimental evidences which show that other propagating modes usually have negligible effect in the passband where the main mode, in this case SAW, is excited. The continuity statements are made for the propagating component fields

$\tau_v=[v \;\; j\omega\phi]^t$ and $\tau_p=[T_x \;\; D_l]^t$ at the discontinuity plane. For the generalized Rayleigh modes considered, the continuity field statements are of the form

$$\tau_p^L = \sum_{j=f,b} c_j \tau_p^{Lj} = \tau_p^{Rf} \tag{2.22a}$$

$$\tau_v^L = \sum_{j=f,b} c_j \tau_v^{Lj} = \tau_v^{Rf} \tag{2.22b}$$

where L, R, f, b, stand for left, right, forward and backward, respectively. These are really approximations and not equalities, since we are not at this stage including any evanescent or pseudo-SAW modes in the superposition. The inclusion of pseudo-SAW modes in this mode-matching technique is deferred to for Chapter 5. The following **scalar product or inner product** is defined in order to implement the MMM, namely

$$<\tau_p^{Xw},\tau_v^{Zt}> = \int_{-\infty}^{0} -[(\tau_p^{Xw})_M.(\tau_v^{Zt})_M^* + (\tau_p^{Xw})_E^*.(\tau_v^{Zt})_E]dz \tag{2.23}$$

Suffixes M and E stand for mechanical and electrical field components, respectively. X, Z are either R (right) or L (left), and w, t are either f (forward) or b (backward) labels. In (2.23) the mechanical and electrical parts of τ_v and τ_p are considered separately so that when X=Z and w=t, the power carried by the SAW in a forward or in a reverse mode is calculated. Inner products are formed between: (2.22a) and τ_v^{Rf}; (2.22b) and τ_p^{Lf}; (2.22b) and τ_p^{Rf}; (2.22a) and τ_v^{Lf} ; leading to four "equations", in which there is no z dependency, containing the two unknown scalar coefficients c_f, c_b. Finding values for these coefficients, using an appropriate minimization procedure on the functions (24) below, constitutes the essentials of the mode-matching method.

$$f_a = <\tau_p^{L},\tau_v^{Rf}> - <\tau_p^{Rf},\tau_v^{Rf}> \tag{2.24a}$$

$$f_b = <\tau_p^{Lf},\tau_v^{L}> - <\tau_p^{Lf},\tau_v^{Rf}> \tag{2.24b}$$

$$f_c = <\tau_p^{Rf},\tau_v^{L}> - <\tau_p^{Rf},\tau_v^{Rf}> \tag{2.24c}$$

$$f_d = <\tau_p^{L},\tau_v^{Lf}> - <\tau_p^{Rf},\tau_v^{Lf}> \tag{2.24d}$$

Different constraints on the scattering parameters were tested in the process of minimization of (2.24), namely: (i) lossless power conservation stating that the incident SAW power equals the reflected plus the transmitted SAW power ($|S_{11}|^2+|S_{21}|^2=1$); (ii) power inequality stating that the reflected plus the transmitted SAW power is less than the incident SAW power ($|S_{11}|^2+|S_{21}|^2\leq1$), thus admitting some loss; and (iii) a lossless reciprocal ($S_{12}=S_{21}$) transition ($|S_{11}|^2+|S_{21}|^2=1$ and $|S_{22}|^2+|S_{12}|^2=1$). The results obtained were essentially independent of the selected constraint. The only difference was in the computing time to achieve the results. Numerical results of this method are discussed in the next Section 2.9, which concern with the numerical results of the theory discussed in this chapter.

2.9 NUMERICAL RESULTS

In this section numerical results are presented, which are based on the theoretical development discussed in this chapter. In order to calculate the reflection coefficient, Γ_u, one has to evaluate several fields at z=0 in the free and the layered regions, as examined in the previous sections. High-level programs, which run in a Matlab commercial software environment, were developed for calculating the required SAW properties and fields

(Matlab is a registered trademark of The Mathworks, Inc., Natick, MA 01760-1500).

A first illustration material chosen is quartz, Euler angles (0° 132.75° 25°); in this orientation a generalised SAW having all field components exists, and it corresponds to the cut used in NSPUDT investigations and devices [56]. This is a material in which reflections due to mechanical loading play a major role, and therefore can not be neglected in the analysis.

Figs. 2.7, 2.8, and 2.9 show some of the representative fields involved in the derivation of the reflection coefficient expression (2.9) for normalized thicknesses (h/λ) up to 3%. Fig. 2.7 shows the amplitudes of the three components of $\mathbf{T'}_z(z=0)$ calculated using (2.5) and calculated using Perturbation Theory (dotted curves). At 1% thicknesses the agreement in the absolute value for the normal components T'_{xz} and T'_{zz} is about 3.5%, whereas for layers as thick as 3% the agreement for T'_{zz} is 12% between the Perturbation Theory and equation (2.5). Note that above 1.5%, T'_{zz} starts to show a non-linear behaviour and begins to differ significantly from the Perturbation Theory. The three components of the $\mathbf{T'}_x(z=0)$ are represented in Fig. 2.8. From this curve one can see that even for small thicknesses the values of T'_{xx} and T'_{xz} vary significantly. In the perturbation theory, the components of $\mathbf{T'}_x(z=0)$ are calculated irrespective of thicknesses and in the present example assume the values $|T'_{xx}|=1.32$ GPa, $|T'_{xy}|=0.15$ GPa, and $T'_{xz}\cong 0$ GPa. In the case of $|T'_{xx}|$ note from Fig. 2.8 that the discrepancy goes from about 4% for $h/\lambda=1\%$ to about 15% for $h/\lambda=3\%$. Furthermore, for thicker layers the values $|T'_{xz}|$ are no longer negligible, assuming a magnitude larger than that of $|T'_{xy}|$ at $h/\lambda=3\%$. The velocity fields in the layer are plotted in Fig. 2.9 also with respect to the normalized thicknesses. Referring to the perturbation theory once again one should recall that the approximation $\mathbf{v}=\mathbf{v'}$ is done, as mentioned in Section 2.5, in which case the velocity fields in the layer have their amplitudes approximated by $|v_x|=0.054$ Km/s, $|v_y|=0.018$ Km/s, and $|v_z|=0.088$ Km/s, in the present example. Comparing these values to the ones plotted in Fig. 2.9, an agreement of 2% is obtained for $|v_z|$ up to $h/\lambda=3\%$, whereas for $|v_x|$ the agreement drops from about 6% to 23% in going from thicknesses of 1% to 3%.

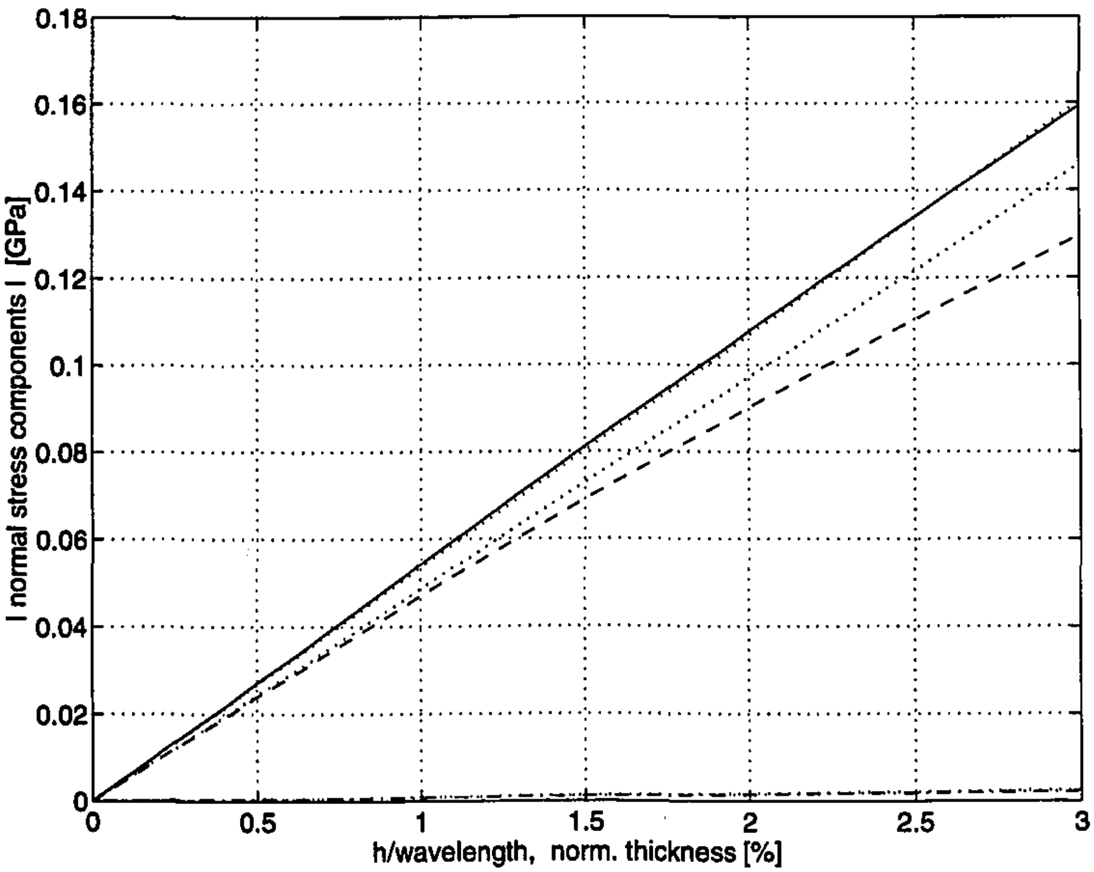

Fig. 2.7 Magnitude of the normal stress components versus normalised thickness: T'_{xz} (solid curve), T'_{yz} (dashdot curve), T'_{zz} (dashed curve), Perturbation Theory (dotted curves).

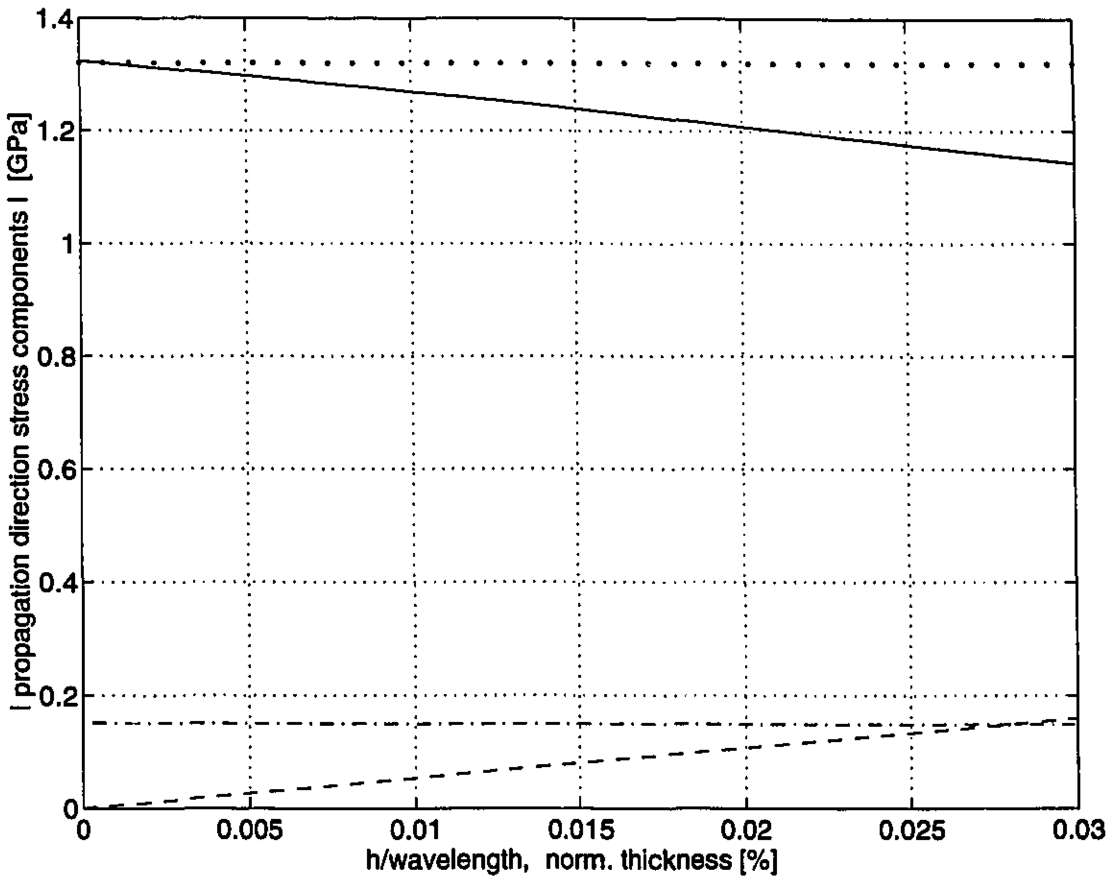

Fig. 2.8 Magnitude of the propagation direction stress components versus normalised thickness: T'_{xx} (solid curve), T'_{xy} (dashdot curve), T'_{xz} (dashed curve), Perturbation Theory T'_{xx} (dotted curve).

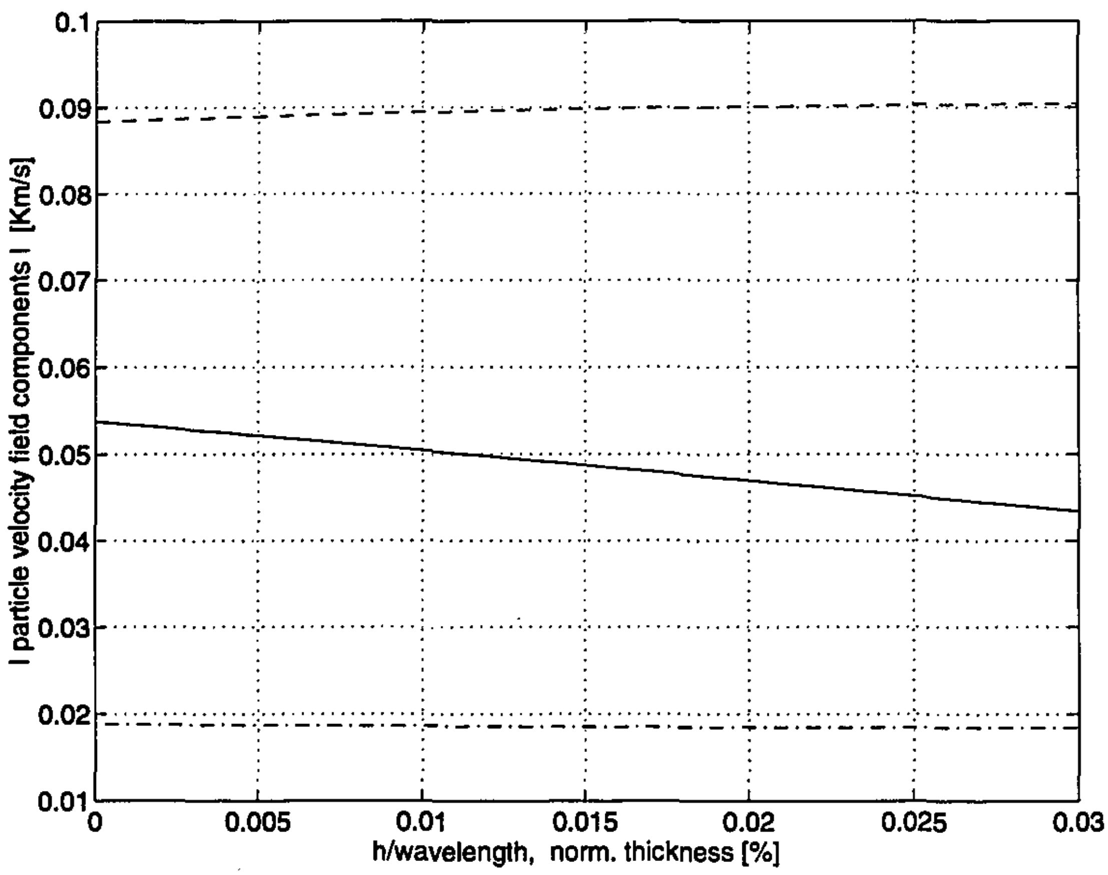

Fig. 2.9 Magnitude of the particle velocity field components: v_x (solid curve), v_y (dashdot curve), v_z (dashed curve).

Although a fairly good agreement is obtained between the fields calculated using Perturbation Theory and the non-perturbation procedure outlined in Section 2.4, the main concern is the reflection coefficient Γ_u. In Fig. 2.10 the reflection coefficient calculated using (2.9) is compared with Perturbation Theory approximation (2.16). From this figure an error in $|\Gamma_u|$ of about 15% at (h/λ) of 1%, deteriorates to an error of almost 30% at 1.5%, and to a factor of almost 2 at 3%, demonstrating the importance of using the proper field variations with thickness in computing Γ_u. Thus, for this material and cut, the Perturbation Theory is inadequate for $(h/\lambda)>1\%$. As can be inferred from Fig. 2.10, $|\Gamma_u|$ is mainly determined by the mechanical loading for (h/λ) of about 0.5% and higher for this material and cut. The discrepancy in the phase between the two calculations is not very high.

In Fig. 2.11 the reflection coefficient is examined in more detail by breaking (2.9) up into a δ-function contribution at the edges and a non-δ-function contribution. The solid curves are for the total magnitude and phase of Γ_u as were shown in Fig. 2.10, and are included here for comparison; the dashed curves shows the non-δ-function contribution to Γ_u in (2.9); the circles show the δ-function contribution alone to Γ_u in (2.9); and the dashdot curves show the calculations obtained using the mode-matching method. The following information can be inferred from the data presented in Fig. 2.11:

i.) The magnitude of the δ-function contribution at the edges is slightly larger than the non-δ-function contribution, whereas the respective phases are about +90° and -90°, for $(h/\lambda)>.5\%$. It follows then that since these contributions are almost 180° out of phase, the total reflection coefficient will be approximately equal to their difference with a phase close to that of the larger one. Indeed in Fig. 2.11 it is clear that the resultant phase is that of the δ-function contributions (circles), and that the resultant amplitude is essentially the **difference** in the two contributions with significant inaccuracy implications. Since the property which makes this quartz cut a Natural Single Phase Unidirectional Transducer - NSPUDT - orientation is that $\angle\, \Gamma_u \approx 90°$ [56], Fig. 2.11 highlights the importance of the δ-function contribution in calculating Γ_u.

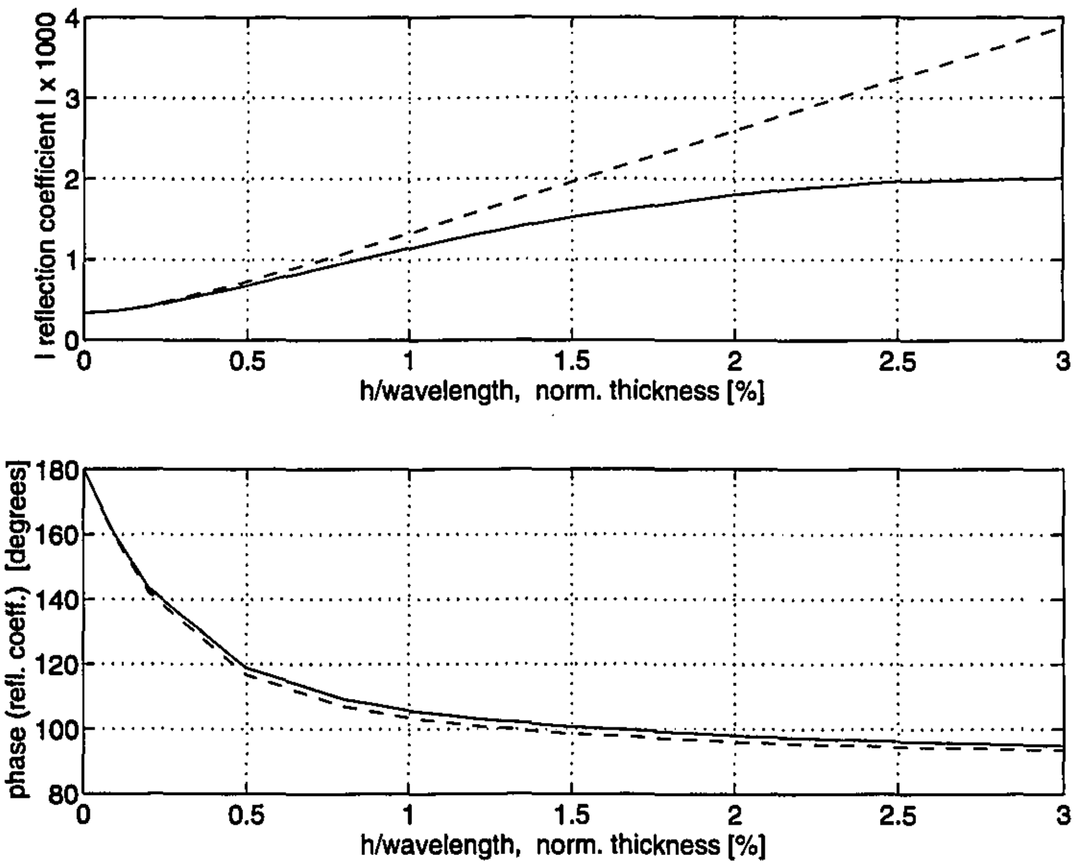

Fig. 2.10 Reflection coefficient, Γ_u, magnitude and phase: non-perturbation theory (RRM, (2.9), solid curves); perturbation theory ((2.16), dashed curves).

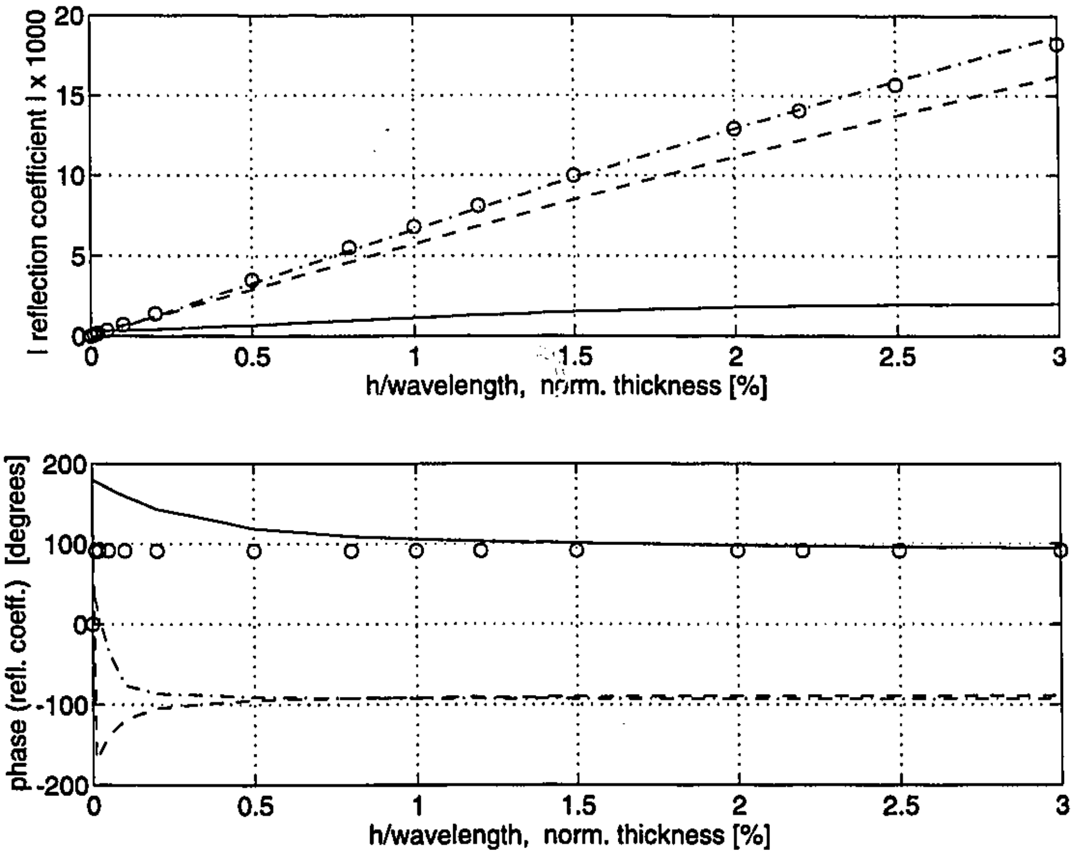

Fig. 2.11 Reflection coefficient magnitude and phase: non-perturbation theory (RRM, (2.9), solid curves); without the δ-function contribution (dashed curves); δ-function contribution alone (circles); and mode-matching method (dashdot curves).

ii.) The mode-matching method, described in Section 2.8, yields data shown as the dashdot curves, and gives values of Γ_u which are very close to those calculated without the δ-function contribution. The optimization routine used in the mode-matching method is doing its best to minimize the field discontinuity with the available free and layered modes, and in doing so it reaches a value which is almost the value given by (2.9) when the δ-function contributions are excluded.

iii.) The δ-function type of contribution is not accounted for in the attempt at using the MMM technique as described in Section 2.8.

For the reverse propagating direction, i.e. Euler angles (0° 132.75° -155°), a point worth mentioning is that the reflection coefficient values obtained by each of the 3 methods discussed are the complex conjugates of those obtained for the Euler angles (0° 132.75° 25°). This conjugacy result shows that these methods seem able to describe directivity effects, but with only SAW modes fail to account for energy storage. A reflection coefficient magnitude plot, including the effect of energy storage determined from measured data [56], is shown in Fig. 2.12 together with the magnitude result presented in Fig. 2.10, for (h/λ) of up to 2%. It is interesting to notice the effect of the energy storage in the magnitude of the reflection coefficient of an upstep discontinuity is to decrease it in one direction and reinforce it in the reverse direction.

In Section 2.6 the impact of arbitrary orientation in the SAW reflection coefficient has been discussed in terms of the forward and backward fields and in terms of the orientation of propagation. It is mentioned in that section that for orientations contained in mirror planes, or *symmetric directions*, the relative phases of the fields are either 0°, 90° or 180°, and that the resulting reflection coefficients are real numbers. On the other hand, for orientations not contained in mirror planes, or *asymmetric directions*, the relative phases of the fields are arbitrary, and the resulting reflection coefficient is a complex number. A useful way of identifying mirror planes is to observe that, as a result of the mirror symmetry, the bulk-wave slowness curves of the sagittal plane are symmetric with respect to the mirror plane. Consequently in a mirror plane the eingenvalues or partial waves (Appendix I) which decay with depth and which are used to built the SAW solution

(4 in the most general case) appear in conjugate pairs or are real numbers. For asymmetric orientations such symmetries do not exist. Table 2.1 illustrates the above mentioned properties of the SAW solutions for some symmetric and some asymmetric orientations; for clarity of presentation the fields are normalised in magnitude with respect to $| u_t |$, but the phase of ϕ is adopted as the reference. The reflection coefficient is also calculated for an aluminum (Al) layer with normalized thickness $h/\lambda=1\%$, using the RRM expression (2.9) and the simplified perturbation theory expression (2.16). As already mention in this chapter in Section 2.6, the fact that arbitrary orientations may result in a complex reflection coefficient, is of paramount importance in the device modelling developed in the next chapters.

In this section numerical evaluations were performed to verify and discuss the theoretical development of the previous sections of this chapter. Fields quantities relevant in the calculation of the reflection coefficient, and the reflection coefficient itself were calculated with respect to an aluminum layer thickness and the results have been compared to the perturbation theory approximation. Such comparison allowed the evaluation of the errors in the accuracy of the perturbation method in this case, which, for the quartz cut example used, is about 15% at $(h/\lambda)=1\%$. The results obtained for the mode-matching method developed considering only the generalized Rayleigh wave modes, showed good agreement with the Reciprocity Relation Method excluding the δ-function contribution for the quartz orientation considered. Additional results were presented for other materials and orientations and the issue of symmetric and asymmetric directions were exemplified at these orientations.

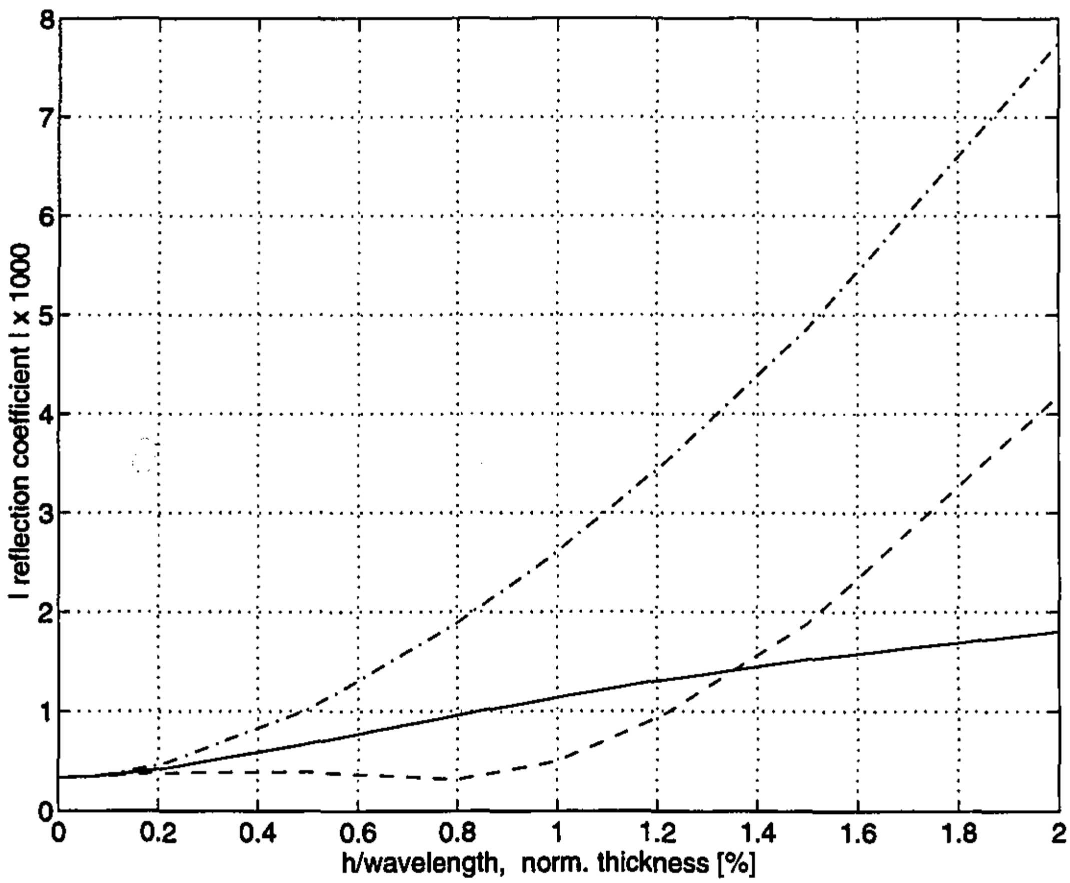

Fig. 2.12 Reflection coefficient magnitude (2.9) (solid curve); and including the effect of energy storage, (2.9) for quartz, (Euler angles: [0° 132.75° 25°]) (dashed curve), and (2.9) for quartz in the reverse direction, (Euler angles: [0° 132.75° -155°]) (dashdot curve).

TABLE 2.1

Free surface SAW solutions and the reflection coefficient, Γ_u

Material and orientation (Euler angles, [degrees]) classification (Section 2.6) & (free surface v_p [Km/s])	Decaying eigenvalues (free surface solution)	Free surface fields @ z=0 u1,u2,u3,ϕ (magnitude [Km], [TV] and phase [degrees])	Reflection coefficient Γ_u @ h/λ=1% (RRM) (magnitude and phase [degrees])	Reflection coefficient Γ_u @ h/λ=1% (Pert.Theory) (magnitude and phase [degrees])
quartz ST-25° [0° 132.75° 25°] asymmetric (3.2475)	0.04+j0.007 0.19-j0.003 0.30-j0.010 0.47-j0.07	1.00 -45.3 0.34 -166 1.64 -133 3.10 0	1.15e-3 106	1.33e-3 103
quartz ST-X [0° 132.75° 0°] symmetric (3.1576)	0.044 0.323 0.341 0.400	1.00 0 0.14 90 1.52 -90 2.47 0	2.65e-3 180	3.00e-3 180
YZ $LiNbO_3$ [0° 90° 90°] asymmetric (3.4897)	0.04+j0.016 0.22-j0.095 0.29+j0.090 (Rayleigh)	1.00 -175 0 1.43 95 7.32 0	1.22e-2 178	1.23e-2 -179
128 YX $LiNbO_3$ [0° 38° 0°] symmetric (3.9805)	0.039 0.110-j0.092 0.110+j0.092 0.486	1.00 90 0.06 180 1.12 0 5.29 0	1.13e-2 180	9.36e-3 180

TABLE 2.1 (cont.)

$LiTaO_3$	0.09-j0.025	1.00 124	2.33e-3 123	2.47e-3 120
[0° 90° 141.25]	0.10-j0.069	0.32 116		
asymmetric	0.24+j0.087	1.43 26		
(3.2095)	0.38+j0.044	2.46 0		
36 YX $LiTaO_3$	0.085	1.00 -90	1.29e-3 0	1.45e-3 0
[0° -54° 0°]	0.25+j0.073	8.76 180		
symmetric	0.25-j0.073	1.49 180		
(3.1252)	0.404	7.30 0		
$Li_2B_4O_7$	0.08+j0.162	1.00 0	1.53e-2 180	1.75e-2 180
[135° 90° 90°]	0.08-j0.162	0		
symmetric	0.286	0.87 -90		
(3.4652)	(Rayleigh)	2.77 0		
$Li_2B_4O_7$	0.04+j0.029	1.00 58.2	6.03e-3 -122	6.07e-3 -122
[0° 60° 90°]	0.30-j0.002	0		
asymmetric	0.34-j0.25	1.42 -3.8		
(3.2638)	(Rayleigh)	5.61 0		
GaAs	0.019	1.00 -90	1.14e-3 0	1.19e-3 0
[0° 0° 30°]	0.20+j0.18	4.09 -90		
symmetric	0.20-j0.18	2.28 180		
(2.6697)	0.380	3.96 0		
GaAs	0.04+j0.059	1.00 -155	4.98e-4 -154	4.35e-4 -144
[0° 20° 30°]	0.13-j0.162	1.37 -83		
asymmetric	0.31+j0.175	1.61 123		
(2.6635)	0.38-j0.003	1.64 0		

2.10 SUMMARY AND CONCLUDING REMARKS

In this chapter a Reciprocity Relation Method, which is not a perturbation method, is developed to calculate an original SAW reflection coefficient expression due to a thin metallic strip on a piezoelectric substrate (Sections 2.3 and 2.4). From the expression derived, a perturbation theory expression is also obtained (Section 2.5). In this derivation, the Tiersten Boundary Condition has been generalized to any anisotropic non-piezoelectric layer. Comparison of results (Section 2.9) predicted by the RRM and the perturbation theory allowed to calculate errors in the accuracy of perturbation method with respect to thickness, which, for the quartz ST-25° example used, are about 15% at $(h/\lambda)=1\%$.

It is verified that anisotropy is a requirement to have asymmetry in the reflection coefficient with respect to the forward and backward propagating SAWs (Section 2.6). Directions of propagation are classified into symmetric and asymmetric based on the reflectivity study developed, the second including high directivity or NSPUDT orientations.

A scalar model is developed, which considers asymmetric orientations. This model includes a new network element, B_r, which accounts for the fact that the reflection coefficient calculated at an upstep in the backwards direction is the complex conjugate of the reflection coefficient of an upstep in the forward direction (lack of bilateral symmetry). Along symmetric directions B_r naturally vanishes, since the calculated reflection coefficient is a real number.

Some numerical experiments are carried out using a mode-matching technique, in an attempt to gain more insight into the scattering that takes place when a SAW propagating in the free region encounters a semi-infinite thin metallic layer (Section 2.8). This method, employed over half a century in electromagnetic waveguide discontinuity problems, is applied for the first time in SAW problems, to the best of the author's knowledge.

In the next chapter, the scalar network model developed, based on the reflectivity study performed, is used to described periodic structures oriented along arbitrary directions.

CHAPTER III

THE SHORT-CIRCUITED GRATING

3.1 INTRODUCTION

In this chapter the short-circuited grating oriented along arbitrary directions (therefore including asymmetric orientations) is studied.

The short-circuited grating is the natural choice to start studying of the impact of arbitrary orientations on SAW structures since it avoids dealing with any electrical circuit variable, simplifying the examination of SAW structures. The results obtained in this chapter form the basis for the more complete and complicated analysis of a transducer on an arbitrary orientation developed in the Chapter IV.

The basis for the analysis is the scalar model developed in the previous chapter. The approach here is to define a cell and cascade many of them using their transmission matrices to obtain an overall grating transmission description which includes the effects of asymmetry.

From the predictions of the network model for SAW gratings, the recent widely-used coupling-of-modes (COM) description is also evaluated. It is demonstrated that the incremental COM description can be derived from the unit-cell-based network model for the grating, showing the consistency between the COM description and the scalar model developed in this thesis.

An analytically tractable approximation for the short-circuited grating cell in arbitrary orientations is also described, from which rather simple explicit formulas are derived for two of the COM coefficients that predict their dependence on material parameters and on frequency. Numerical calculations for the full and the approximate descriptions of the short-circuited grating, indicate that the approximate formulas may yield results which are valid over almost 30% relative bandwidths.

In Section 3.2 the short-circuited grating structure and the respective network model are introduced for arbitrary orientations. A review of the coupling-of-modes (COM) approach and the solution to the COM equations are presented in Sections 3.4 and 3.5. Two of the COM coefficients are obtained from the network model (Sections 3.6, 3.3), and using an approximate network model (GWF approximation,[50]), extended to include asymmetric orientations, analytical expressions are derived for the COM coefficients (Section 3.7). In Section 3.8, numerical comparisons between the Network Model, the COM Model, and the Approximated Model, together with a frequency response illustration of the COM parameters, and a discussion regarding the effect of arbitrary orientation on short-circuited grating, are presented. Section 3.9 is devoted to some concluding remarks to this chapter.

3.2 THE STRUCTURE AND THE RESPECTIVE NETWORK MODEL

The short-circuited SAW grating structure and the periodic network model discussed in this chapter are shown in Fig. 3.1. The grating consists of a large but finite number of periodic surface disturbances [52,57] caused, in this case, by the metallization deposited on the substrate. Each period of the grating is modelled by the circuit of Fig. 3.1b which, as discussed in the previous chapter, incorporates distributed disturbances via the quantities Z_m , v_m , and the localized effects via B_e and B_r .

For a SAW propagating in the x direction one can see that even if a piezoelectric substrate is considered, all the metallic fingers are at the same potential. The analysis of the short-circuited grating is simplified by the fact that only the equivalent scalar mechanical variables need be determined. Nevertheless the analysis of the short-circuited grating structure is an essential step in the understanding of more elaborate SAW structures oriented along arbitrary directions, such as the IDT and the open-circuited grating discussed in the next chapter.

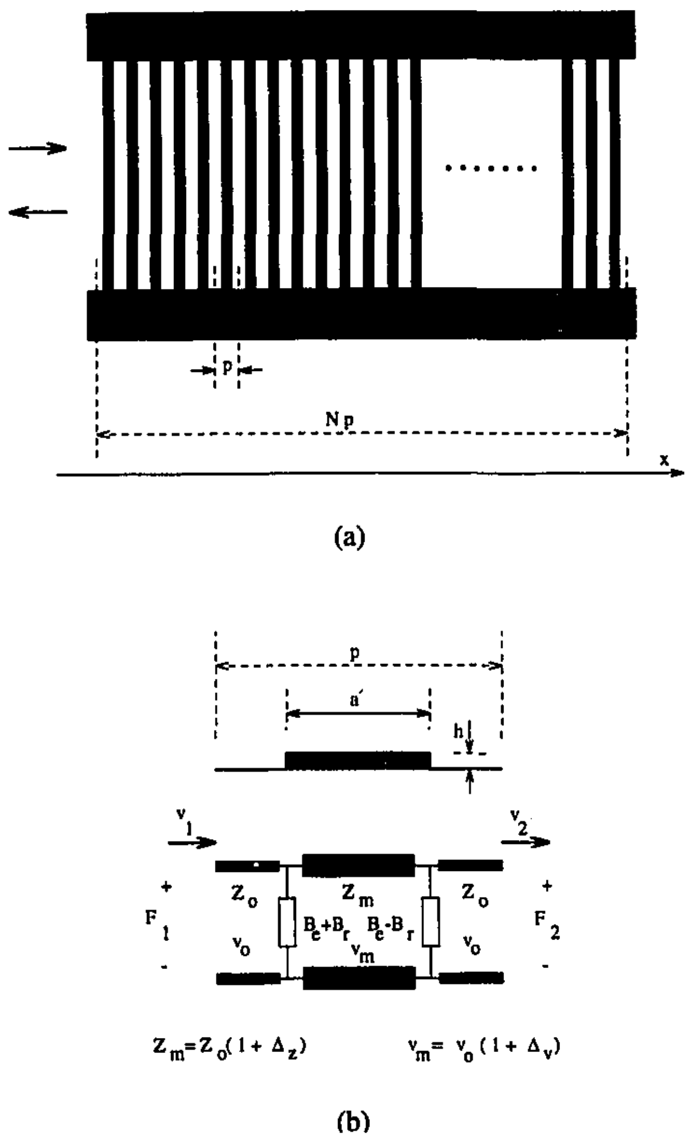

Fig. 3.1 a) Short - circuited SAW grating structure; b) Scalar model for the arbitrarily oriented short - circuited grating cell.

The Network Model for the short-circuited structure cell, depicted in Fig. 3.1b, is essentially the same network presented in Fig. 2.6b, Section 2.7, including the shunt susceptance B_r to account for asymmetric orientations. The basic difference with respect to the discussion in Chapter II is the fact that the structure in Fig. 3.1a has a periodicity p, and therefore Fig. 3.1b is referring to a cell and not to an isolated strip as in Chapter II. The period p defines a unit cell element for the grating structure, with mechanical variables F_1 , v_1 , F_2 and v_2 associated with ports 1 and 2 respectively. The model for Fig. 3.1a consists of a cascade of subnetworks each having a simple transmission matrix (ABCD) representation (three transmission line segments and two lumped susceptance elements, the latter (B_r and B_e) added in pairs at each discontinuity) [52,57].

The ABCD matrix of the unit cell illustrated in Fig. 3.1b is written

$$\begin{bmatrix} F_1 \\ v_1 \end{bmatrix} = \begin{bmatrix} A & B \\ C & D \end{bmatrix} \begin{bmatrix} F_2 \\ v_2 \end{bmatrix} \tag{3.1}$$

where the acoustic terminal variables F_i and v_i are equivalent to voltages and currents in the network sense. The unit-cell matrix elements A, B, C, and D are obtained by multiplying the cascaded ABCD matrices of the unit cell's subnetworks. Since the network is reciprocal and lossless (dissipation is neglected in the present formulation) the ABCD matrix elements satisfy reciprocity (AD-BC=1) and losslessness (A and D real, B and C imaginary), but are not constrained to be bilaterally symmetric ($A \neq D$). The inverse relationship relating the variables at port 2 to those at port 1 is

$$\begin{bmatrix} F_2 \\ v_2 \end{bmatrix} = \begin{bmatrix} D & -B \\ -C & A \end{bmatrix} \begin{bmatrix} F_1 \\ v_1 \end{bmatrix} = \boldsymbol{Q} \begin{bmatrix} F_1 \\ v_1 \end{bmatrix} \tag{3.2}$$

where **Q**, defined as the period transfer matrix, also has unit determinant because of reciprocity. Either (3.1) or (3.2) is a *discrete or port description for a unit cell* of the grating structure.

For an N-element grating the overall transfer matrix $\mathbf{Q}_N=\mathbf{Q}^N$ is calculated either by exponentiation or, to reduce computing time, by using the explicit formula based on the Cayley-Hamilton theorem for 2 x 2 matrices having unit determinant

$$\mathbf{Q}_N = \mathbf{Q}^N = \mathbf{Q}\,\frac{\sin N\Theta}{\sin\Theta} - \mathbf{I}\,\frac{\sin(N-1)\Theta}{\sin\Theta} \tag{3.3}$$

where **I** is the identity matrix and Θ is given by

$$2\cos\Theta = trace(\mathbf{Q}) \tag{3.4}$$

The reflection (S_{11} and S_{22}) and transmission (S_{12} and S_{21}) characteristics of an N-element grating are completely specified by $\mathbf{Q}_N$ through

$$\begin{bmatrix} F(Np) \\ v(Np) \end{bmatrix} = \mathbf{Q}_N \begin{bmatrix} F(0) \\ v(0) \end{bmatrix} \tag{3.5}$$

and in the most general case by impedances terminating the two end-ports of the full structure in the common two-port network sense.

The matrix elements in (3.1) or (3.2) for a unit cell, expressed in terms of normalised susceptances $b_e=Z_oB_e$ and $b_r=Z_oB_r$, obtained by taking $Z_o=1$, are:

$$\begin{aligned} A = {} & [\cos\theta_m - b_e(1+\Delta_z)\sin\theta_m]\cos 2\theta_s + \\ & + b_r(1+\Delta_z)\sin\theta_m - b_e\sin 2\theta_s\cos\theta_m + \\ & - \frac{1}{2}\{(1+\Delta_z)^{-1} + (1+\Delta_z)[1-(b_e^2-b_r^2)]\}\sin 2\theta_s\sin\theta_m \end{aligned} \tag{3.6}$$

$$\begin{aligned} B = {} & j[\cos\theta_m - b_e(1+\Delta_z)\sin\theta_m]\sin 2\theta_s + \\ & + j(1+\Delta_z)\cos^2\theta_s\sin\theta_m - j2b_e\sin^2\theta_s\cos\theta_m + \\ & - j[(1+\Delta_z)^{-1} - (1+\Delta_z)(b_e^2-b_r^2)]\sin^2\theta_s\sin\theta_m \end{aligned} \tag{3.7}$$

$$\begin{aligned} C = {} & j[\cos\theta_m - b_e(1+\Delta_z)\sin\theta_m]\sin 2\theta_s + \\ & - j(1+\Delta_z)\sin^2\theta_s\sin\theta_m + j2b_e\cos^2\theta_s\cos\theta_m + \\ & + j[(1+\Delta_z)^{-1} - (1+\Delta_z)(b_e^2 - b_r^2)]\cos^2\theta_s\sin\theta_m \end{aligned} \tag{3.8}$$

$$\begin{aligned} D = {} & [\cos\theta_m - b_e(1+\Delta_z)\sin\theta_m]\cos 2\theta_s + \\ & - b_r(1+\Delta_z)\sin\theta_m - b_e\sin 2\theta_s\cos\theta_m + \\ & - \frac{1}{2}\{(1+\Delta_z)^{-1} + (1+\Delta_z)[1-(b_e^2 - b_r^2)]\}\sin 2\theta_s\sin\theta_m \end{aligned} \tag{3.9}$$

where

$$\theta_s = \frac{\pi}{2}\frac{f}{f_o}(1-\eta) \tag{3.10}$$

$$\theta_m = \pi\frac{f}{f_o}\frac{\eta}{(1+\Delta_v)} \tag{3.11}$$

with $f_o = v_o/2p$ the Bragg frequency, and $\eta = a/p$ the metallization ration.

The network model of Fig. 3.1b, (3.5) and the A, B, C, and D using (3.6) to (3.11) are taken as a reference in evaluating other models or approximations for the short-circuited grating structure.

3.3 DIFFERENTIAL DESCRIPTION

By simple algebraic procedures, a differential equation with solution that satisfies (3.5) exactly at points which are integer multiples of period p can be obtained. In a fundamental sense this "differential-from-discrete" procedure is at the heart of the so-called coupling-of-modes analysis that is reviewed in Section 3.4. From periodic linear systems theory it is known that there exists a constant or *spatially invariant* matrix **H** such that

$$\frac{d}{dx}\begin{bmatrix} F(x) \\ v(x) \end{bmatrix} = \boldsymbol{H}\begin{bmatrix} F(x) \\ v(x) \end{bmatrix} \tag{3.12}$$

with solutions given in terms of the transition matrix, e^{Hx}, as

$$\begin{bmatrix} F(x) \\ v(x) \end{bmatrix} = e^{\boldsymbol{H}x}\begin{bmatrix} F(0) \\ v(0) \end{bmatrix} \tag{3.13}$$

The continuous solution (3.13) will have a physical meaning at "port" positions that are integer multiples of p (x=Np) at which ports it equals the solution (3.5); hence for one period the transition matrix must equal the period transfer matrix, i.e.,

$$e^{\boldsymbol{H}p} = \boldsymbol{Q} \tag{3.14}$$

and, because of (3.14), **H** and **Q** have the same eigenvectors. Also from linear algebra:

i.) **Q** has the triple product factorization

$$\boldsymbol{Q} = \boldsymbol{T}\begin{bmatrix} \lambda_1 & 0 \\ 0 & \lambda_2 \end{bmatrix}\boldsymbol{T}^{-1} \tag{3.15}$$

where λ_1, λ_2 are the eigenvalues of **Q**, and **T** is the eigenvector matrix of **Q**.

ii.) e^{Hp} has the triple-product factorization

$$e^{\boldsymbol{H}p} = \boldsymbol{T}\begin{bmatrix} e^{\mu_1 p} & 0 \\ 0 & e^{\mu_2 p} \end{bmatrix}\boldsymbol{T}^{-1} \tag{3.16}$$

where μ_1, μ_2 are the eigenvalues of **H**, and **T** is the same eigenvector matrix as in (3.15). From i.) and ii.) it follows that the eigenvalues, μ_i, of **H** are expressed in terms of the eigenvalues, λ_i, of **Q** by

$$\mu_i = \frac{(\log \lambda_i)}{p} \tag{3.17}$$

Since **H** and **Q** have the common eigenvector matrix **T**, the same factorization form of (3.15) applies to **H**

$$\boldsymbol{H} = \boldsymbol{T} \begin{bmatrix} \mu_1 & 0 \\ 0 & \mu_2 \end{bmatrix} \boldsymbol{T}^{-1} \tag{3.18}$$

hence from **Q**, one obtains **T** and the λ_i , which then allows **H** to be constructed using (3.17) and (3.18). Therefore the coefficient matrix **H** for the differential equation (3.12) is obtained directly from **Q** the transfer matrix of a unit cell, sometimes also referred to as the discrete transition matrix; **Q** is calculated directly from (3.2) using the elements defined in (3.6) to (3.9).

Note that since only two independent port-variables are necessary to characterize a two-port network, any independent pair of port-variables other than F and v can be expressed as a linear combination of F and v. It follows then that a transfer matrix corresponding to the relationship (3.2) for any other two port-variables is obtained algebraically from **Q**. *The COM description is thus contained in (3.18).*

In next Section, the procedure for determining the COM coefficient matrix from the **Q** matrix, as well as the relationship between the two variables used in the COM formulation with respect to the voltage and current variables of Fig. 3.1b, are discussed.

3.4 REVIEW OF THE COM APPROACH

In 1976 several papers appeared [58,59] using a coupling-of-modes (COM) method for modelling a discrete periodic system by a pair of coupled differential equations, through which one could study perturbations and excitations in a material. The COM approach for the short-circuited structure postulates that there exists a set of differential equations relating two variables, namely a forward wave amplitude and a backward wave amplitude, containing two independent parameters. The two parameters are usually determined in the narrowband sense, and are essentially phenomenological, although attempts have been made to relate them to physically known quantities [59,60,31,61]. In this section, the solution to the COM equations is reviewed and an explicit procedure is given for determining the COM equations from the network model. It is not the aim of this section to rederive the COM equations and their fundamental relations. These are documented in the references [59,60,62,31]. Nevertheless, the following points should be mentioned:

i.) With some exceptions [60,61] most authors [63,64,62,31] use a set of variables that lead to differential equations with nonconstant coefficients. In fact a more convenient way of postulating the problem is through a set of two differential equations with *constant coefficients*, in variables designated in this work as $\bar{R}$ and $\bar{S}$, and with voltage V_G, the strip voltage, as the input forcing function. $\bar{R}(x)$ and $\bar{S}(x)$ are forward and backward wave amplitudes respectively and correspond to the variables A_1 and A_2 of [60] and the variables R and S of [61] respectively. Working with constant coefficients permits making use of much of the available theoretical and computational tools for dealing with the systems of equations with constant coefficients.

ii.) The COM equations are sometimes presented as a system of three equations, which may be misleading [60,62]. The solution for the current in the connecting bus (cited as a third variable) follows explicitly from the solutions to $\bar{R}$, $\bar{S}$ and the strip voltage "distribution" $V_G(x)$.

The COM equation is

$$\frac{d}{dx}\begin{bmatrix}\bar{R}(x)\\ \bar{S}(x)\end{bmatrix} = \begin{bmatrix} -j(k_{11}+\delta) & -jk_{12} \\ jk_{12}^{*} & j(k_{11}+\delta)\end{bmatrix}\begin{bmatrix}\bar{R}(x)\\ \bar{S}(x)\end{bmatrix} + \begin{bmatrix} j\alpha \\ -j\alpha^{*}\end{bmatrix} V_G(x) \tag{3.19}$$

where $\delta = \pi(f-f_o)/pf_o$ is the detuning parameter, and x is the SAW propagating direction. The 2×2 coefficient matrix in (3.19) is given the matrix symbol **K**. Variables with an overbar are used here to ensure that the notation in (3.19) is not confused with other symbols that have been used in [60,62,31,61]. The k_{11} and k_{12} (coupling coefficients), and α (transduction coefficient) in (3.19) are the three COM parameters as defined in [31], even though in that paper the variables are different from those in (3.19) and the coefficient matrix is not spatially invariant.

Before reviewing the solutions to (3.19) and deriving the parameters k_{11} and k_{12}, in the next sections, two issues are addressed. The **first** concerns the choice of variables. Since the scalar model for the grating is given by a two-port network, any two independent variables are sufficient to describe its behaviour. The $\bar{R}$ and $\bar{S}$ and the F and v variables at integer multiples, n, of a period, *p*, for Z_o=1 are related by [61]

$$F(np) = e^{-jn\pi}\,[\bar{R}(np) + \bar{S}(np)] \tag{3.20}$$

$$v(np) = e^{-jn\pi}\,[\bar{R}(np) - \bar{S}(np)] \tag{3.21}$$

and conversely

$$\bar{R}(np) = \frac{e^{jn\pi}}{2}\,[F(np) + v(np)] \tag{3.22}$$

$$\bar{S}(np) = \frac{e^{jn\pi}}{2}\,[F(np) - v(np)] \tag{3.23}$$

with n=0 as the origin or x=0 location. The **second** issue relates to the fact that COM is a differential equation description and the COM coefficients are not related in a simple way to physical parameters and have a dependence on frequency and mark-to-space ratio that is not easily seen, although some approximations have been proposed and used [60,31]. The network model defined in this thesis is a discrete transfer matrix description, and since solutions can be achieved using either the COM or the network model formulations, it is shown in Section 3.6, how to obtain the COM coefficients from the network model. From such procedure, the validity of the proposed approximations in [60,31] is examined.

3.5 SOLUTION TO THE COM EQUATION

Equation (3.19) describes a system of the form $\dot{\mathbf{X}}=\mathbf{AX}+\mathbf{Bu}$, standard in linear systems and control theory. The well-known solution for the variables $\bar{R}$ and $\bar{S}$ is given by

$$\begin{bmatrix} \bar{R}(x) \\ \bar{S}(x) \end{bmatrix} = \Phi(x-x_0)\begin{bmatrix} \bar{R}(x-x_0) \\ \bar{S}(x-x_0) \end{bmatrix} + \int_{x_0}^{x} \Phi(x-r)\begin{bmatrix} j\alpha \\ -j\alpha^{*} \end{bmatrix} V_G(r)\, dr \tag{3.24}$$

where $\Phi(x-x_0)$ is the transition matrix, which can be derived for the case of the zero-input (unforced, $V_G=0$) system. For a second-order system the "zero-input" or homogeneous solution is given in terms of $\Phi(x)=e^{\mathbf{K}x}$, where $\mathbf{K}$, the coefficient matrix in (3.19), has the explicit form obtained directly using the triple-matrix product procedure described in

$$\Phi = e^{Kx} = \begin{bmatrix} \cosh(\lambda_1 x) - j\dfrac{(k_{11}+\delta)}{\lambda_1}\sinh(\lambda_1 x) & -j\dfrac{k_{12}}{\lambda_1}\sinh(\lambda_1 x) \\ j\dfrac{k_{12}^*}{\lambda_1}\sinh(\lambda_1 x) & \cosh(\lambda_1 x) + j\dfrac{(k_{11}+\delta)}{\lambda_1}\sinh(\lambda_1 x) \end{bmatrix} \tag{3.25}$$

with $\lambda_1=[|k_{12}|^2-(k_{11}+\delta)^2]^{1/2}$, the system eigenvalues being λ_1 and $-\lambda_1$. Although only shorted gratings are studied in this chapter, the full solution to (3.24) is given for completeness, and will be referred to in the next chapter, where a transducer structure is discussed. Equation (3.24), in particular, permits a solution for cases where the voltage V_G is different at each strip as a convolution of Φ and V_G. The "zero-state" convolution integral or the particular solution is, for V_G constant

$$\begin{bmatrix} \overline{R}(x) \\ \overline{S}(x) \end{bmatrix}_{zs} = V_G \int_0^x \Phi(x-r) \begin{bmatrix} j\alpha \\ -j\alpha^* \end{bmatrix} dr = V_G \begin{bmatrix} \sigma_1 \\ \sigma_1^* \end{bmatrix} \tag{3.26}$$

with

$$\sigma_1 = \frac{\{\alpha^* k_{12} - \alpha(k_{11}+\delta)\}}{\lambda_1^2}[1-\cosh(\lambda_1 x)] + j\frac{\alpha}{\lambda_1}\sinh(\lambda_1 x)] \tag{3.27}$$

The solution (3.26) given above applies when $V_G \neq 0$, therefore both for the case of an IDT, where excitation is present, or for the case of an open-circuited grating. An explicit solution for the transducer bus current follows directly from (3.26), and requires the calculation of the COM parameter α, discussed in the next chapter.

In order to compare the predictions of the COM model as given by (3.25) with those of the network model, values for k_{11} and k_{12} must first be obtained. In the next section the procedure for calculating the values of k_{11} and k_{12} from the network model is described.

3.6 DETERMINATION OF k_{11} and k_{12}

The COM coefficients in (3.24) and (3.25) are k_{11} , k_{12} and α. The transduction coefficient α needs be determined when $V_G \neq 0$ in (3.24), and reference to it is deferred to the next chapter. This section demonstrates how k_{11} and k_{12}, the elements of **K** under shorted strip conditions ($V_G=0$), are obtained from the network model given in this thesis using straightforward algebraic computations.

The problem here is to find the COM matrix elements from the network model ABCD matrix in (3.1) or its inverse **Q** in (3.2) of the unit cell in Fig. 3.1b. From **Q** obtained from (3.1) to (3.11) using the method given in Section (3.2), the COM unit-cell transition matrix Φ is calculated by use of relationships (3.20) to (3.23) between the $\bar{R}$, $\bar{S}$ and F, v variables over one period, namely through

$$\begin{bmatrix} \bar{R}(p) \\ \bar{S}(p) \end{bmatrix} = -\frac{1}{2}\begin{bmatrix} 1 & 1 \\ 1 & -1 \end{bmatrix} Q \begin{bmatrix} 1 & 1 \\ 1 & -1 \end{bmatrix}\begin{bmatrix} \bar{R}(0) \\ \bar{S}(0) \end{bmatrix} = \Phi \begin{bmatrix} \bar{R}(0) \\ \bar{S}(0) \end{bmatrix} \tag{3.28}$$

The COM coefficient matrix **K** of (3.19) is now calculated from Φ in (3.28) using the discrete-to-incremental procedure described in Section 3.3. Using this approach, the COM parameters' behaviour with respect to frequency, mark-to-space ratio, or any other variation in the network model parameters are determined.

In summary, the sequence of calculations is:

i) find **Q** from the network model equations (3.1) to (3.11), then Φ and its eigenvalues (λ_i) and its eigenvector matrix **T** from (3.28);

ii) obtain the eigenvalues μ_i of **K** using (3.17);

iii) finally calculate **K** by using the triple-product form (3.18), hence k_{11} and k_{12}.

All the computations are carried out on a PC or Sun-station, through high level programs, which run in a Matlab commercial software environment. The values obtained for k_{11} and k_{12} at the resonant frequency (frequency of maximum reflectivity for the short-circuited grating structure) previously found from the network model, $f=f_R$, are then used in (3.25).

3.7 EXTENSION OF THE FARNELL (GWF) APPROXIMATION

The expressions (3.6) to (3.10) for the matrix elements of the unit cell describe the behaviour of the network model in Fig. 3.1b exactly. As shown by Farnell [50], for the situation corresponding to Fig. 2.5a, where $B_r=0$, equations (3.6) to (3.10) can be approximated by a simpler form near the Bragg frequency $f_o=v_o/2p$, and which provides greater insight into the grating characteristics. The GWF approximation [50] consists in carrying out a Taylor expansion with respect to frequency of the network model described in Section 3.2 and retention of lowest order powers of Δ_v, Δ_z, and b_e. Extending the same procedure to include the new element b_r, the approximate ABCD matrix of a unit cell of period *p* becomes

$$\begin{bmatrix} -1-\frac{1}{2}(\gamma^2+b_r^2\sin^2(\pi\eta)-b_rF) & -j(\delta p+b-d)) \\ -j(\delta p+b+d) & -1-\frac{1}{2}(\gamma^2+b_r^2\sin^2(\pi\eta)+b_rF) \end{bmatrix} \tag{3.29}$$

where

$$\delta = \frac{\pi(f-f_o)}{pf_o} \tag{3.30}$$

$$b = b_e - \left(\frac{\pi f}{f_o}\right)\eta\,\Delta_v \tag{3.31}$$

$$d = \Delta_z\sin(\pi\eta) - b_e\cos(\pi\eta) \tag{3.32}$$

$$\gamma^2 = d^2 - (\delta p + b)^2 \tag{3.33}$$

$$F = 2[\sin(\pi\eta) + d + b\cos(\pi\eta)] \tag{3.34}$$

with Δ_z and Δ_v as defined in Fig. 3.1b. Since this approximation relies on a Taylor expansion, it is only accurate over a limited bandwidth. For narrow-band resonators this is more than adequate: it is even sufficient to take the elements Δ_z, b_e, b_r, and Δ_v evaluated at $f=f_o$ in (3.29), with δ, the detuning parameter, as the only frequency dependent parameter. This is the main feature of the method developed in [50] for the symmetric case $b_r=0$.

A narrow-band approximation to the COM transition matrix $\mathbf{\Phi}$ is obtained from (3.29) using the transformations (3.20) to (3.23). Hence, using steps i) to iii) given in Section 3.6, an approximation to **K** near the Bragg frequency is given by

$$K(f \approx f_o, \eta) \approx \frac{1}{p}\begin{bmatrix} -j(b+\delta p) & -jd + b_r \sin\eta\pi \\ jd + b_r \sin\eta\pi & j(b+\delta p) \end{bmatrix} \tag{3.35}$$

Comparing (3.35) with (3.19) the following formulas follow for k_{11} and k_{12} at $f \approx f_o$

$$k_{11} p(f \approx f_o) = b = b_e - \left(\frac{\pi f}{f_o}\right) \eta \, \Delta_v \tag{3.36}$$

$$\begin{aligned} k_{12} p(f \approx f_o) &= d + j b_r \sin(\pi\eta) = \\ &= (\Delta_z + j b_r)\sin(\pi\eta) - b_e \cos(\pi\eta) \end{aligned} \tag{3.37}$$

For a 50% mark-to-space ratio, $\eta = 1/2$, approximate expressions for the cell ABCD elements which are valid over a wider bandwidth than in (3.29) are obtained by retaining a frequency dependent second order term which is neglected in (3.29). These expressions are used to obtain an approximation to $\mathbf{\Phi}$ using the transformations in (3.20) to (3.23) and hence again using the steps i) to iii) given in Section 3.6 an approximation to **K** is given by

$$K(f,\eta=\frac{1}{2}) \cong \frac{1}{p}\begin{bmatrix} -j(b+\delta p) & b_r-j\left(\Delta_z+\dfrac{b_e\delta p}{2}\right) \\ -b_r+j\left(\Delta_z+\dfrac{b_e\delta p}{2}\right) & j(b+\delta p) \end{bmatrix} \tag{3.38}$$

Comparing (3.38) with (3.19) the following explicit formulas are obtained for k_{11} and k_{12} at $\eta=1/2$

$$k_{11}p(\eta=\frac{1}{2}) = b = b_e - \left(\frac{\pi f}{2f_o}\right)\Delta_v \tag{3.39}$$

$$k_{12}p(\eta=\frac{1}{2}) = (\Delta_z+jb_r) + \frac{b_e\delta p}{2} \tag{3.40}$$

Explicit formulas given in [31], with $\eta=1/2$, and using the preceding notation, are

$$k_{11}p = b_e\left\{\frac{f}{f_o}\right\} - \left(\frac{\pi f}{2f_o}\right)\Delta_v \tag{3.41}$$

$$k_{12}p = 2\Gamma_u^*\left\{\frac{f}{f_o}\right\} \cong (\Delta_z+jb_r)\left\{\frac{f}{f_o}\right\} \tag{3.42}$$

A comparison of (3.36) and (3.39) with (3.41), and (3.37) and (3.40) with (3.42), leads to the conclusion that the terms bracketed by { } in (3.41) and (3.42) should not be there and furthermore that (3.42) is missing an energy storage term contribution. Even with these deletions as corrections, (3.41) and (3.42), seem only valid for η=0.5.

3.8 COMPARISON OF DIFFERENT METHODS

In this section the following numerical results concerning the approximate models and the network model are given:

i. Comparing frequency responses for the network model, the COM constant coefficients model, and the GWF model;

ii. Comparing the profiles close to the resonant frequency for the network model, the COM constant coefficients model, and the GWF model;

iii. Finding the frequency dependence of the equivalent frequency dependent COM coefficient matrix **K**(f) from the network period **Q** matrix;

iv. Evaluating approximate explicit formulas for the COM elements **K**(f).

3.8.1 Comparison of different methods

From previous considerations in this chapter, both the COM and the GWF approximations have limitations with regard to bandwidth. The COM coefficients are frequently calculated (or measured) at a specific frequency, normally either f_o or f_R , and taken as constants from this point on in calculating the frequency response of a grating or transducer structure. In this way, the COM approximation that uses frequency independent parameters is evaluated. In the GWF approximation for a grating, a Taylor expansion is carried out near f_o and only the lowest usable powers of the parameter Δ_z, b_e and Δ_v are retained in (3.29). A question that naturally arises is: over what bandwidths can these models be used with acceptable accuracy?

The following simulations use a 680 strips, and a shorted grating with metallization ratio η=0.5 and h/λ=1%, in the NSPUDT orientation on quartz (Euler angles: [0° 132.75° 25°]) [62,31] and b_e as estimated in [53,56]. The frequency independent COM coefficients calculated, as explained in Section 3.6, at the resonant frequency, f_R , previously found from the network model are then used in (3.25) for the COM calculations. Some of the next comparisons are done in terms of the scattering parameters (S-parameters). The conversion between ABCD and scattering matrices is done in the regular network sense, and the conversion between the COM unit-cell based transfer matrix and the ABCD matrix is given in (3.28).

As a first attempt to compare approximate models, Figs. 3.2 and 3.3 show plots of magnitude and phase for the reflection coefficient S_{11}, and the transmission coefficient S_{21}, respectively, versus the normalized frequency $f_n=f/f_o$ for the network model (Section 3.2), the COM model (Section 3.5), and the GWF model discussed in Section 3.7. For the 2% bandwidth shown in Figs. 3.2 and 3.3, one finds excellent agreement between the approximated model of Section 3.7, the COM solution, and the network model calculations. It is hard to distinguish any differences in these figures.

Close to the resonant frequency, at f_n=.998, the forward and backward wave amplitudes, $\tilde{R}(x)$ and $\tilde{S}(x)$, are plotted with respect to the strip position for the network model, the COM model, and GWF model (Fig. 3.4). In Fig. 3.5 the net forward power at f_n=.998 is verified for the short-circuit grating structure. Figs. 3.4 and 3.5 verify once again the consistency and the good agreement between the approximated GWF model of Section 3.7, the COM solution, and the network model calculations.

Over broader bandwidths, larger differences appear. In Figs. 3.6 and 3.7 the absolute value of the percentage difference for S_{21} between the COM model, the network model predictions, and the "GWF" approximate model results are shown over a 30% bandwidth, Fig. 3.6, and a 6% bandwidth, Fig. 3.7, respectively. From these plots, it is seen that for frequencies a few percent away from f_o, the Bragg frequency, the error rapidly increases for both the GWF and the COM (constant k_{11} and k_{12}) approximations and for a frequency ±3% from f_o, Fig. 3.7, the percentage difference for this particular NSPUDT orientation is around 25%. Note that the predictions with respect to variation with frequency are very close for both COM and GWF approximations over a 6% bandwidth, beyond which, they deviate significantly from each other as seen in Fig. 3.6. The conclusion is that these two approximate models can not be used over bandwidths larger than a few percent.

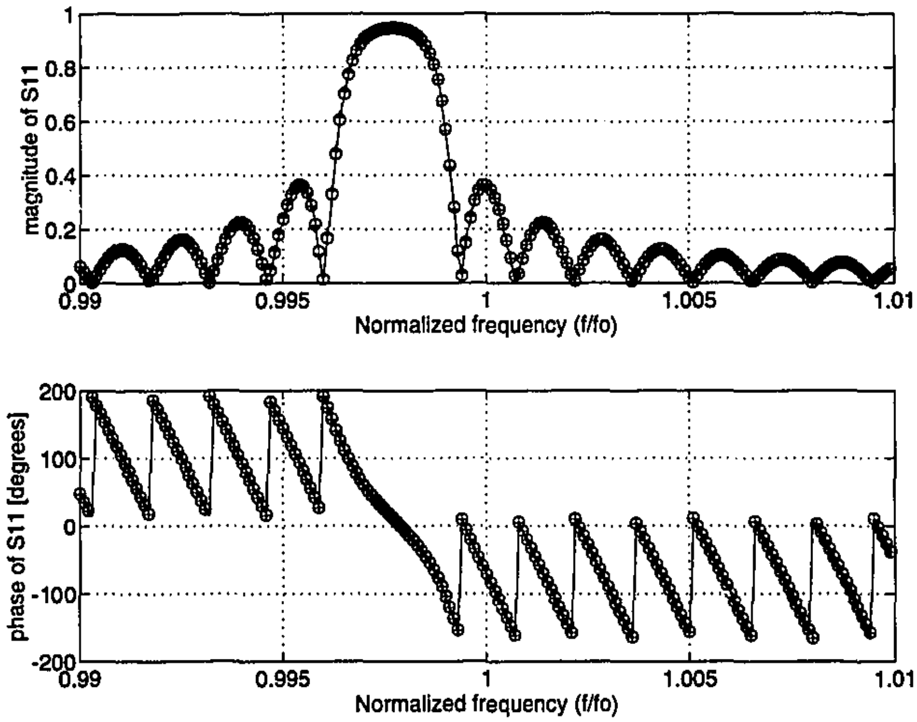

Fig. 3.2 Calculated a) magnitude and b) phase of S_{11}; network model (solid curve), COM (ooo), and GWF model (+++).

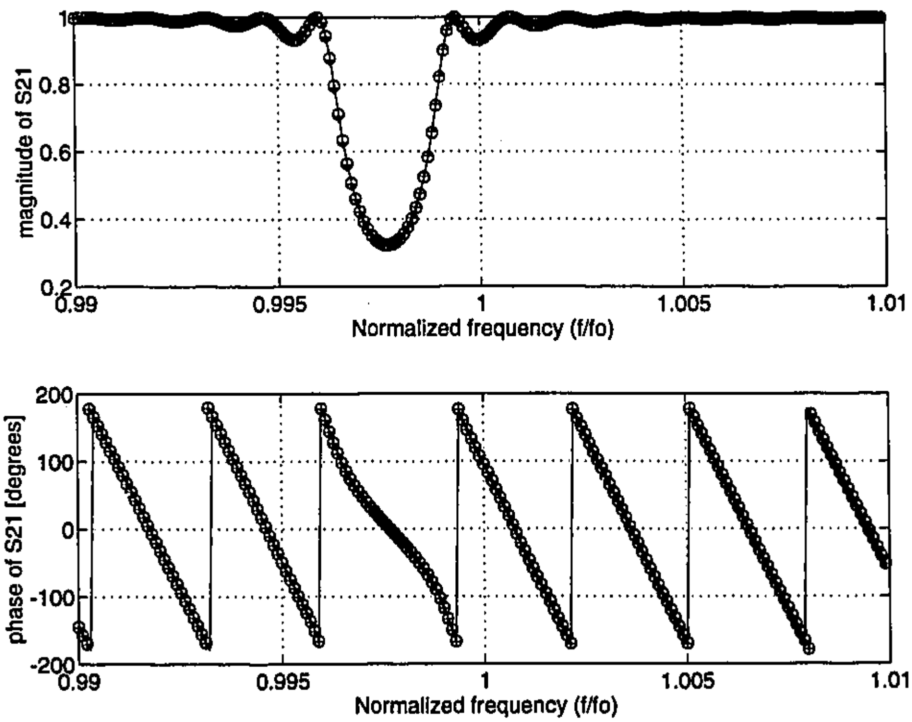

Fig. 3.3 Calculated a) magnitude and b) phase of S_{21}; network model (solid curve), COM (ooo), and GWF model (+++).

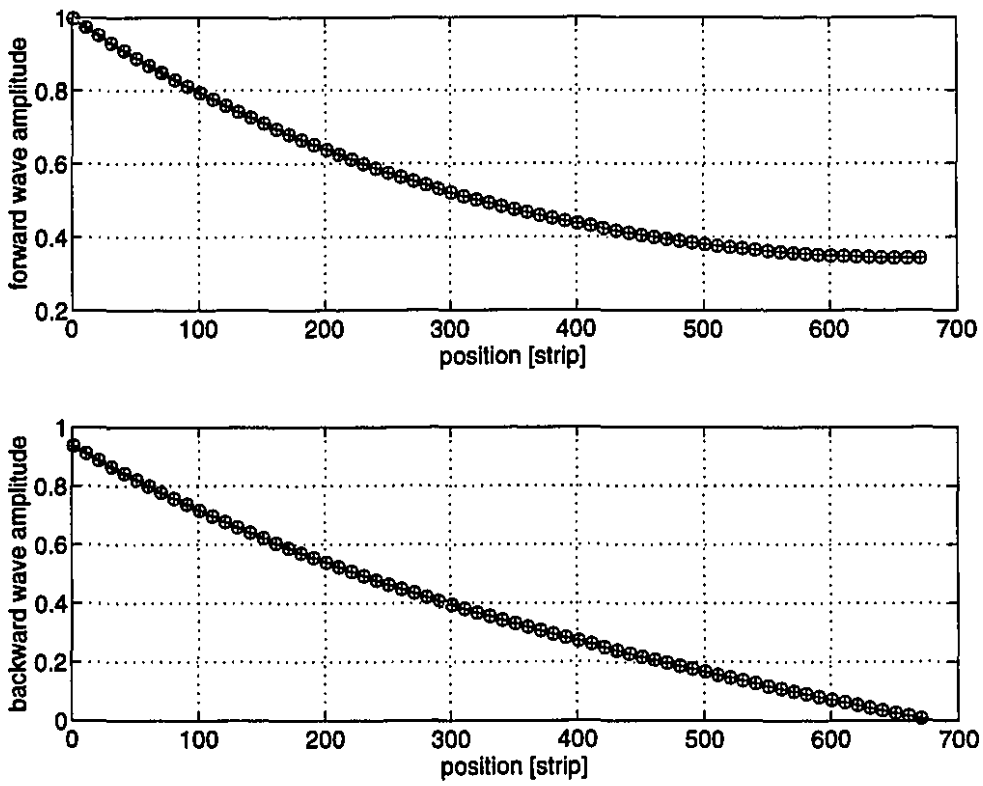

Fig. 3.4 Forward ($\bar{R}$) and backward ($\bar{S}$) wave amplitudes as a function of position, at f_n=0.998, with the incident forward wave amplitude normalized so that it carries unit power; network model (solid curve), COM (ooo curve), and GWF model (+++ curve).

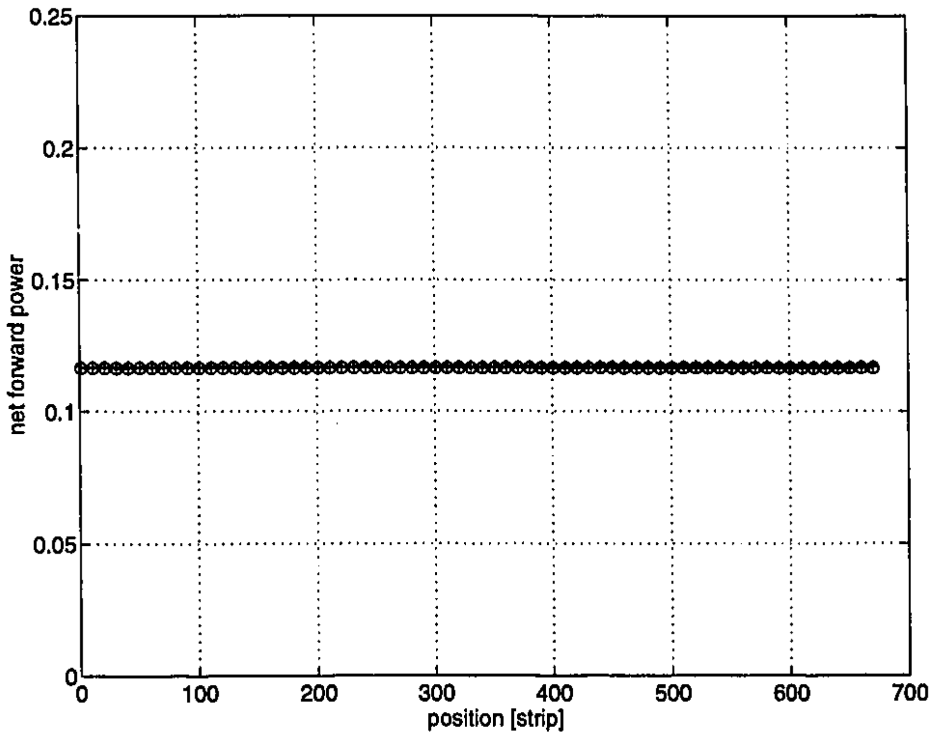

Fig. 3.5 Net forward power, $|\bar{R}|^2-|\bar{S}|^2$, in the short-circuited grating as a function of position (incident forward wave amplitude normalized so that it carries unit power); network model (solid curve) COM model (ooo curve), and GWF (+++ curve).

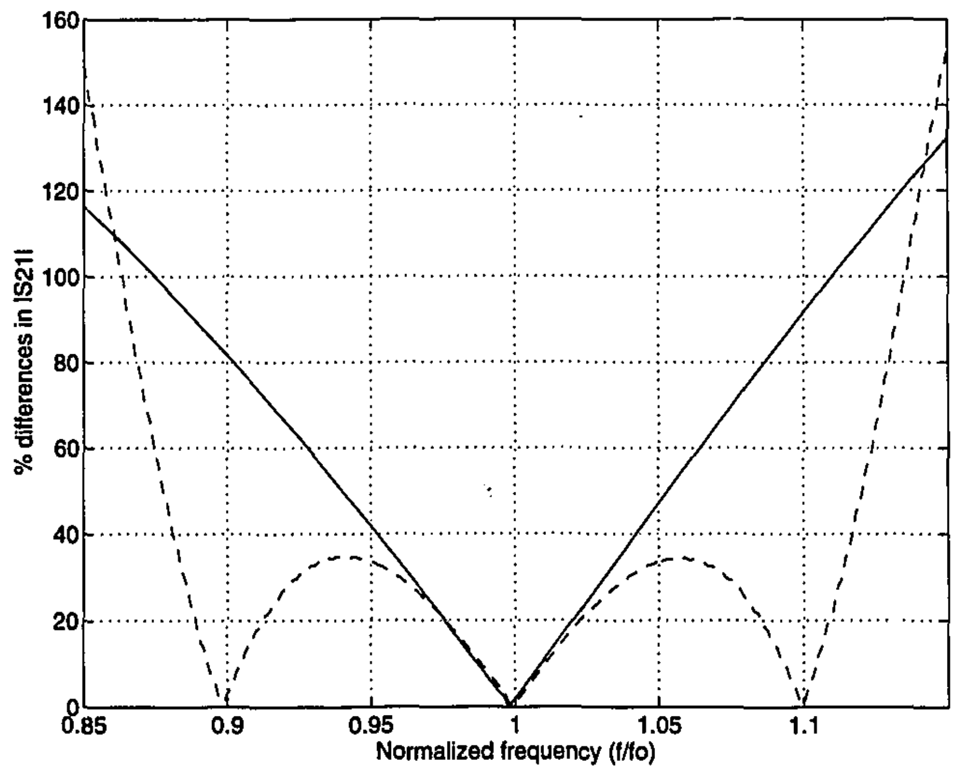

Fig. 3.6 Percentage differences, over 30% frequency band with respect to network model, for the magnitude of the calculated differences with the COM model (solid curve) and the GWF model (broken curve).

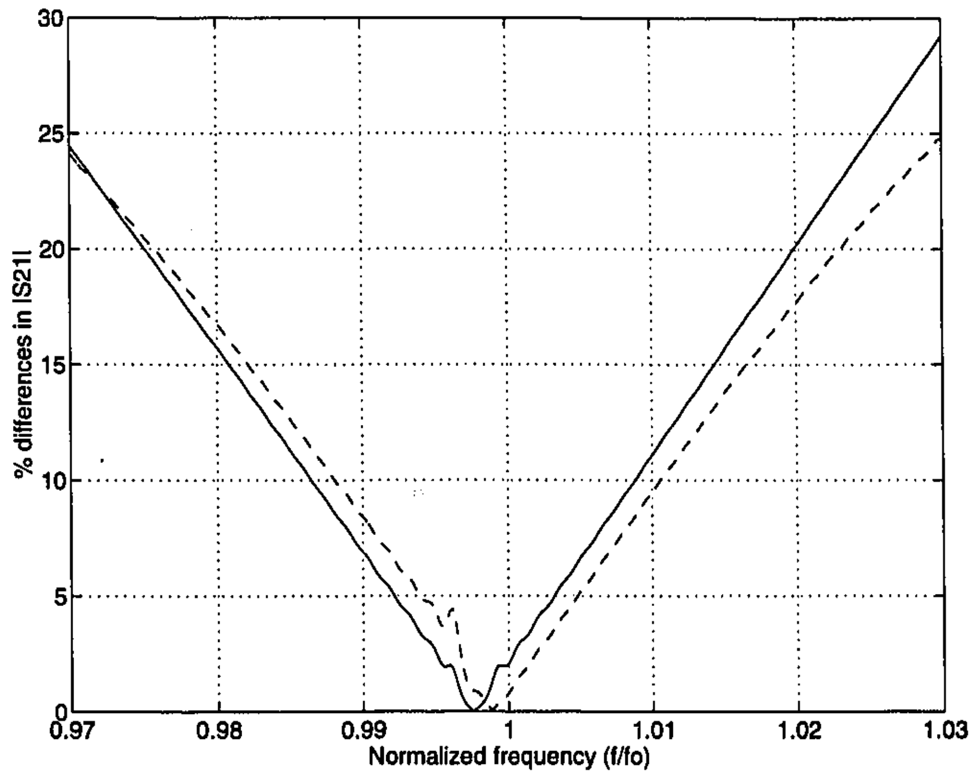

Fig. 3.7 Same as Fig. 3.6, but shown over a 6% frequency band.

3.8.2 Frequency responses for the COM parameters

In addition to verifying over what bandwidth the COM and GWF models can be used with acceptable accuracy, one may ask whether useful explicit formulas exist which may provide wider band analysis capabilities. Certainly it can be argued that no one is interested in building a grating with such bandwidths, in which case the GWF and the COM models for short-circuited gratings would apply equally well. However, if one would like to operate over wider bandwidths, such as in certain SAW bandpass filters where the interdigital transducers dictate the response, the question arises regarding how the "k" parameters behave with frequency.

Figs. 3.8 and 3.9 show how k_{11} and k_{12} vary with frequency over a 30% bandwidth, for the cases when the coefficients are calculated from the network model (Section 3.2), and according to the corrected version of the formulas [(4),(5),31] which are (3.36) or (3.39) instead of (3.41) for k_{11}, and (3.37) instead of (3.42) for k_{12}. A good agreement is obtained over a large bandwidth between the two models, with the exception of Re{k_{12}}. Fig. 3.9a shows Re{k_{12}} calculated in three different ways: the solid from the full network model, the broken one from the explicit formula (3.40), and the dash-dot one from the corrected version of [(5),31], which is (3.42) with the bracketed {} term deleted. If the {} term is maintained, the discrepancy of k_{12} with frequency is even larger further away from the normalized frequency $f_n=f/f_o=1$.

For Im{k_{12}}, Fig. 3.9b, a reasonable agreement of the order of 5% is observed; however as can be seen in Fig. 3.9a, a very large difference appears between Re{k_{12}} as calculated from the full network model and as calculated in [31]. The same difference for Re{k_{12}} is found in the case of quartz ST-X (Euler angles:[0° 132.75° 0°]), where k_{12} is pure real (Fig. 3.10). The conclusion that can be drawn from Figs. 3.9 and 3.10 is that to calculate k_{12} for larger bandwidths through an analytical expression, its dependency on b_e must be taken into consideration. This dependency is shown by the last term in the approximate expression (3.40).

It is interesting to note that for the particular NSPUDT direction chosen the reflection coefficient per strip is smaller than in the quartz ST-X by a factor of 2, leading to longer structures in order to achieve the desired reflectivity. Thus the search for other NSPUDT cuts, that can provide higher reflectivity, is certainly of great interest not only for resonators, where temperature coefficients may be a strong limitation, but also for other devices where IDT transducers play the main role.

In this section, an analysis of the short-circuited grating response has been performed based on the network model developed in this chapter. Scattering parameters frequency responses have been compared between the network model, COM, and GWF approximation predictions. For small bandwidth, which is the usual case of a short-circuited gratings, excellent agreement has been obtained, confirming the consistency between the different methods. For bandwidth larger than a few percent, errors in the COM with constant coefficients and in the GWF approximation increase rapidly. Analytical expressions for the COM parameters derived in this chapter from the GWF approximation and predicting their dependency on frequency, and on geometric and material parameters have been compared to available expressions in the literature. It has been verified that the retention of a second order term with frequency in the GWF approximation allows the analytical COM parameters expressions derived to match the network model predictions for bandwidth in excess of 30%.

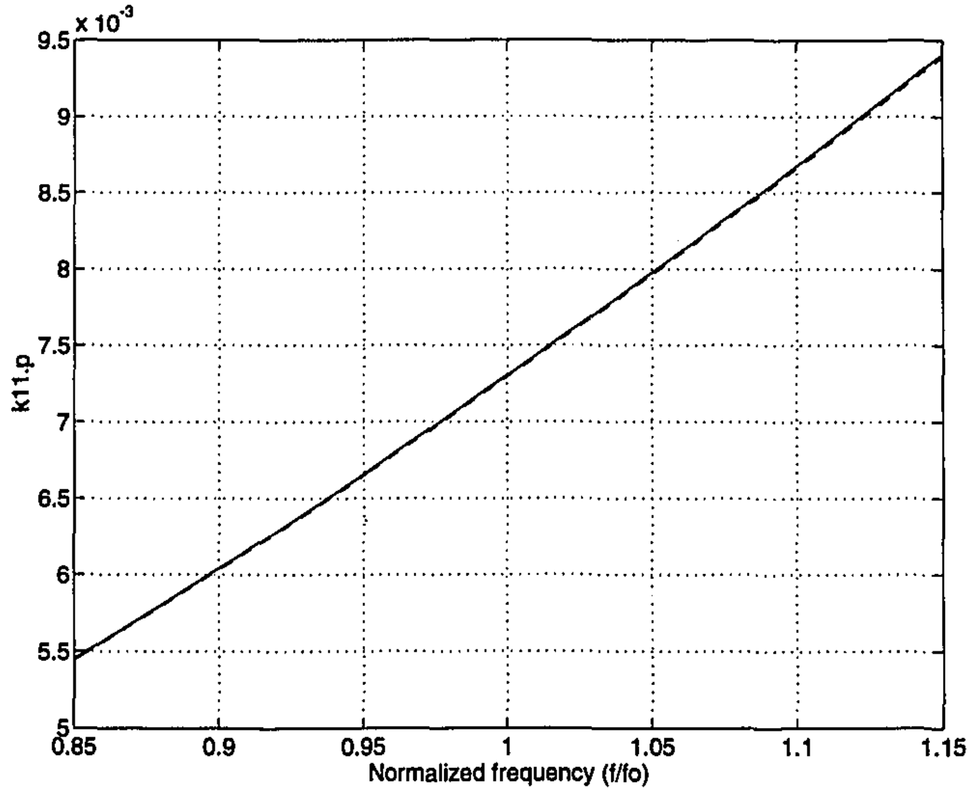

Fig. 3.8 Comparison of $k_{11}.p$ calculated from the network model (solid curve) and from a corrected version of formula given in [31] as deduced from the GWF approximation (broken curve).

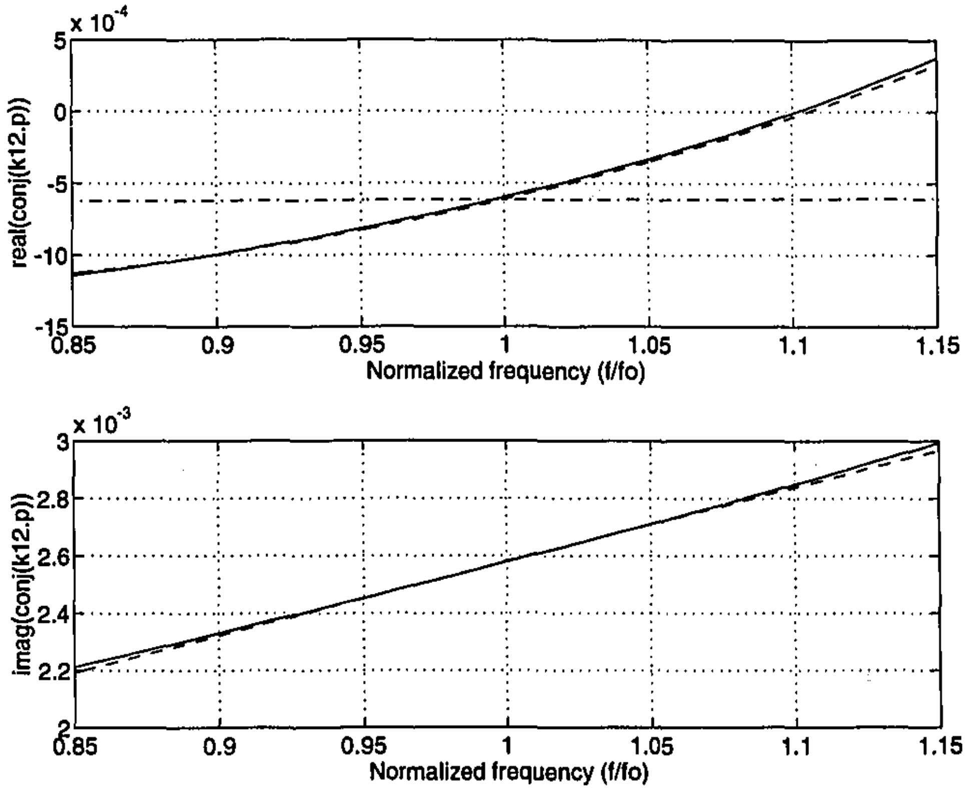

Fig. 3.9 a) Re{k_{12}.p} calculated from the network model (solid curve), the formula given in [31] (dashdot curve), and the formula obtained by extending the GWF approach (dashed curve); b) Im{k_{12}.p} from the network model (solid curve) and the corrected version of the formula given in [31] (dashed curve).

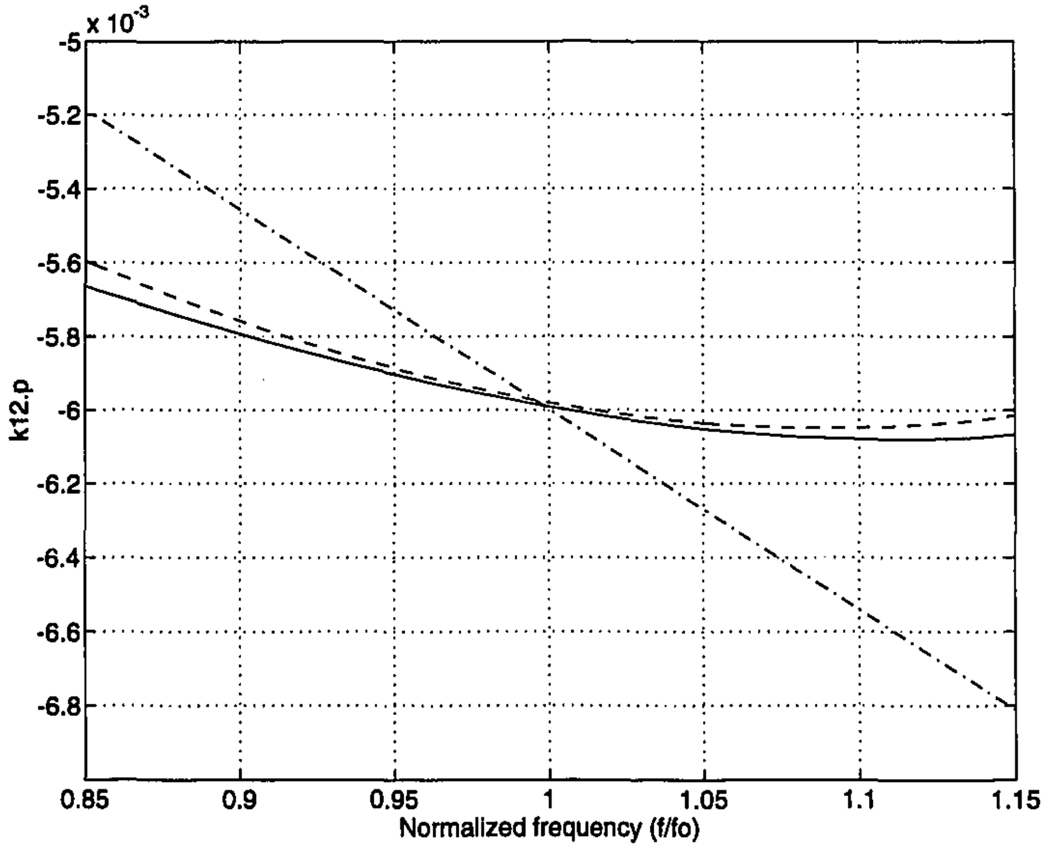

Fig. 3.10 Quartz ST-X: k_{12} is pure real; network model (solid curve), the formula given in [31] (dashdot curve), and the formula obtained by extending the GWF approach, (dashed curve).

3.9 SUMMARY AND CONCLUDING REMARKS

In this chapter the short-circuited grating structure oriented along arbitrary directions is analyzed. The scalar model developed in Chapter II for a discontinuity is extended to deal with the concept of cell and periodicity associated with the grating structure.

A generalized network model for SAW short-circuited gratings fabricated along arbitrary, and hence including both symmetric and asymmetric directions such as the NSPUDT orientations, is presented for the first time (Section 3.2).

The predictions of this model have been used to evaluate the Coupling-of-Modes phenomenological description. A procedure is outlined to calculate a "differential-from-discrete" solution, which is the basis of the Coupling-of-Modes, COM, description (Section 3.3). The fact that there exists a corresponding differential system for a periodic structure, which has a unit cell input-output matrix description for any pair of independent port-variables has been used to calculate the COM parameters directly from the network model (Section 3.6).

An approximate scalar model, the GWF approximation, is extended to account for arbitrary orientations, hence both symmetric and asymmetric orientations (Section 3.7). Using this extended model, simple explicit formulas for the ABCD matrix and therefore for the COM parameters have been derived. The retention of a second order frequency term in the GWF approximation allowed the extension of the bandwidth of the formulas derived. The COM parameter equations found have been compared to the ones quoted in the literature. The formulas derived for the COM parameters predict their dependence on frequency, on material parameters, and on geometrical parameters, and may yield results that match network model calculations for relative bandwidths in excess of 30% (Section 3.8.2). Comparison of frequency responses among the different methods, namely the network model, the COM model and the approximate model showed complete consistency. This comparison also permitted an evaluation of the limitations in frequency of the COM with constant coefficients and the GWF model with respect to the network model, which, for the quartz ST-25° example used, is about 25% in the absolute value of the percentage difference for S_{21} , for a frequency ±3% from f_o (Section 3.8.1).

In the next chapter the scalar network model is extended to describe IDT structures oriented along arbitrary propagating directions (symmetric and asymmetric orientations). This modelling provides a powerful tool to increase the insight in device design and analysis, which has historically been done along asymmetric orientations only through the COM description.

CHAPTER IV

ARBITRARILY ORIENTED INTERDIGITAL TRANSDUCER

4.1 INTRODUCTION

In Chapter II a network model for arbitrarily oriented SAW structures based on reflection coefficient calculations was given. Discontinuity effects due to metal layers were discussed and network parameters defined according to the geometry of the structure. In Chapter III this model was used successfully to represent a short-circuited grating.

In this chapter, this scalar network model is extended further to describe interdigital transducers (IDTs), where an excitation voltage is present, and to describe open-circuited gratings, where induced voltages exist along the propagation direction.

The structures discussed in this chapter consist of a primary geometrical pattern repeated in space, called a "cell", as was the case for the short-circuited grating in the previous chapter. In this thesis only the regular two fingers per wavelength IDT type, simply called "regular IDT", and the split-finger transducer type are discussed. Although the analysis presented concentrates on the regular and the split-finger IDTs, the unit-cell-based model is quite general and applies to any IDT geometry and material orientation.

Good physical insight into the structure's characteristics is obtained from the scalar model developed, since only ordinary network elements are combined in accordance with the IDT geometry.

In Section 4.2 the IDT structure oriented along arbitrary directions is introduced, and in Sections 4.3 and 4.4 the development of the Network Model for the regular IDT and the split-finger IDT, respectively, are given. In Section 4.5 power conservation, input admittance and directivity effects are considered, and in Section 4.6 a method for finding high directivity orientations is outlined. In Section 4.7, the COM description reviewed in

Chapter III is generalized to include transducers, and the "third" COM coefficient is calculated from the network model. Section 4.8 discusses first order approximations to the IDT models. In Section 4.9 the network model developed is used to calculate the performance of a complete delay line structure, taking advantage from the transmission matrix formulation adopted. Section 4.10 describes the open-circuited grating. Numerical and experimental results are presented in Section 4.11. Section 4.12 is devoted to some concluding remarks.

4.2 THE INTERDIGITAL TRANSDUCER - INITIAL CONSIDERATIONS

As previously mentioned the IDT network models available to date are scalar approximations which model IDT structures as sections of transmission lines, coupled through a transformer to an electrical port [14,13,29,15]. Most models do not include lumped susceptances to account for reflections at the metal finger-edge discontinuities and simpler models do not even take into account differences in velocities and "wave impedances" between free and metallized regions. Such additional simplifications further restrict the applicability of these models.

Another important restriction of these network models is that they use symmetrical network topologies, and therefore they work well only along symmetric orientations. For an arbitrarily oriented IDT structure where reflections due to strip discontinuities must be accounted for, this bilateral symmetry property does not apply, and some directivity in the transduction must exist, i.e., more power is launched in one direction with respect to the other. Recently, directivities of the order of 12 dB have been measured for quartz (Euler angles: 0° 132.75° 25°) [31,34], which is a high directivity or NSPUDT direction. In light of the preceding considerations, the need for, and usefulness of, an IDT Network Model which applies for arbitrary material orientations is evident.

In the next section, a simple and accurate IDT Network Model which accounts for the asymmetry along arbitrary orientations is described.

4.3 THE REGULAR IDT

To account successfully for the non-symmetrical behaviour of arbitrarily oriented IDTs the bilateral symmetry constraint in any model must be removed. It is shown in this chapter that the required asymmetry is inherent in the upstep reflection coefficient (Γ_u) calculation, discussed in Chapter II. On creating a network model to describe the metallic strip/layer discontinuity problem on arbitrary orientations (Fig. 2.6), it was shown that the symmetry of the network is destroyed by the introduction of shunt susceptances $+B_r$ at the finger upstep and $-B_r$ at the finger downstep [52].

The scalar network model given in Section 2.7 (Fig. 2.6) and used to study the grating structure in Chapter III (Fig. 3.1), serves precisely the purpose of characterizing this non-symmetrical feature of the IDT, and is incorporated in the present proposed IDT model [53]. As in the case of the grating structure, the acoustical part of the IDT cell is represented by alternating sections of unperturbed and perturbed regions, modelled by transmission lines of different characteristic impedances and velocities, with lumped discontinuities at the transitions between regions, as indicated in the center part of Fig. 4.1. An IDT cell contains all the elements of the shorted grating cell. The new variable is the applied voltage, which is, of course, zero in a shorted grating.

The IDT structure is shown in the upper part of Fig. 4.1. Although the primary cell can be connected in any desired fashion to the positive and negative bus bars, the analysis in this section is restricted to the regular IDT structure at the top of Fig. 4.1, having two fingers per wavelength with opposite polarities. The lower part of Fig. 4.1 shows the proposed model for a half-period IDT cell oriented along an arbitrary direction. The cell shown is assumed to be connected to the positive polarity bus-bar.

The electromechanical coupling is taken into account for each IDT half-period p with a transformer in a Mason-like fashion [82], according to the finger polarity. The transformer secondary is connected at the extremities of the acoustic transmission line sections of the IDT cell; the primary is connected to the electrical bus bar. The negative electrode cell is obtained by reversing the transformer secondary polarization, which is equivalent to reversing the sign of n.

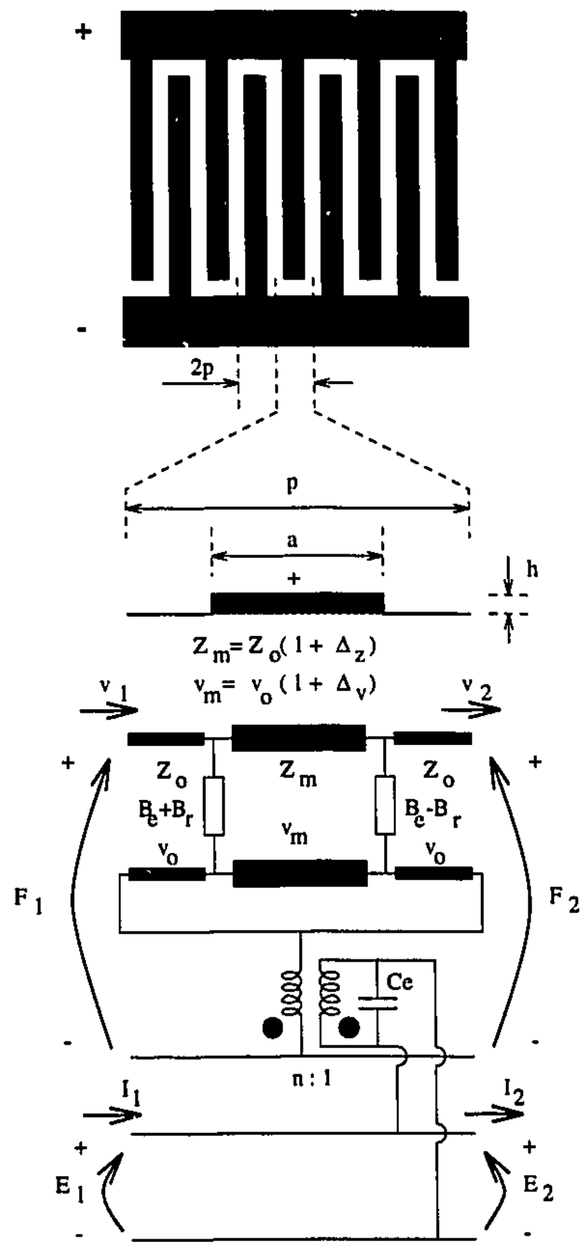

Fig. 4.1 Regular IDT structure and the corresponding network model for a positive polarity half-period cell.

The transformer ratio n is taken to be given by the same relation as in Smith's paper [14] with the characteristic mechanical impedance, Z_0, set to unity, namely

$$n = \left(\frac{v_o C_e k_{eff}^2}{p} \right)^{\frac{1}{2}} \tag{4.1}$$

where v_o is the acoustic velocity in the free region, C_e is indicated in Fig. 4.1 and represents the IDT capacitance per half-period p (unit: farad), and k_{eff} is calculated considering the periodicity of the structure [65].

Since it is desired to cascade cells having alternating polarities, it is convenient to describe them by means of a 4x4 transfer matrix [13]. The transfer matrix variables, F_i , v_i , E_i, I_i, i=1,2, shown in Fig. 4.1, represent the mechanical variables and the electrical variables. From basic network theory the resulting transfer matrix description for the half-period circuit in Fig. 4.1 is given by

$$\begin{bmatrix} F_1 \\ v_1 \\ E_1 \\ I_1 \end{bmatrix} = \begin{bmatrix} A & B & -n(1-A) & 0 \\ C & D & nC & 0 \\ 0 & 0 & 1 & 0 \\ nC & -n(1-D) & (n^2C+j\omega C_e) & 1 \end{bmatrix} \begin{bmatrix} F_2 \\ v_2 \\ E_2 \\ I_2 \end{bmatrix} = T(n) \begin{bmatrix} F_2 \\ v_2 \\ E_2 \\ I_2 \end{bmatrix} \tag{4.2}$$

where A, B, C, D are the 2x2 mechanical transfer matrix elements describing the short-circuited grating model and given explicitly in section 3.2, equations (3.6) to (3.9). The full IDT transfer matrix for a period 2p is then given by **T=T(n)T(-n)**. The full transducer is therefore described by cascading the appropriate number of cell transfer matrices.

For the proposed model, it is opportune to reiterate that all the information necessary to account for the asymmetry in an arbitrary orientation is contained in the model parameter B_r ($-B_r$), which comes from the calculation of the upstep (downstep) reflection coefficient. With respect to the grating model, the additional network parameters included to account for the piezoelectric transduction are C_e and n.

4.4 THE SPLIT-FINGER IDT

For completeness and for comparison with experimental data for the delay line (one regular and one split-finger IDT) discussed in Section 4.11 the split-finger structure is also analyzed. In this structure (Fig. 4.2) the IDT cell is built by acoustically cascading two fingers having the same polarity, which is equivalent to multiplying the 2x2 matrices corresponding to the acoustic part alone. This defines a new 2x2 transfer matrix **T'(n')** with parameters A', B', C' and D', to replace A, B, C and D in (4.2). For the transformer ratio n', values of C'_e and k'_{eff} corresponding to the split finger IDT must be used in (4.1) [65]. The lower part of Fig. 4.2 shows the model for the split-finger IDT.

With the modifications mentioned above, a full IDT period 2p is again represented by multiplying the two transfer matrices **T'(n')** and **T'(-n')**. The full transducer is therefore obtained by cascading cells as shown in Fig. 4.2, with alternating polarities for n.

4.5 SOME IDT CHARACTERISTICS

In this section the driving point admittance impedance, the directivity evaluation, and energy conservation are discussed.

The IDT is viewed as a three port device, consisting of one electrical and two mechanical ports (Fig 4.3a). The reduction from 4 ports to 3 ports is just because, for the IDT **as a structure** (Fig. 4.1 and (4.2)), $E_1=E_2=E$, $I_2=0$ (end of the structure), and $I_1=I$. If one of the acoustic ports is match-terminated with Z_0 , the terminal acoustic variables at that specific port are eliminated and the matched port is then absorbed, allowing the IDT to be treated as a two-port network. In Fig. 4.3b the acoustic *port 1* is absorbed, and in Fig. 4.3c *port 2* is absorbed. In a regular IDT oriented along symmetric directions, it is irrelevant whether *port 1* or *port 2* is acoustically matched and absorbed. In contrast, for arbitrary orientations, symmetry no longer applies, and it is from the difference in the transmission response when *port 1* or *port 2* is matched and absorbed that the directivity described in this section is derived.

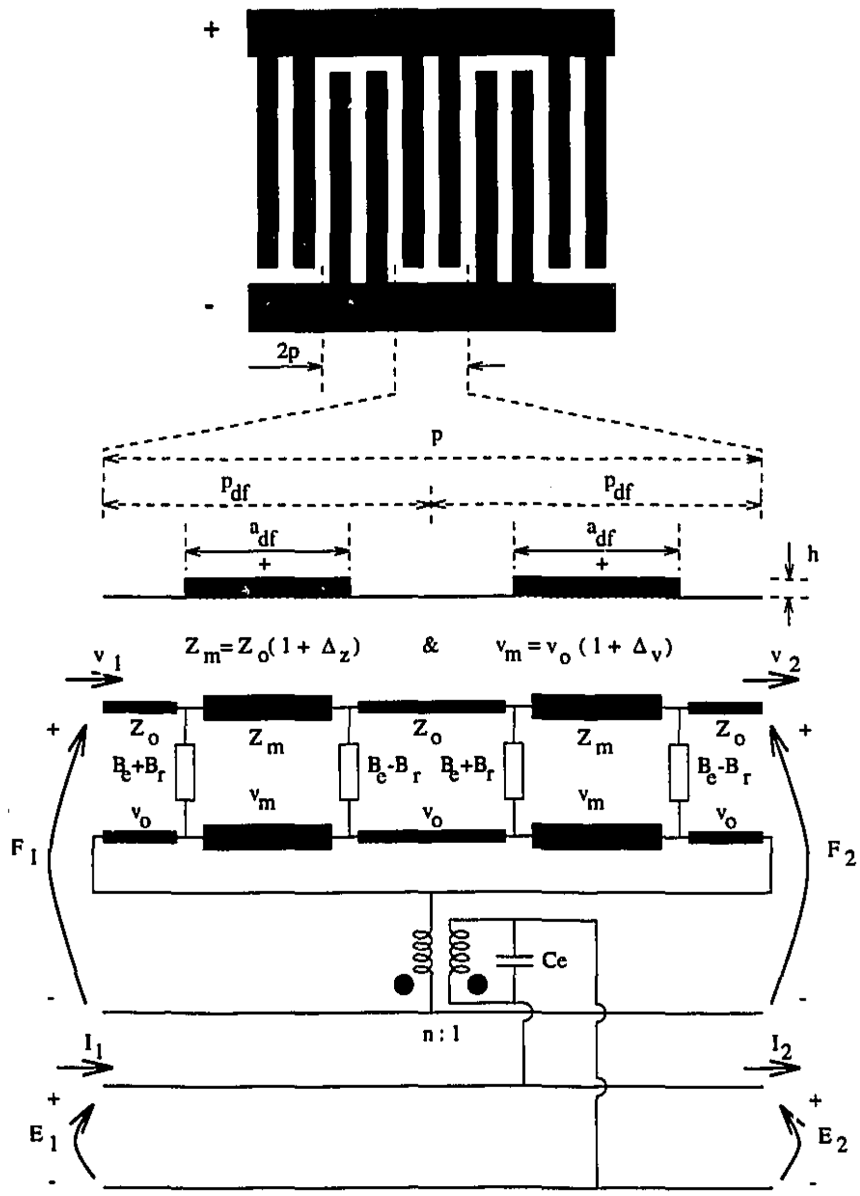

Fig. 4.2 Split-finger IDT structure and the corresponding network model for a positive polarity half-period cell.

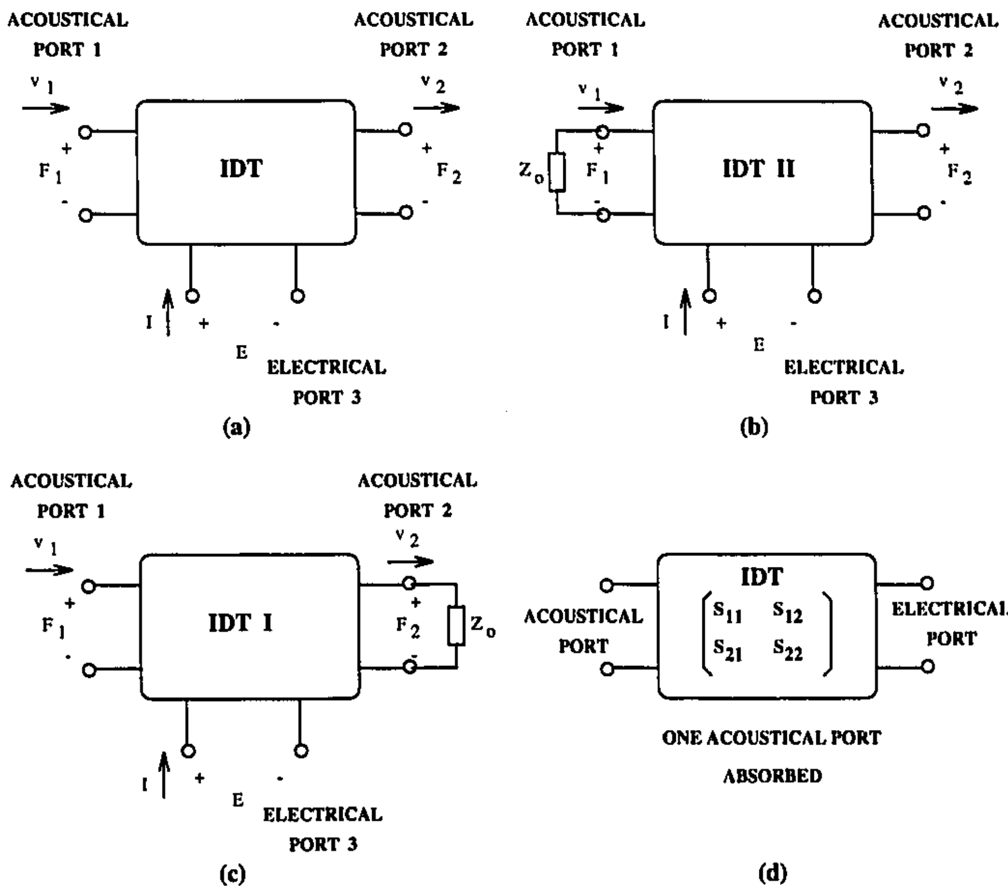

Fig. 4.3 a) IDT as a three port device; b) absorption of the acoustic port 1; c) absorption of the acoustic port 2; d) two port representation which results from the absorption of one acoustic port.

Once a two port network is established, its scattering parameter (S parameters) are calculated from the ABCD matrix using standard network theory. Here the acoustic matched impedance is taken to be $Z_o=Z_{o1}=1$, and the electrical matched impedance is taken as to be $Z_{o2}=50\Omega$. The IDT is then represented by one acoustical and one electrical port, as shown in Fig. 4.3d.

Power conservation is checked by verifying that

$$1-|S_{33}|^2 = |S_{13}|^2+|S_{23}|^2 \tag{4.3}$$

where S_{33} is the electrical port reflection coefficient, S_{13} is the transmission coefficient for the acoustic port referring to IDT I, and S_{23} is the transmission coefficient for the acoustic port referring to IDT II.

Matching acoustic ports 1 and 2, which correspond to the extreme cells of the IDT structure (Fig. 4.3a), the acoustic ports are absorbed, and the *driving point admittance* $Y_{in}=I/E$ is calculated. Defining **TI** as the 4x4 IDT overall transfer matrix obtained by cascading the ABCD matrices of the transducer cells with their proper polarity (equation (4.2)), Y_{in} is written in terms of the elements of **TI** as

$$Y_{in} = TI_{43}-\frac{(TI_{41}+TI_{42})(TI_{13}+TI_{23})}{(TI_{11}+TI_{12}+TI_{21}+TI_{22})} \tag{4.4}$$

Still considering both acoustic ports matched as in the previous paragraph, *directivity* is defined as the ratio between the power going to the "right" (direction of the forward wave, positive x axis direction) and the power going to the "left" (direction of the backward wave, negative x axis direction). In terms of the 4x4 IDT transfer matrix **TI** defined in the previous paragraph, the directivity is expressed as

$$Dir = \frac{P_R}{P_L} = 20\log\left|\frac{(TI_{13}+TI_{23})}{TI_{13}(TI_{21}+TI_{22})-TI_{23}(TI_{11}+TI_{12})}\right| \tag{4.5}$$

The above expressions for the driving point admittance and the directivity are compared to experimental data in Section 4.11.

4.6 HIGH DIRECTIVITY (NSPUDT) ORIENTATIONS

At the end of last section an expression is given (4.5) for the directivity of a transducing structure. In this section, the directivity phenomenon is examined from a "physical" point of view by investigating the reflections in the structure. This discussion leads to a procedure for finding and maximizing high directivity orientations in a material in a chosen plane.

Consider Fig. 4.4, which applies when energy storage effect is neglected. In this figure, the reflection coefficients for counterpropagating waves at locations 1 and 3 are shown as the conjugates of the reflection coefficients Γ_d and Γ_u , respectively. This property was demonstrated in Chapter II; the question asked here is: what can be said with respect to the phase of Γ_u , Γ_d , and the propagation phase shift of a half strip length (a/2) in the metallized region, $\bar{\phi}=\omega a/2v_m$, in order to have maximum power going to the right (+x direction), and consequently minimum power going to the left (-x direction)? By finding such relations, strategies for identifying high directivity orientations and therefore appropriate materials and cuts are formulated.

For maximum power going to the right, the wave that goes to the right must be exactly **in phase** with the reflected waves at locations 1 and 3 of Fig. 4.4, and the wave that goes to the left must be **180° out of phase** with the reflected waves at locations 2 and 4. These requirements are given by

$$-2\bar{\phi} + \angle(\Gamma_d^*) = 0 \tag{4.6a}$$

$$-2\bar{\phi} + \angle(\Gamma_d) + 180° = 0 \tag{4.6b}$$

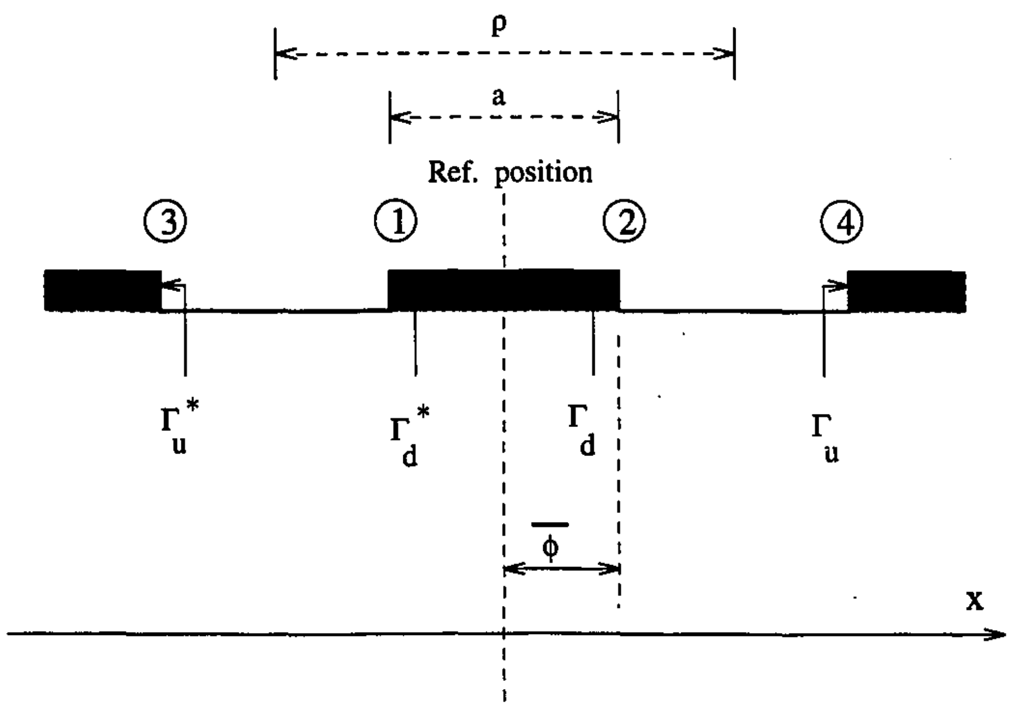

Fig. 4.4 Locations of reflections due to discontinuities in the IDT structure (energy storage effect neglected in this figure).

and

$$\angle(\Gamma_u^*) - 2\frac{\omega}{v_o}(p-a) = \angle(\Gamma_d^*) \tag{4.7a}$$

$$\angle(\Gamma_u) - 2\frac{\omega}{v_o}(p-a) = \angle(\Gamma_d) \tag{4.7b}$$

Solving (4.6a) and (4.6b) one gets, to within ± 180°

$$\angle(\Gamma_d) = -90^\circ \tag{4.8a}$$

$$\bar{\phi} = \frac{\omega a}{2v_m} = 45^\circ \tag{4.8b}$$

From (4.7) and (4.8), one arrives at

$$\angle(\Gamma_u) = 90^\circ \tag{4.9}$$

Therefore (4.8) and (4.9) fix the conditions for the search of high directivity orientations and also, through $\bar{\phi}$, the optimum IDT geometry. In terms of the network model parameters, (4.8) and (4.9) can only be satisfied if the following inequality constraints hold

$$|\Delta_z| \ll |b_r| \ll 1 \tag{4.10}$$

where $b_r = Z_0 B_r$.

It can be shown that inclusion of energy storage effects through B_e does not affect these conclusions. Clearly, since (4.8b) can only be satisfied exactly at a single frequency $v_m/4a$, high directivity is achievable only across a finite bandwidth.

In summary, the proposed model helps in understanding the high directivity (NSPUDT) operation. Since Γ_u depends uniquely on the layer material and on the SAW properties in the substrate, (4.8) and (4.9) are used as guidelines for finding new high directivity orientations. Some numerical examples and results for the search method described above are discussed in Section 4.11.

A high directivity application

To illustrate a high directivity or NSPUDT orientation application, one can refer to the resonator devised by P. Wright [66].

In a regular two-port one-pole resonator **oriented along symmetric directions**, an input and an output IDT are located between two gratings, as shown in Fig. 4.5a. Low-cost commercial resonators consist of aluminium film deposited gratings and transducers, with typical metallization ratio of η=0.5, and the distance between the inner strips of the gratings (cavity length) as $n\lambda_R/2$; λ_R here, the resonant frequency.

The placement of the transducers inside the cavity is of importance in such devices, since the IDT themselves act as reflectors. If the IDT is placed periodically, as a natural sequence of the grating, Fig. 4.5b, there is the evident advantage that the IDT fingers discontinuities reflect in phase with the grating and do not disturb the cavity response (synchronous placement). This scheme also results in small cavity lengths, which turns out to be another advantage since spurious cavity resonances are moved further away from the passband. A disadvantage of the synchronous scheme is the fact that the synchronously placed transducers are not maximally coupling to the standing wave implying higher insertion losses, or equivalently lower Q, as can be noted from the standing wave pattern drawn in Fig. 4.5b. Another disadvantage, is the fact that a lower frequency resonance peak occurs since the IDTs will couple even stronger to it; at a high frequency a null takes place (Fig. 4.5b).

If the asynchronous scheme is adopted so that the transducers couple maximally to the standing wave (Fig. 4.5c), the IDTs reflections are no longer in phase with the grating reflection and spurious resonances appear. Additionally, there is an increased complexity in the mask design, device fabrication, and an increased sensitivity to the thickness of the layer [66].

The resonator structure on a high directivity orientation is shown in Fig. 4.5d, with the IDTs and gratings synchronously placed. While retaining the synchronous placement advantages mentioned before, the NSPUDT resonator naturally avoids the disadvantages of non-maximal coupling. At NSPUDT orientations the standing wave pattern is shifted 45°, or equivalently the reflection coefficient $\angle\Gamma_u = 90° = -\angle\Gamma_{ubk}$ (Fig. 4.5c) as discussed earlier in this section. Note that the transducers must be at the same side of the small cavity, so that both are maximally coupled at the resonance.

4.7 THE COM DESCRIPTION

In Chapter 3 the coupling-of-modes description is given as a set of two differential equations with constant coefficients, in variables $\bar{R}$ and $\bar{S}$, and with voltage V_G, the strip voltage and input forcing function. The COM equation given by (3.19) is repeated below for convenience.

$$\frac{d}{dx}\begin{bmatrix}\bar{R}(x)\\ \bar{S}(x)\end{bmatrix} = \begin{bmatrix} -j(k_{11}+\delta) & -jk_{12} \\ jk_{12}^{*} & j(k_{11}+\delta)\end{bmatrix}\begin{bmatrix}\bar{R}(x)\\ \bar{S}(x)\end{bmatrix} + \begin{bmatrix} j\alpha \\ -j\alpha^{*}\end{bmatrix} V_G(x)$$

The solution to the above equation is written as the sum of the "zero-input" or homogeneous solution (unforced, $V_G=0$), of specific interest for short-circuited gratings, and of the "zero-state" or particular solution ($V_G \neq 0$). For compactness and facility in describing the IDT as a three-port network (Fig. 4.6), the solution is written as a set of three equations

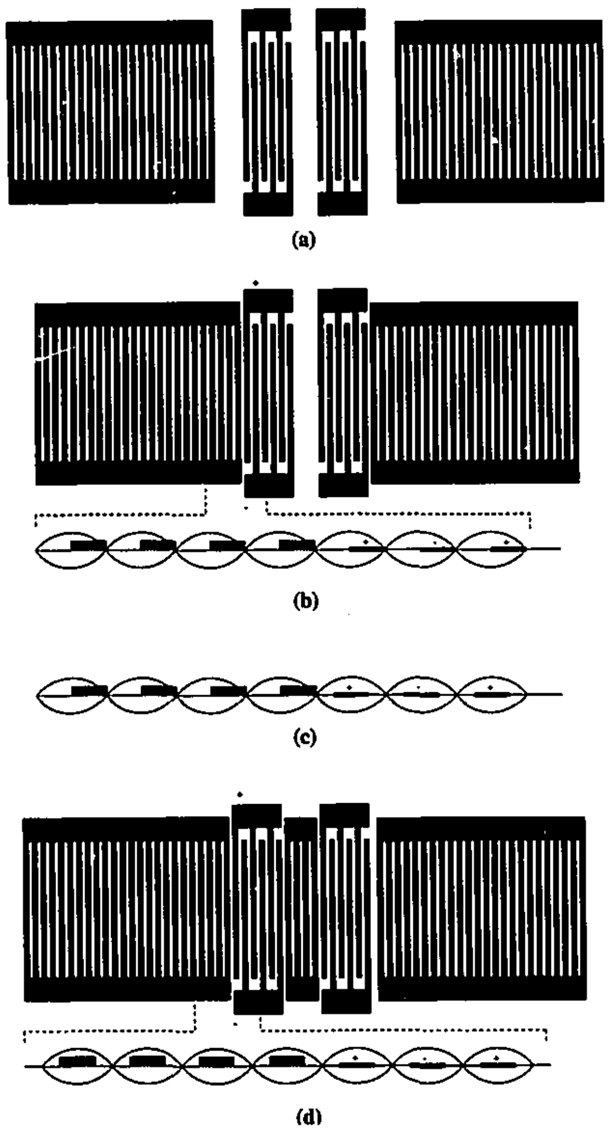

Fig. 4.5 a) Regular two-port one-pole resonator; b) Synchronous placement of the IDTs and standing wave diagram; c) standing wave diagram for asynchronous placement of the IDTs; d) NSPUDT resonator structure [66].

$$
\begin{bmatrix} \bar{R}(x) \\ \bar{S}(x) \\ I(x)-I(0) \end{bmatrix} = B(x) \cdot \begin{bmatrix} \bar{R}(0) \\ \bar{S}(0) \\ V_G \end{bmatrix} \tag{4.11}
$$

where

$$
B(x) = \begin{bmatrix} b_{11} & b_{12} & b_{13} \\ b_{12}^{*} & b_{11}^{*} & b_{13}^{*} \\ b_{31} & -b_{31}^{*} & b_{33} \end{bmatrix} \tag{4.12}
$$

The equations for the matrix elements of $\mathbf{B(x)}$ are given by

$$
b_{11} = \cosh(\lambda_1 x) - j\frac{(k_{11}+\delta)}{\lambda_1}\sinh(\lambda_1 x) \tag{4.13}
$$

$$
b_{12} = -j\frac{k_{12}}{\lambda_1}\sinh(\lambda_1 x) \tag{4.14}
$$

$$
b_{13} = \frac{\xi}{\lambda_1^2}[\cosh(\lambda_1 x)-1] + j\frac{\alpha}{\lambda_1}[\sinh(\lambda_1 x)] \tag{4.15}
$$

$$
b_{31} = 2\frac{\xi^{*}}{\lambda_1^2}[\cosh(\lambda_1 x)-1] + j2\frac{\alpha^{*}}{\lambda_1}[\sinh(\lambda_1 x)] \tag{4.16}
$$

$$
b_{33} = j\left\{\frac{4Re[\alpha.\xi^{*}]}{\lambda_1^3}.[\sinh(\lambda_1 x)-x\lambda_1] - x\omega C_e\right\} \tag{4.17}
$$

with

$$\lambda_1 = [\,|k_{12}|^2 - (k_{11}+\delta)^2]^{\frac{1}{2}}$$

and

$$\xi = \alpha(\delta + k_{11}) - k_{12}\alpha^*$$

The calculation of the parameters k_{11} and k_{12} from the network model was described in Section 3.6. The only COM parameter yet to be determined is α, the transduction coefficient, which has been the subject of a number of recent papers [67,68].

A straightforward way of finding α is to identify the COM short-circuit current equation from the third row of (4.11) with the corresponding network model short-circuit current equation (fourth row of (4.2)), yielding a complex α

$$\alpha = \alpha_r + j\alpha_i \tag{4.18}$$

with

$$\alpha_r = \frac{j\dfrac{nC}{2} - \dfrac{n[\cosh(\lambda_1)-1](A-1)(\delta+k_{11}+k_{12r})}{2\{\lambda_1\sinh(\lambda_1)+k_{12i}[\cosh(\lambda_1)-1]\}}}{-\dfrac{k_{12i}[\cosh(\lambda_1)-1]}{\lambda_1^2} + \dfrac{\sinh(\lambda_1)}{\lambda_1} + \dfrac{[\cosh(\lambda_1)-1]^2[(\delta+k_{11})^2-k_{12r}^2]}{\{\lambda_1^3\sinh(\lambda_1)+\lambda_1^2 k_{12i}[\cosh(\lambda_1)-1]\}}} \tag{4.19}$$

$$\alpha_i = \frac{n\lambda_1^2(A-1) + 2\alpha_r[\delta+k_{11}-k_{12r}][\cosh(\lambda_1)-1]}{2\{\lambda_1\sinh(\lambda_1)+k_{12i}[\cosh(\lambda_1)-1]\}} \tag{4.20}$$

where complex k_{12} is written as $k_{12}=k_{12r}+jk_{12i}$, and λ_1 is the same as defined for (3.25).

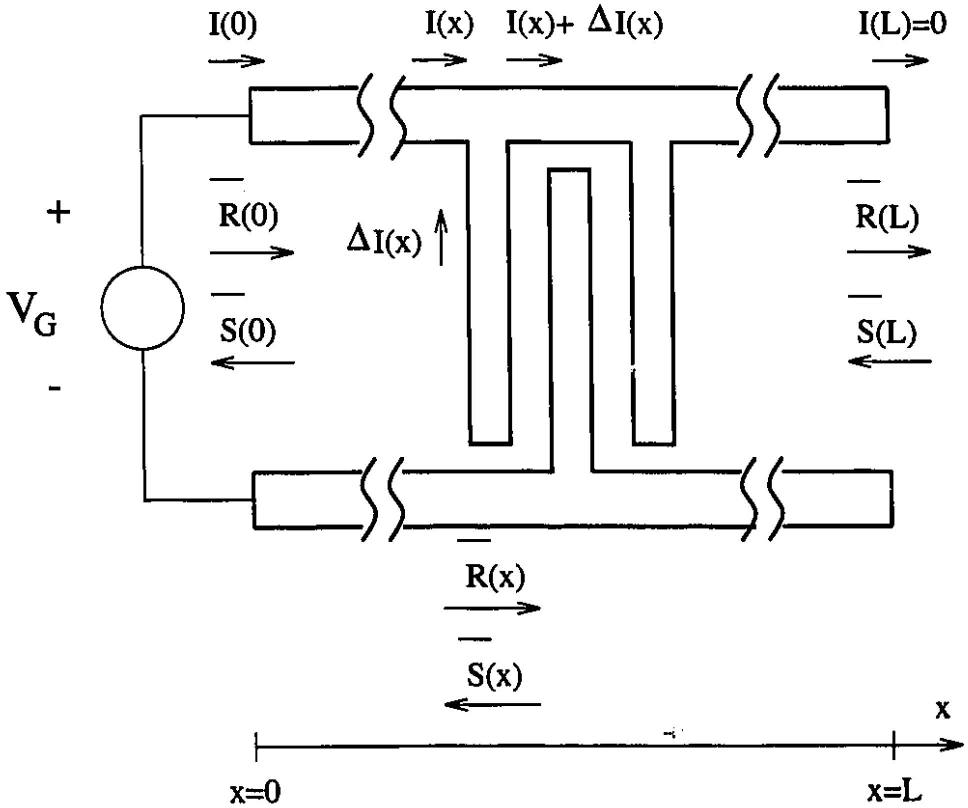

Fig. 4.6 Coupling-of-modes (COM) variables for the IDT structure.

Since (4.19) and (4.20) are rather bulky, they are approximated by means of a first order Taylor expansion around f_o, the Bragg frequency, and substitution of the first-order approximations for A, C, k_{11}, and k_{12} given in Chapter III. The procedure is discussed in the next section.

4.8 FIRST-ORDER APPROXIMATIONS

In this section the approximate network model and the COM model parameters are discussed for transducers.

4.8.1 Approximate network model parameters

For the network model cell, the simplification in calculations using (4.2) is achieved through the determination of approximate expressions for the A, B, C and D matrix elements, i.e., through (3.29), Section 3.7. These expressions are obtained by replacing the network model parameters, Δ_v, Δ_z, B_e, and B_r, with their Taylor expansions with respect to frequency and retention of only the lowest-order powers of these parameters.

When the approximate A, B, C and D matrix element values replace the exact ones, a good approximation around the frequency f_o was obtained for the grating transfer matrix, as was shown in Chapter III. This good approximation is also true for the IDT transfer matrix, as verified in Section 4.11.

4.8.2 Approximate COM parameters

With respect to the COM parameters, approximate analytical expressions for k_{11} and k_{12} have been derived in Section 3.7. What remains is to derive an approximate analytical expression for α.

This is done using the same procedure outlined in the previous Section 4.5, which led to (4.18) to (4.20), namely identifying the short-circuit current equation for COM (third row of (4.11)) with the short-circuit current equation for the cell structure. The procedure is: (i) perform a Taylor expansion of α with respect to frequency around f_o; (ii) then use the approximate expressions for the A, C, k_{11} and k_{12} elements; and (iii) retain the first-order terms. The resulting approximate equation for αp is

$$\alpha p \doteq (\alpha_r + j\alpha_i)p = n(d + \frac{b}{2}) - jn \tag{4.21}$$

For completeness, the approximate expressions for k_{11p} and k_{12p}, as given by (3.36) and (3.37) in Section 3.7, are repeated here

$$k_{11}p(f \approx f_o) = b = b_e - (\pi \frac{f}{f_o})\eta \Delta_v$$

$$k_{12}p(f \approx f_o) = d + jb_r \sin(\pi\eta) =$$
$$= (\Delta_z + jb_r)\sin(\pi\eta) - b_e \cos(\pi\eta)$$

In the above, the explicit dependence on the metallization ratio, $\eta = a/p$, is exhibited. From these approximate equations, since b and d « 1, the phase of α is close to -90° and its magnitude is close to n.

4.9 A DELAY LINE ON ARBITRARY ORIENTATIONS

From the discussion in Sections 4.5 and 4.6, the regular IDT structure oriented along arbitrary asymmetric directions presents at least some directivity at its fundamental frequency f_o, whereas the split-finger structure of Section 4.4 with $\eta = .5$ presents no directivity. Basically there is coherent reflection, which add in phase in the regular IDT, but are out of phase for the split-finger structure.

A convenient way of checking directivity at a certain frequency is to employ one regular IDT and one split-finger IDT designed to operate at their fundamental frequency

f_o. The relative position of the different IDTs is essential in detecting the non-symmetric response. The directivity is given by the ratio of the electrical transmission coefficients for the entire delay line when the regular IDT is on the left (forward propagation) with respect to the situation where the regular IDT is on the right (reverse propagation) (Section 4.5).

Other than serving the purpose of measuring directivity, this delay line is a nice example of the convenience of using transmission matrices. The cascading of the cell leads to the IDT structure as seen in Fig. 4.3, which in its turn is cascaded with other SAW structures in order to finally assemble a device, in this case a delay line, Fig. 4.7. In this figure, the transmission matrices for both transducers are represented by the blocks Q_{TI} and Q_{TII}; Q_{dl} portrays a section of transmission line (pure delay) in between the two transducers; Q_{ZP1}, Q_{YP1}, Q_{ZP2} and Q_{YP2} are *parasitic* elements which must be accounted for in most practical devices, with the Q_{ZPi} terms representing the transmission matrix for a series impedance, and the Q_{YPi} terms representing the transmission matrix for a parallel admittance; finally, in this example, Q_{ZM1} and Q_{ZM2} represent the transmission matrix for a series impedance, usually an inductor, basically used to resonate the IDT static capacitance. As depicted in Fig. 4.7, the transmission matrix for the full delay line, Q_{DL} , is built by simply multiplying the transmission matrix of each individual block. The scattering parameters for the full delay line are calculated from Q_{DL} , assuming Z_{oELEC}=50Ω at both terminal electrical ports.

In Section 4.11 delay line numerical simulations are presented and their results compared experimental data.

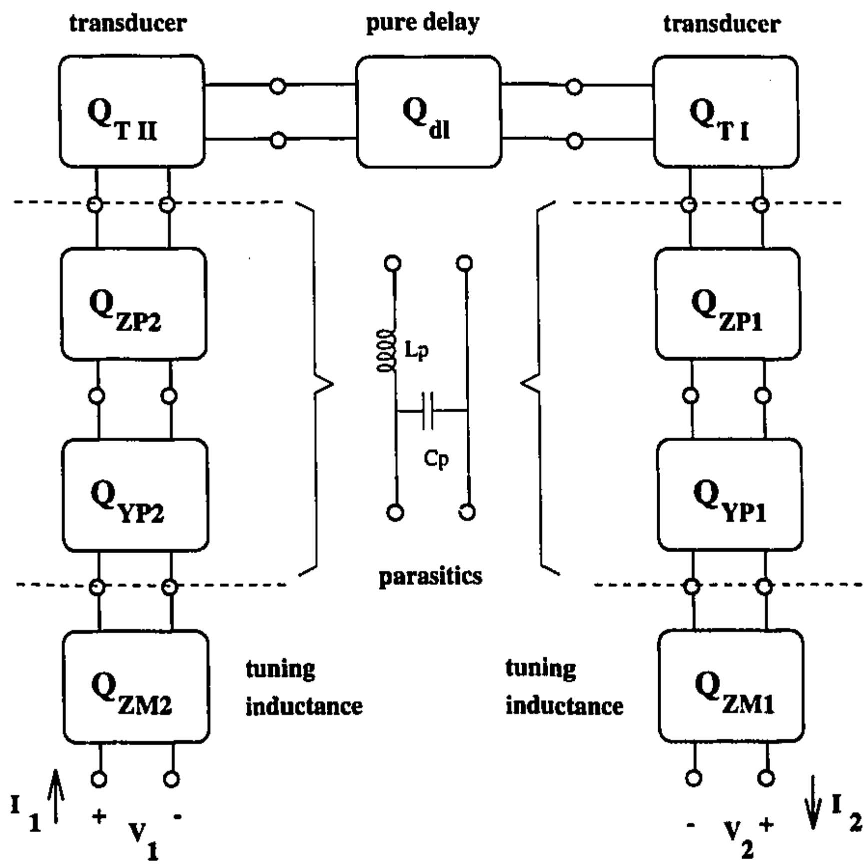

$$Q_{DL} = Q_{ZM2} \cdot Q_{YP2} \cdot Q_{ZP2} \cdot Q_{T\,II} \cdot Q_{dl} \cdot Q_{T\,I} \cdot Q_{ZP1} \cdot Q_{YP1} \cdot Q_{ZM1}$$

Fig. 4.7 Transmission matrix blocks used for constructing a SAW delay line.

4.10 OPEN-CIRCUITED GRATINGS

4.10.1 Network Model

The analysis of the open-circuit grating structure is not as simple as the short circuited grating for the reason that the voltage at all the strips are no longer the same. The open-circuited grating is, however, just a special case of the IDT. Referring to Fig. 4.1, the IDT cell is used to represent an open-circuited grating cell with $I_1=I_2=0$ and $E_1=E_2=E$. Imposing these conditions in (4.2), one gets for the open-circuited grating

$$\begin{bmatrix} F_1 \\ v_1 \end{bmatrix} = \frac{1}{1+\bar{\rho}C} \begin{bmatrix} A+\bar{\rho}C & B+\bar{\rho}(A+D-2) \\ C & D+\bar{\rho}C \end{bmatrix} \begin{bmatrix} F_2 \\ v_2 \end{bmatrix} \tag{4.22}$$

where $\bar{\rho}=n^2/j\omega C_E$, n and C_E specified in (4.1), and the A, B, C and D parameters are as given in Section 3.2 for the short circuited grating. Therefore (4.22) defines the transmission matrix for the open-circuit grating, where other than the same ABCD elements which determine the transmission matrix for the short circuited grating, n and C_E are required. Also, instead of employing the full expressions for the ABCD elements derived in Section 3.2, the GWF approximated ABCD elements derived in Section 3.7 for arbitrary directions can be used, thus providing approximate analytical expressions for the transmission matrix in (4.22).

4.10.2 Coupling-of-Modes

In Section 4.6, the COM equation (3.19), was solved for the IDT, in which case V_G was assumed *constant* with respect to the propagating direction x. This is not the case for an open-circuited grating, where V_G is a function of x, $V_G(x)$.

The COM equation for the incremental current [31,60] according to the polarity convention adopted in Fig. 4.6 is given by

$$\frac{dI(x)}{dx} = j2\alpha^{*}\bar{R}(x) + j2\alpha\bar{S}(x) - j\frac{\omega C_e}{p}V_G(x) \tag{4.23}$$

Recalling that for the open circuit grating I(x)=0, $V_G(x)$ are readily determined from (4.23) in terms of $\bar{R}$ and $\bar{S}$, and substituted in (3.19), leading to

$$\frac{d}{dx}\begin{bmatrix}\bar{R}(x)\\ \bar{S}(x)\end{bmatrix} = \begin{bmatrix} -j(k_{11}+\delta)+\dfrac{j2|\alpha|^2}{\omega C_e/p} & -jk_{12}+\dfrac{j2(\alpha)^2}{\omega C_e/p} \\ jk_{12}^{*}-\dfrac{j2(\alpha^{*})^2}{\omega C_e/p} & j(k_{11}+\delta)-\dfrac{j2|\alpha|^2}{\omega C_e/p}\end{bmatrix}\begin{bmatrix}\bar{R}(x)\\ \bar{S}(x)\end{bmatrix} = K_{oc}\begin{bmatrix}\bar{R}(x)\\ \bar{S}(x)\end{bmatrix} \tag{4.24}$$

The advantage of making the above substitution for $V_G(x)$ lies in the fact that one can treat the matrix $\mathbf{K}_{oc}$ like the matrix $\mathbf{K}$ in Section 3.5, with the solution for the variables $\bar{R}$ and $\bar{S}$ given by

$$\begin{bmatrix}\bar{R}(x)\\ \bar{S}(x)\end{bmatrix} = \Phi_{oc}(x-x_0)\begin{bmatrix}\bar{R}(x-x_0)\\ \bar{S}(x-x_0))\end{bmatrix} \tag{4.25}$$

where $\Phi_{oc}(x-x_0)$ is the transition matrix for the open circuit situation. Therefore, for the second-order system defined by (4.24), the solution can be expressed in terms of

$\Phi_{oc}(x)=\exp[\mathbf{K}_{oc}.x]$, in an analogous way to what was been done in Section 3.5, namely

$$\mathbf{\Phi}_{oc}(x) = e^{K_{oc}x} =$$

$$\begin{bmatrix} \cosh(\lambda_1^{oc}x) - j\dfrac{\beta}{\lambda_1^{oc}}\sinh(\lambda_1^{oc}x) & -j\dfrac{\gamma}{\lambda_1^{oc}}\sinh(\lambda_1^{oc}x) \\ j\dfrac{\gamma^*}{\lambda_1^{oc}}\sinh(\lambda_1^{oc}x) & \cosh(\lambda_1^{oc}x) + j\dfrac{\beta}{\lambda_1^{oc}}\sinh(\lambda_1^{oc}x) \end{bmatrix} \tag{4.26}$$

with $\lambda_1^{oc}=[|\gamma|^2-\beta^2]^{1/2}$, the system eigenvalues being λ_1^{oc} and $-\lambda_1^{oc}$ and

$$\beta = [(k_{11}+\delta) - \frac{|\alpha|^2}{\nabla}]$$

$$\gamma = [k_{12} - \frac{\alpha^2}{\nabla}]$$

and $\nabla=\omega C_s/2$. It is interesting to notice that replacing β by $(k_{11}+\delta)$, γ by k_{12}, and λ_1^{oc} by λ_1, one ends up with the transition matrix for the zero-input system, derived in Section 3.5.

4.11 NUMERICAL AND EXPERIMENTAL RESULTS

In this section numerical and experimental results regarding the interdigital structures modelled in this chapter are presented. As was done in Chapter III for the case of short-circuited gratings, the consistency of the COM and the approximated models is checked against the network model developed in this thesis. Also in the first part of this section, network model calculations are compared with published device measurements for the NSPUDT quartz orientation (Euler angles:[0° 132.75° 25°]). IDT insertion loss, IDT input admittance, directivity, and delay line insertion loss plots are presented. In a second part of this section the network model calculations are compared with measurements on delay lines structures containing two regular IDTs. In this subsection, more traditional orientations, namely quartz ST-X (Euler angles:[0° 132.75° 0°]) and YZ-$LiNbO_3$ (Euler angles:[0° 90° 90°]) are included. In a third and final part of this section, the procedure to find NSPUDT orientations, developed earlier in this Chapter, is illustrated with some numerical results.

4.11.1 Comparison with COM, approximate model, and published experiments

The next paragraphs are devoted to the presentation of some calculated results using the IDT model defined in this thesis. Comparisons are made with: calculations using the COM procedure, calculations using the approximate equations referred to in Section 4.8, and also with published measured data.

Most of the calculations and comparisons in this subsection refer to quartz ST-25 (Euler angles: [0° 132.75° 25°]). The reason for the choice is that this cut was one of the first for which a practical application of the non-symmetrical IDT behaviour was mentioned, namely the high directivity (NSPUDT) phenomenon. The availability of published experimental data for direct comparison with computations was another reason for this choice. However it is worth stressing that the model developed in this thesis applies to arbitrary directions. High directivity orientations are just particular cases.

The values of the IDT parameters used in this subsection are: regular IDT of 500 fingers, as discussed in Section 4.3; finger width of 5 μm and finger-overlap width of 1.6 mm; metallization ratio η=0.5; Al-film thickness of 2000 Å. The device parameter values as well as all experimental data in this section are from [31,32].

As an initial self-consistency test, the frequency responses of the IDT electrical to mechanical insertion loss using the COM description & the Network Model are compared in Fig. 4.8 for both the forward and the reverse propagation directions. For this crystal cut and for this essentially narrowband IDT structure, the COM description calculations match the Network Model calculations to within 2% over a 10 dB bandwidth.

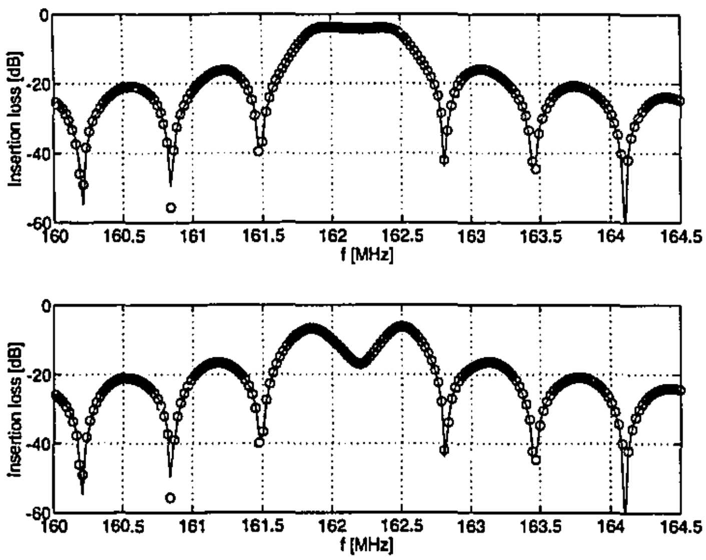

Fig. 4.8 IDT electrical to mechanical insertion loss for both the network model (solid curve) and the COM description (ooo curve); a) forward propagation direction; b) reverse propagation direction.

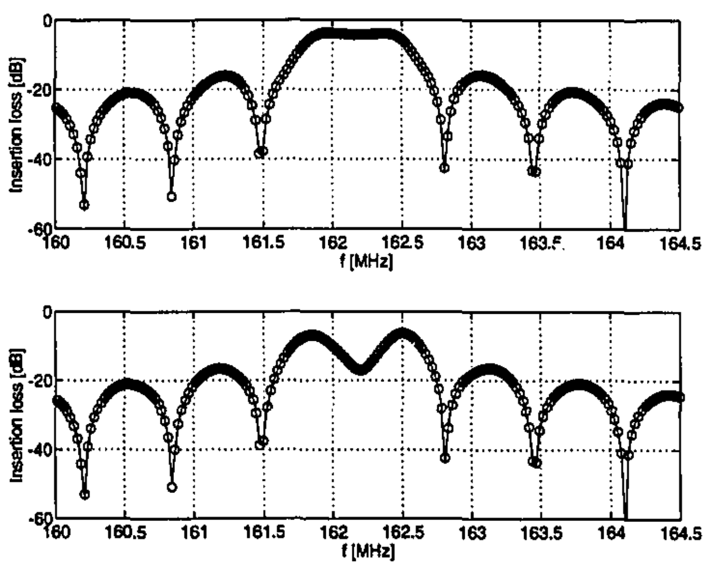

Fig. 4.9 IDT electrical to mechanical insertion loss using full network model (solid curve) and the approximate network model parameters (ooo points); a) forward propagation direction; reverse propagation direction.

Figure 4.9 compare the frequency responses of the IDT electrical to mechanical insertion loss using the extended GWF approximate network model parameters (Section 4.8.1) and the full network model (Section 4.3). For the same narrowband situation plotted in Fig. 4.8, the error obtained in the magnitude using the approximate equations is less than 0.6% over a 10 dB bandwidth [56].

Figure 4.10 is the directivity plot for the same IDT structure. This graph is the difference between the Network Model curves in Figs. 4.8a & 4.8b, and can be calculated using (4.5). The 12.8 dB directivity obtained is in agreement with experimental results, as shown in the figure.

In Fig. 4.11 the calculated input admittance for the same IDT structure is compared with measured results. The solid curve is the calculated result neglecting parasitics, whereas the broken line takes into account a typical parasitic circuit consisting of a 6 nH series inductance followed by a 1 pF capacitance to ground. The calculated curves agree very well with the measured data for both the conductance and the susceptance when taking into account this parasitic circuit.

A delay line structure was also simulated. The first transducer is the one mentioned above. The second is a 20 wavelength split-finger IDT, modelled as discussed in Section 4.4. A 3 μs (free region delay) was used between transducers. Note that since the proposed model takes reflections of the structure into account, the triple transit effect in a delay line is fully predicted, as well as any distortions due to multiple reflections in the structure.

Figure 4.12 shows the excellent agreement obtained between the proposed model and the measured data for the delay line insertion loss for both propagation directions: forward and reverse (positions of split-finger IDT and regular IDT interchanged). The 1.6 dB difference in insertion loss is quite acceptable since several mechanisms, like: mode conversion, radiation losses, propagation losses, diffraction loss, ohmic losses, and other device imperfections (alignment with the crystal axis, shorted or open fingers, etc.) are not considered in the model.

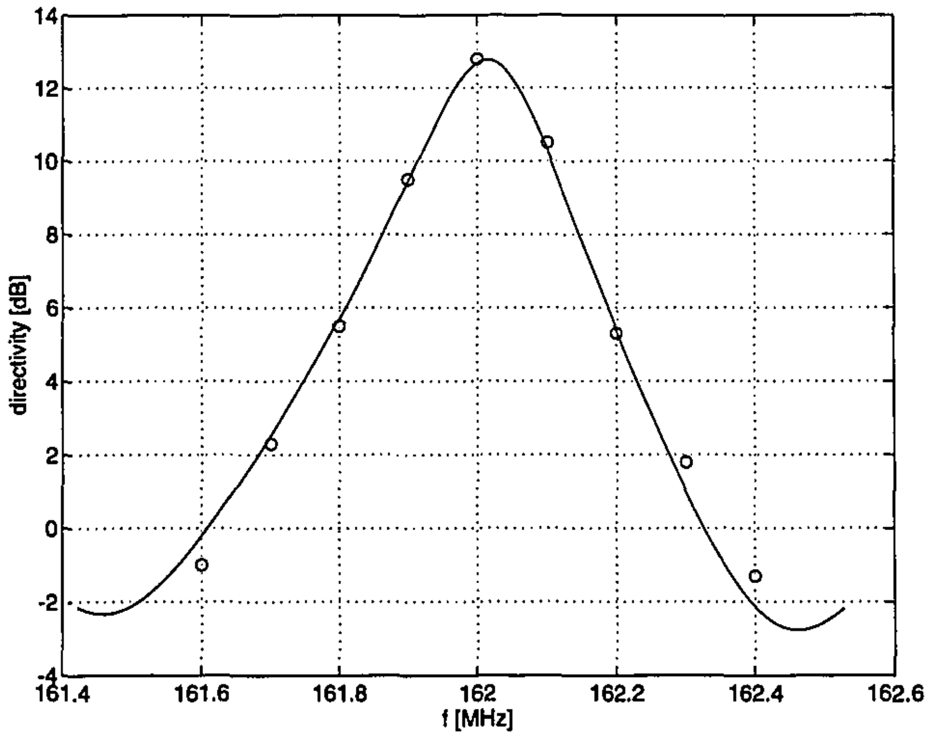

Fig. 4.10 Directivity plot for the IDT structure; network model (solid curve) and experimental results (ooo points).

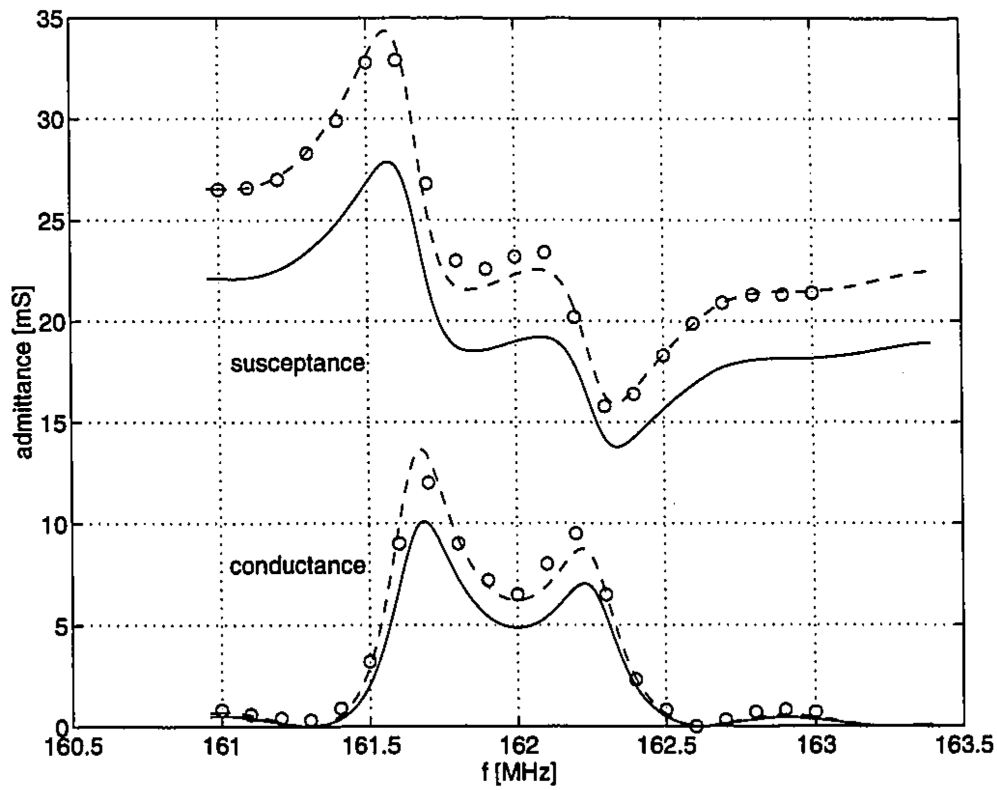

Fig. 4.11 IDT input admittance: network model (solid curves), experimental result (ooo points), network model plus typical parasitic circuit (broken curves).

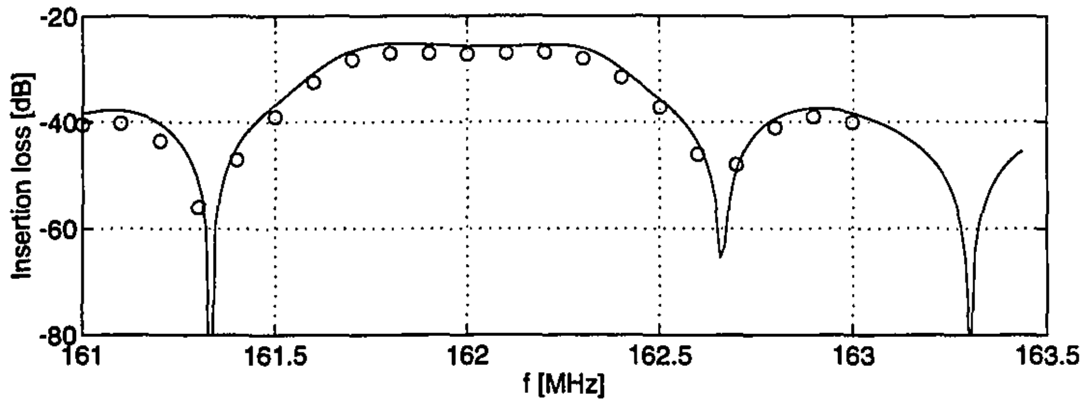

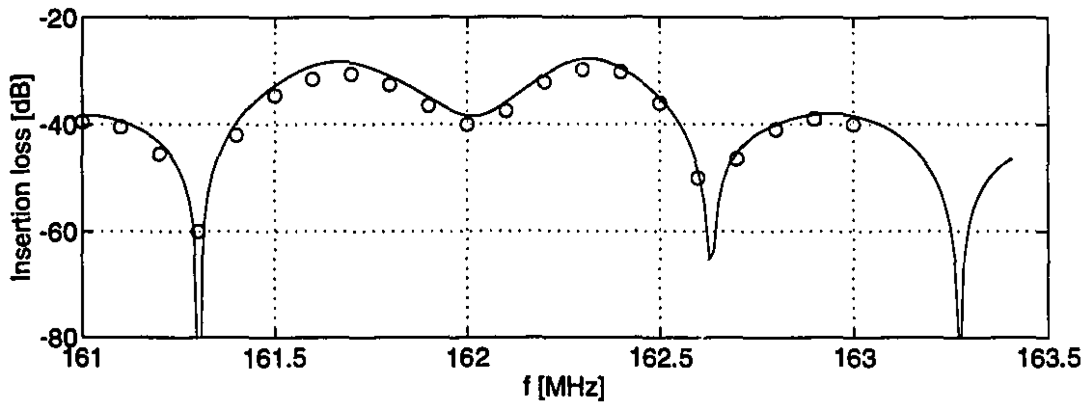

Fig. 4.12 Delay line insertion loss for both propagation directions: a) forward and b) reverse (positions of split-finger IDT interchanged); network model (solid curves) and experimental results (ooo points).

Because the calculated curves in Fig. 4.12 used **only** b_e as a parameter for obtaining a best fit with the experimental data, we are able to estimate that the value of the energy storage susceptance, b_e, for this quartz orientation is $b_e=9.5\pi(h/\lambda)^2$. This is a useful result and yields a value of b_e which is about 20% different from the value for the X-propagating direction [57] for the same h/λ.

4.11.2 Other regular IDT delay lines: comparison with measured data

The objective of this subsection is to compare some additional regular IDT delay line insertion loss measurements with predictions obtained by using the network model developed in this thesis. Some of the following results are oriented along more traditional crystal directions, like quartz ST-X (Euler angles:[0° 132.75° 0°]) and YZ-$LiNbO_3$ (Euler angles:[0° 90° 90°]).

The values of the IDT parameters used for the quartz orientations results in this subsection are: regular IDT (Section 4.3) of 120 fingers; finger width of 16 μm and finger-overlap width of 3.2 mm; metallization ratio η=0.5; Al-film thickness of 1500 Å; and center to center distance between IDTs equal to 8 mm.

From Figs. 4.13 and 4.14 an excellent agreement can be seen between the predicted and the measured delay line insertion loss results for ST-X quartz. The predicted and measured sidelobes are in good agreement at about -26.8 dB. In this case the calculated insertion loss is -31.1 dB and the one obtained experimentally is -31.9 dB, the difference being credited to the same factors mentioned in the previous subsection. In Fig. 4.13 interference due to plate modes [5] not included in the network model analysis can be noted at higher frequencies. In the passband, a frequency perturbation of about 150 KHz, which is due to the effect of multiple reflections in the IDT electrodes, is seen in both the predicted and the measured results.

For the same delay line geometry, Figs. 4.15 and 4.16 verify the good agreement in a delay line insertion loss prediction loss for the NSPUDT orientation quartz ST-25°. The sidelobes prediction and the measured results are in excellent agreement, both -26.5 dB below the main lobe. The predicted and measured insertion losses are -29.5 dB and -32.2 dB, respectively. At this orientation a power flow angle of 5° is calculated, and since that has not been accounted for in the design of the mask, originally projected for quartz ST-X, an additional 1.1 dB insertion loss is expected in this case. As in the case of quartz ST-X, plate modes can be observed at higher frequencies. For both quartz experiments illustrated above, the effect of energy storage is negligible due to the thin layer ($h/\lambda \cong .0023$).

Figs. 4.17 and 4.18 compare the insertion loss predicted by the network model with measured results [69] for the YZ-$LiNbO_3$ orientation. The transducer parameters are: regular IDT of 11 fingers; finger width of 12.3 μm and finger-overlap width of 2.56 mm; metallization ratio η=0.5; Al-film thickness of 1800 Å; and center to center distance between IDTs equal to 12 mm. Again a very good agreement is observed between calculate and measured results. The right sidelobe suffers strong distortion due to the slow-shear bulk mode generated by the IDT in this orientation [16,70].

4.11.3 Some numerical results for NSPUDT search orientations

Another important point addressed in this section refers to the procedure outlined in Section 4.6 for finding high directivity orientations. A straightforward consequence of higher directivities is that one needs less fingers to get the same directivity effect. This might be an advantage in saving substrate in NSPUDT applications, and avoiding additional problems in mask making and construction of the device. Certainly in addition to the high directivity search, other parameters must be observed in finding a practical NSPUDT orientation, such as the piezoelectric coupling coefficient, the reflectivity itself, and the temperature dependence. The objective in this subsection is to illustrate with a few examples the NSPUDT search procedure of Section 4.6.

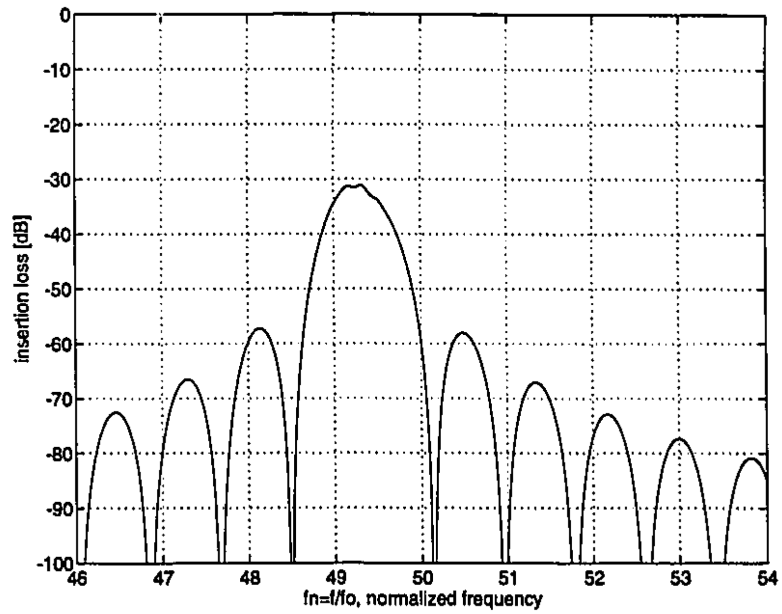

Fig. 4.13 Predicted delay line insertion loss versus frequency (quartz ST-X).

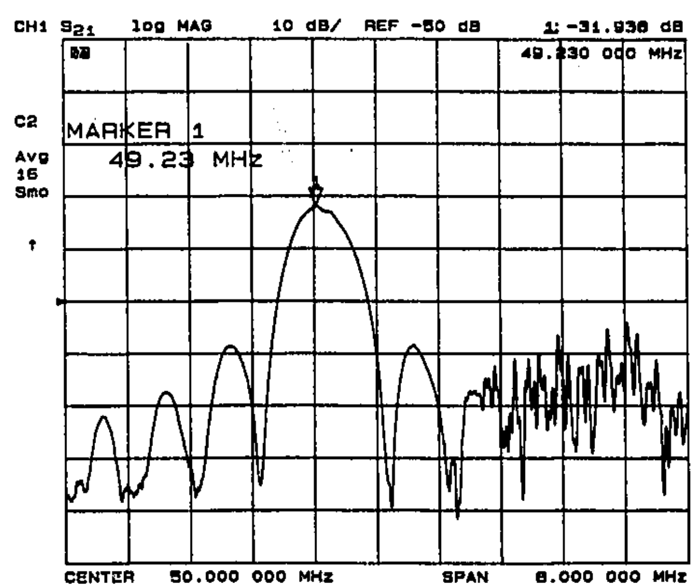

Fig. 4.14 Measured delay line insertion loss versus frequency (quartz ST-X).

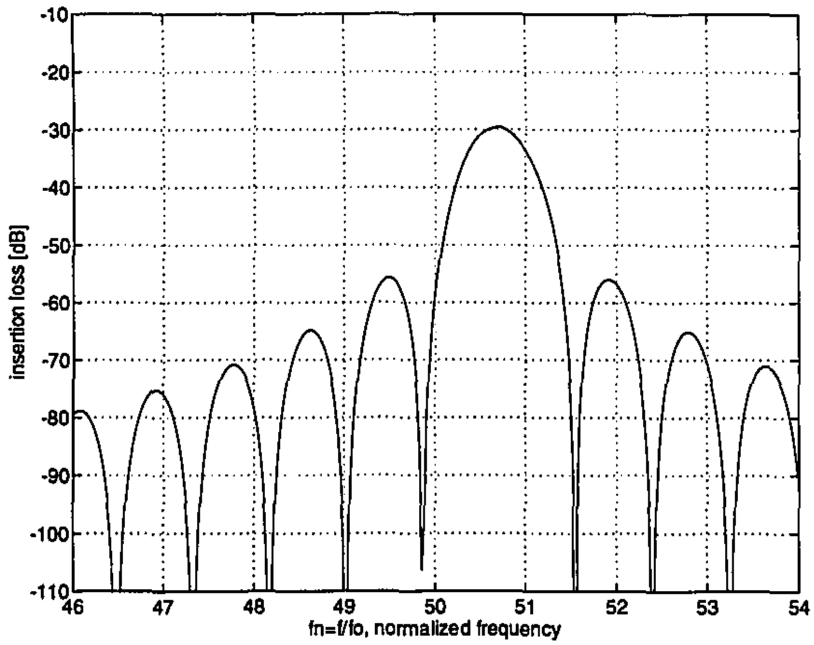

Fig. 4.15 Predicted delay line insertion loss versus frequency (quartz ST-25°).

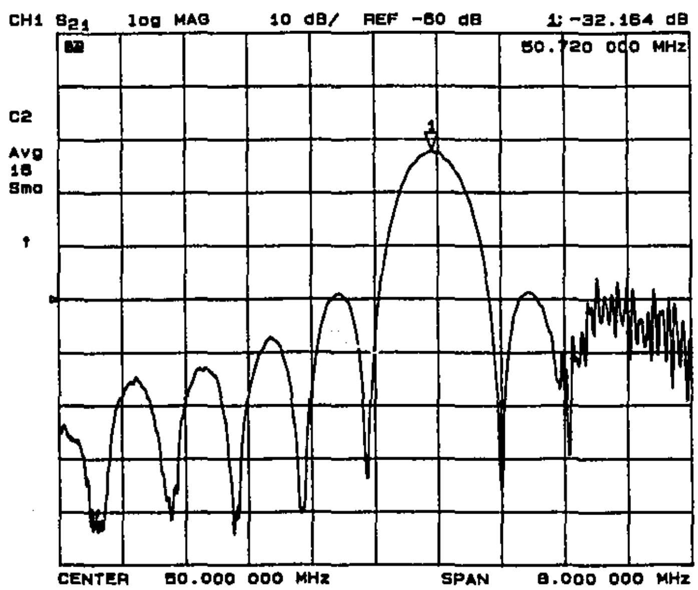

Fig. 4.16 Measured delay line insertion loss versus frequency (quartz ST-25°).

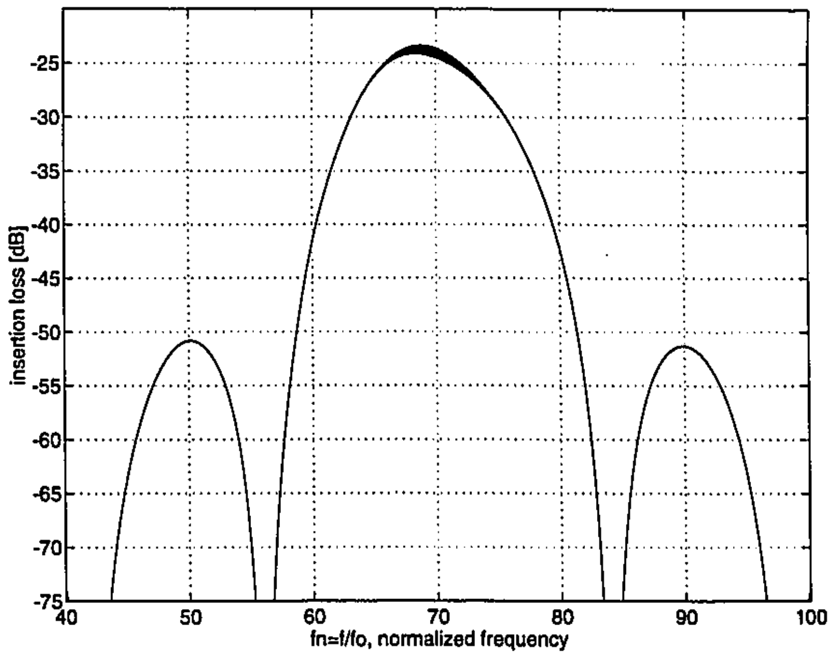

Fig. 4.17 Predicted delay line insertion loss versus frequency (YZ $LiNbO_3$).

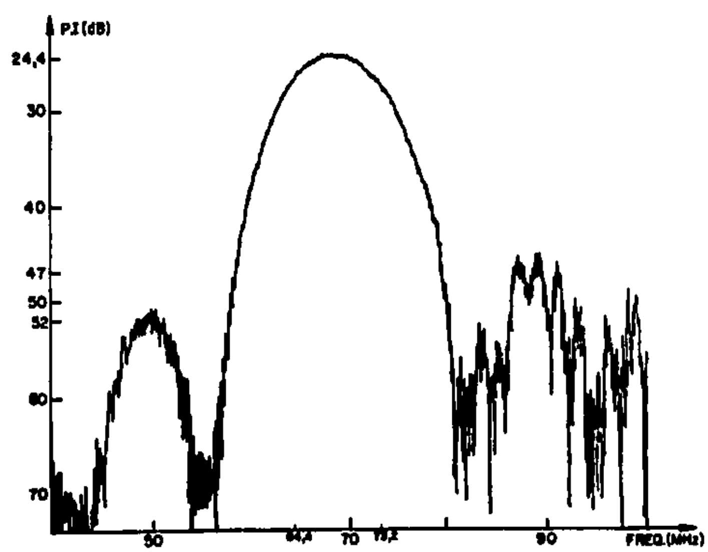

Fig. 4.18 Measured delay line insertion loss versus frequency (YZ $LiNbO_3$).

Working with the conditions imposed by (4.8) and (4.9), enables one to find the highest directivity orientations in ST cut quartz, at (Euler angles: 0° 132.75° ψ), ψ=21°, 159°, 300° and 240°, for h/2p=.01 . For example, at ψ=300°, a directivity of 30.5 dB is obtained. Such a value is much higher than the 12.8 dB for the direction (Euler angles: 0° 132.75° 25°) shown in Fig. 4.10. Although the electromechanical coupling constant for the 300° direction ($K^2=4.5\cdot10^{-4}$, $|\Gamma_u|=3.5\cdot10^{-3}$) is about one third that of the 25° direction ($K^2=1.4\cdot10^{-3}$, $|\Gamma_u|=1.5\cdot10^{-3}$), the much higher directivity obtained deserves attention and may justify the use of this new orientation. Due to the quartz symmetry, the 21° & 159° orientations and the 300° & 240° orientations have the same directivity properties. One should comment, however, that the ψ=60°, 120°, 201° and 339° orientations (the first two are mentioned in [32]) correspond to reverse-NSPUDT directions: the power goes in the opposite directions for these values of ψ. Applying the conditions imposed by (4.8) and (4.9) to lithium tetraborate, one high directivity orientation identified in this material is (Euler angles: 0° 60° 27°), with $K^2=5.5\cdot10^{-3}$, and $|\Gamma_u|=3.2\cdot10^{-3}$ for h/2p=.01, and a directivity of 23.3 dB, illustrating once again the method discussed in Section 4.6.

In this section plots of directivity, input admittance and delay line insertion loss have been presented for transducer structures oriented along a high directivity NSPUDT direction, quartz (Euler angles: 0° 132.75° 25°). Excellent agreement between measured published results and the predictions of the scalar model developed in this work have been demonstrated. The same good agreement has been observed in comparing delay line insertion loss measurements with the network model predictions along more traditional orientations such as ST-X quartz and YZ $LiNbO_3$. The consistency between the network model developed, the COM model and the GWF approximation has been demonstrated through predictions of the IDT electrical to mechanical insertion loss. Finally, the high directivity search procedure developed in this chapter has been applied for two different material cuts, in order to illustrate its use.

4.12 SUMMARY AND CONCLUDING REMARKS

In this chapter a Network Model for arbitrarily oriented IDT structures has been presented. Full expressions have been derived for calculating the transfer matrix for each IDT cell, which are then cascaded for the full IDT computation (Section 4.3). One of the main features of the model devised is that all discontinuities are taken into account at their physical location, thus enabling the precise consideration of reflections in the IDT structure. This powerful tool allows the correct modelling and simulation of arbitrarily oriented IDTs, and hence is essential for both symmetric and asymmetric orientations. Using the basic IDT cell presented in this chapter, apodized and chirped IDTs can also be analyzed, and finger resistance and SAW damping effects can be included.

Computed results for the insertion loss response, input admittance, and directivity response, based on the IDT Network Model, are in excellent agreement with measured data given in the literature and from this thesis work for the high directivity (NSPUDT) orientation on quartz (Euler angles: [0° 132.75° 25°]) (Section 4.11). The same fine agreement between numerical and experimental data is observed for delay line responses positioned along more traditional orientations, like quartz ST-X and YZ-$LiNbO_3$.

A procedure based on physical reasoning for finding high-directivity orientations has been outlined, and some previously unknown directions in quartz and lithium tetraborate have been identified to illustrate its use (Sections 4.6 and 4.11).

The third Coupling-of-Modes (COM) parameter, namely the transduction coefficient, has been derived in this chapter from the Network Model, and an approximate analytical expression for it is also given (Sections 4.7 and 4.8). Together with the COM parameters derived in the previous chapter, the full set is determined. Through numerical evaluation, the consistency between the COM description and the Network Model in predicting an IDT response in arbitrary orientations is verified (Section 4.11). For completeness, the IDT cell is used to determine an open-circuited grating cell, and also the COM description is extended to analyze the open-circuited grating structure (Section 4.10).

The work developed up to this chapter has been concerned with the SAW modes, their effect in practical SAW structures, and the convenient scalar modelling of these modes and structures, when oriented along arbitrary directions. In the next chapter, other propagating modes, namely the pseudo-SAW modes, are discussed for arbitrary directions of propagation .

CHAPTER V

SAW, PSAW AND A NEW HIGH VELOCITY PSAW MODE

5.1 INTRODUCTION

The work developed in the previous chapters focused on the SAW forward and reflected waves, assuming that the generation of other propagating modes could be neglected in calculating SAW reflectivities for the structures involving thin layer discontinuities. In this chapter, two other propagating modes are considered in addition to the SAW waves. The first is the pseudo-SAW (PSAW) mode [25], and the other is a new dominantly longitudinally polarized high-velocity pseudo-SAW mode. This new pseudo-SAW can have very low propagation loss along certain directions, which together with its high velocity make it potentially attractive for high frequency device applications. Some original exploratory work is done concerning the solutions (boundary function behaviour) of these new pseudo-waves and their properties (phase velocity, attenuation, fields) for arbitrary orientations on a free or metallized half-space and their generation at step discontinuities.

In SAW devices fabricated on arbitrary orientations there is always a generalized surface wave mode (GSW) having general particle displacement polarization and along some orientations there may also exist an additional independent quasi-shear polarized pseudo-SAW (PSAW) mode [25]. Brillouin scattering theory and experiments on cubic materials have verified the main properties of the pseudo-SAW modes [84]. Furthermore the existence of a third independent high-velocity pseudo-SAW (HVPSAW) mode has been discussed by some Brillouin scattering researchers. Clearly if the attenuation of this mode is low it would permit an even higher frequency of operation than either SAW or PSAW based devices. Although Brillouin scattering researchers have classified this mode as a highly lossy wave, results obtained and mentioned in this chapter indicate that this is not always the case. To the best of the author's knowledge this work is original; the existence of such high-velocity pseudo surface wave modes on different materials has not been discussed in the SAW device literature[2]. In this chapter, numerical and experimental results are presented which describe the existence and properties of these high-velocity pseudo-surface-waves for piezoelectric materials oriented along arbitrary directions.

In addition, the mode matching method introduced in Chapter II is extended to include the generation of these pseudo-SAW modes in the scattering calculation.

In Section 5.2 the pseudo-SAW solutions are reviewed briefly, and the nature of both PSAW and HVPSAW modes discussed. Section 5.3 presents numerical and experimental pseudo-SAW results for different materials and orientations. The boundary function is plotted as a function of phase velocity and attenuation, the pseudo-SAW solutions in the ST plane on quartz, and for a layered condition are presented, and experimental measurements on quartz ST-X and quartz ST-25 discussed. In Section 5.4 these pseudo-SAW modes are included in the mode matching technique described in Chapter II. Finally, Section 5.5 presents some concluding remarks to this Chapter.

5.2 PSEUDO-SAW SOLUTIONS

The well-known mechanically free pseudo-SAW solutions have a propagation loss due to the power carried away from the surface by the accompanying "growing tilted bulk-like partial wave" needed to satisfy the stress-free surface boundary conditions [25,86]. In the case of the high-velocity pseudo-SAW mode there are two "tilted bulk-like partial waves" (for symmetry type 1 in [9]) which carry power away from the free surface [84], and which are necessary to satisfy the stress-free boundary conditions. As in the

[2] Since the work discussed in this chapter was completed, the existence of a quasi-longitudinal SAW has been independently confirmed for lithium tetraborate (Euler angles: [45° -θ° 90°]) in a translation of a Russian crystallography journal article [85].

PSAW problem, the numerical solution to the HVPSAW problem requires finding a zero of a complex function of two real variables, namely the phase velocity, v_p , and the attenuation constant, α, thus necessitating a multivariable search procedure for minimizing the boundary condition function. Finding such a minimum in the complex plane is often much more difficult in the HVPSAW problems, than it is in the PSAW situation, since it turns out that the target functions are usually steeper and multi-valleyed, as is illustrated in the next section. The phase velocity for the HVPSAW lies close to that of the longitudinal bulk wave and the polarization is dominantly longitudinal, a fact which may have led this wave to be identified as a bulk acoustic wave [87]. At a sufficient depth below the surface two of the four coupled partial waves are essentially tilted bulk modes radiating into the solid.

In the next section, some numerical and experimental results are presented for pseudo-SAW modes for some representative materials and orientations. The next section also addresses the effective permittivity function concept, ε_{eff} , the Poynting vector and "power flow angles" for the PSAW and HVPSAW.

5.3 NUMERICAL AND EXPERIMENTAL DISCUSSION

In this section some numerical and experimental data obtained regarding the HVPSAW and the PSAW solutions, including the metallic layered case are discussed. It is not the intention to classify and exhaustively discuss different materials and orientations. Reference is made to a few selected materials, and the quartz ST plane has been chosen for most of the numerical and experimental examples, with particular attention to the orientation (Euler angles: [0° 132.75° 25°]), or quartz ST-25° alluded to several times throughout this thesis.

To illustrate the problems in finding a zero of a complex function of two real variables, namely the phase velocity and the attenuation constant, Fig. 5.1 shows a mapping of the boundary function value as a function of v_p and α for a free surface PSAW problem, and Fig. 5.2 shows a similar plot for a HVPSAW metallic layered problem (h/λ_{SAW}=1%), both on quartz (Euler angles: [0° 132.75° 25°]). These figures represent a typical functional behaviour observed for other materials and orientations. Several valleys, which are relatively close to each other, can be seen in these pictures and thus the minimization routine can easily settle at a local instead of a global minimum. A few of these minima are quite smooth, and some represent the situation where the problem degenerates, presenting identical eingenvalues. In order to avoid local minima, it is convenient to use numerical routines which allow bounding the search range in the phase velocity and the attenuation plane (v_p , α plane). For routines which do not allow bounding the search range, the solution is very sensitive to initial values selected. For comparison, Fig 5.3 shows the equivalent boundary function for the single variable case of the free surface SAW solution for the same material and orientation. In Fig. 5.4, the boundary function is shown for a layered problem (aluminum), where here the phase velocity has been fixed at 3.2 Km/s, a value slightly smaller than the free surface solution, and a plot is done with respect to the independent real parameter *thickness x frequency* (hf). The minima seen in Fig. 5.4 correspond to solutions for the modes of a layered substrate, namely, the first generalized surface wave, the first generalized Love mode, etc., with increasing thickness. Compared to the multivariable plots shown in Figs. 5.1 and 5.2, one can see that in both cases of Figs. 5.3 and 5.4 the boundary functions are relatively smooth close to the solution(s).

The fact that the boundary functions for the HVPSAW problems have typically steeper behaviour close to the solution than in the PSAW problems, thus increasing the difficulty involved in finding the HVPSAW solution when compared to the PSAW solution, is illustrated qualitatively in Figs. 5.5 (PSAW) and 5.6 (HVPSAW). This two figures are zooms of Figs. 5.1 (PSAW) and 5.2 (HVPSAW) around the respective PSAW and HVPSAW solutions.

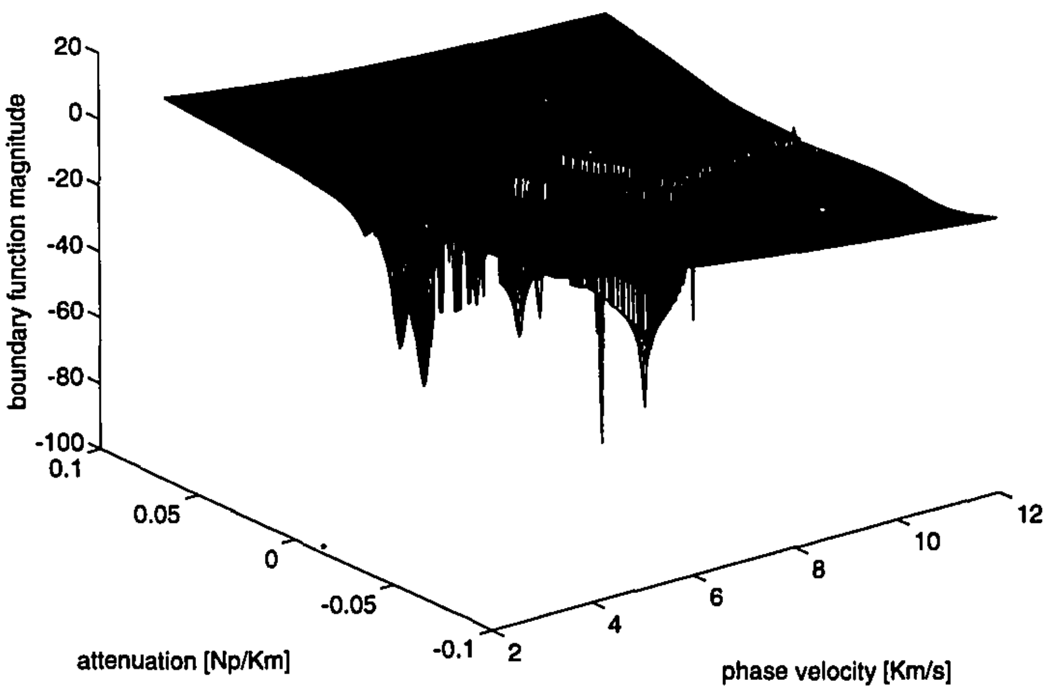

Fig. 5.1 Boundary function value as a function of the phase velocity, v_p, and attenuation, α, for the pseudo-SAW (PSAW) (free surface quartz, Euler angles:[0° 132.75° 25°]).

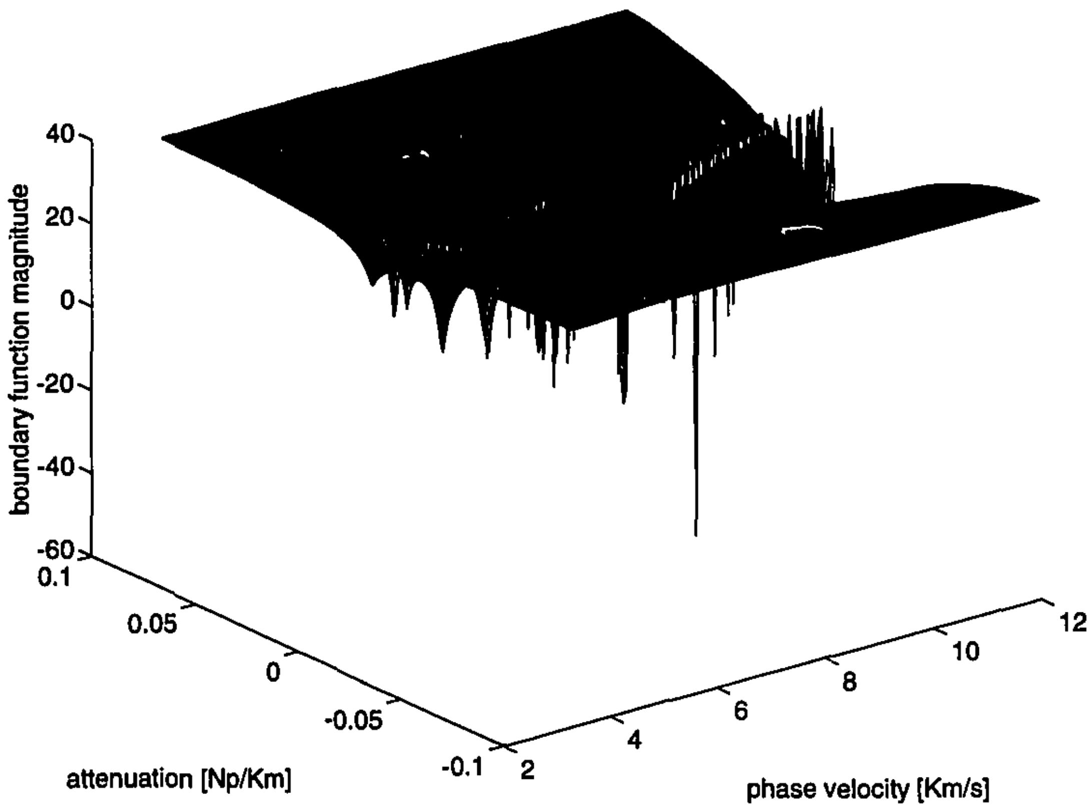

Fig. 5.2 Boundary function value as a function of the phase velocity, v_p, and attenuation, α, for the high velocity pseudo-SAW (HVPSAW) (aluminium layer on quartz, Euler angles:[0° 132.75° 25°]).

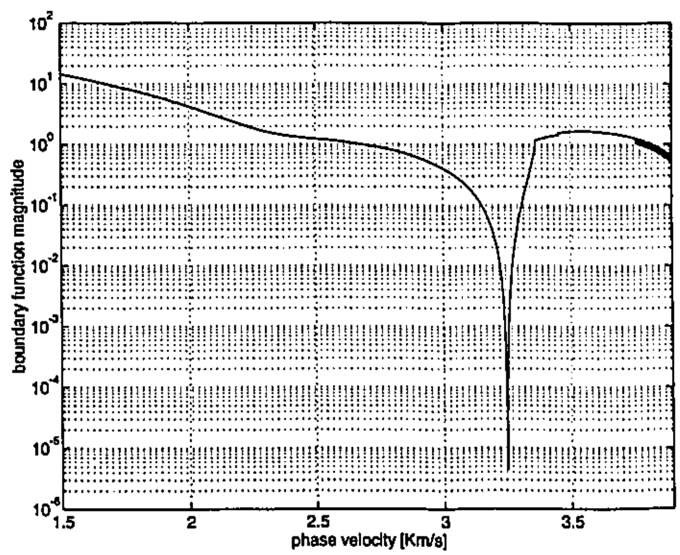

Fig. 5.3 Boundary function value as a function of the phase velocity, v_p, for the regular SAW (free surface, quartz, Euler angles:[0° 132.75° 25°]).

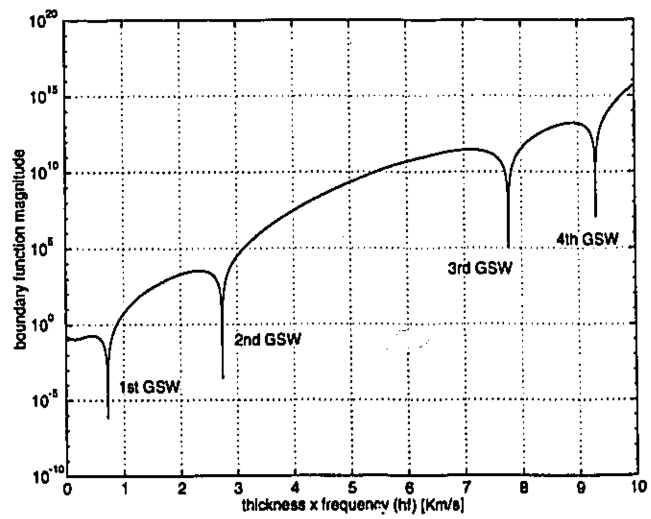

Fig. 5.4 Boundary function showing the several generalized surface wave (GSW) modes as a function of thickness x frequency (hf) for a fixed phase velocity, v_p=3.2 km/s; aluminium layer on quartz, Euler angles:[0° 132.75° 25°].

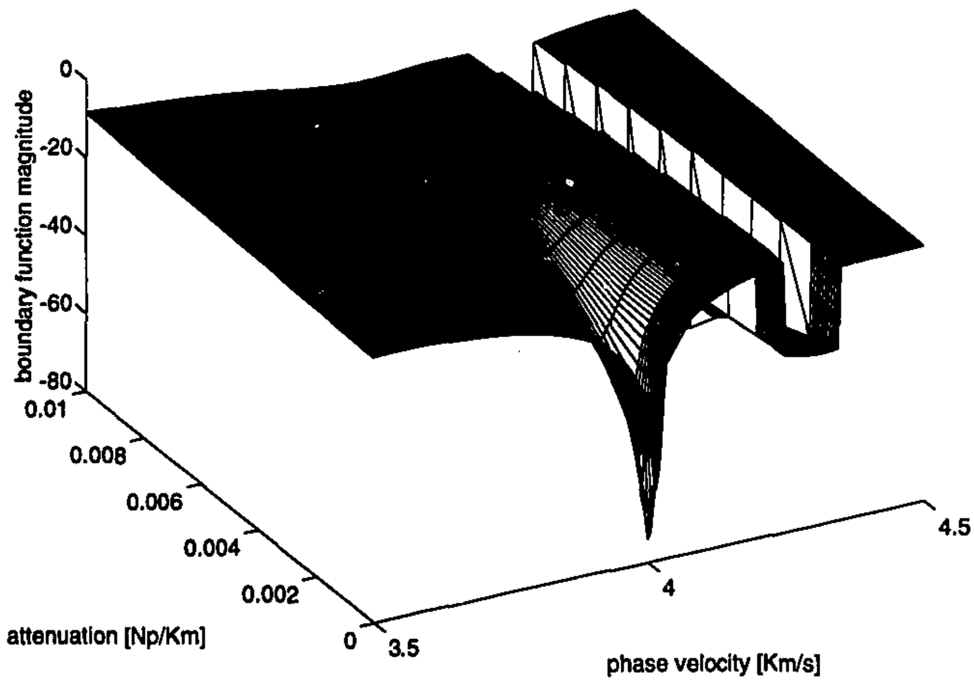

Fig. 5.5 Detail near the solution region for the boundary function value as a function of the phase velocity, v_p, and attenuation, α, for the pseudo-SAW (PSAW) (free surface quartz, Euler angles:[0° 132.75° 25°]).

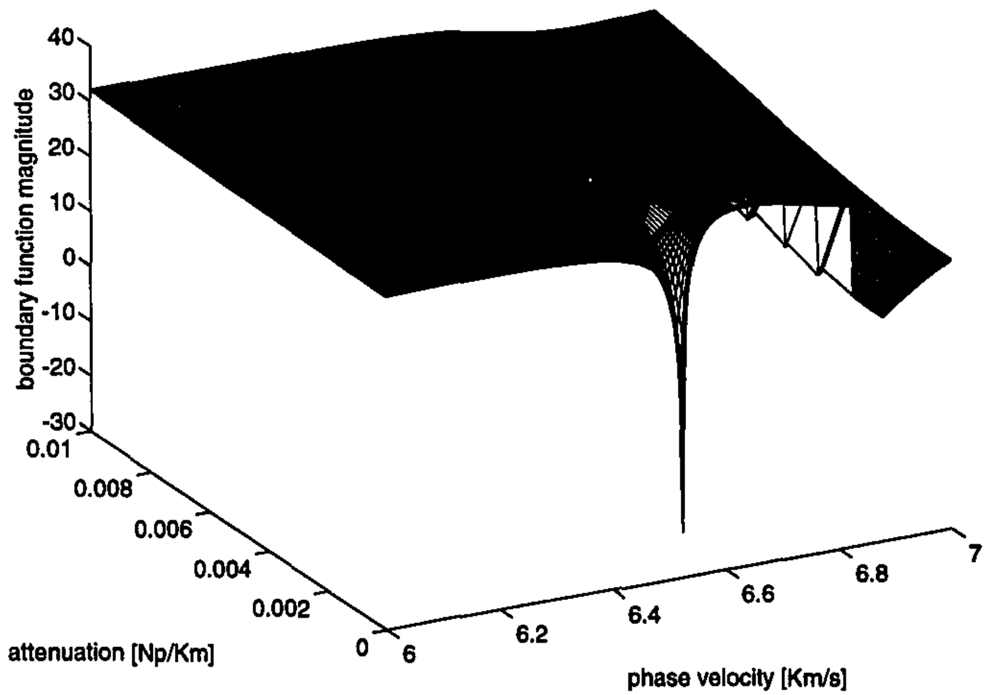

Fig. 5.6 Detail around the solution for the boundary function value as a function of the phase velocity, v_p, and attenuation, α, for the high velocity pseudo-SAW (HVPSAW) (aluminium layer on quartz, Euler angles:[0° 132.75° 25°]).

The effective permittivity, or surface permittivity, is a scalar function which relates the normal electric displacement discontinuity to the surface potential, and is defined as $\varepsilon_{eff}(\omega/v_p)=\{D_3^+-D_3^-\}/(\omega\phi(0)/v_p)$ [16,70,88,89]. As stressed by Milsom, "... for a given substrate it effectively stores all the relevant mechanical information in a scalar electrical quantity." Since ε_{eff} relates the surface potential to the charge density, it is an attractive way of formulating surface acoustic wave excitation problems [16,70] on piezoelectric materials: the potential is specified at electrode locations, and $\{D_3^+-D_3^-\}=0$ on unmetallized regions. The boundary information described by ε_{eff} and expressed in the (ω/v_p) domain is translated to the space or x-domain by use of the Green's function [16,70] which is the inverse Fourier transform of $\bar{G}(\omega/v_p)=[\omega\varepsilon_{eff}/v_p]^{-1}$, and interpreted as the surface potential produced by a line charge at $x=x_1$. Therefore from the Green's function, derived from ε_{eff}, and the calculation of the charge distribution in a transducer, the wave potential is determined [16,70]. This method has been used successfully by numerous research groups to solve surface acoustic wave excitation problems [79,90,91,92,93]. On dealing with PSAW excitation on 36° YX $LiTaO_3$ [90,92,91] the Green's function derived from ε_{eff} is complicated by the interaction between the PSAW and the resulting bulk mode, which is also seen from the complex propagation constant for the pseudo-SAW. If the influence of mode coupling is neglected, a poor theoretical prediction for the IDT input admittance [91] is achieved. Simplifications for ε_{eff} based either on the expansion of the Green's function in several more tractable numerical functions [16,90], or in approximate expressions [92], have been used. The boundary conditions, expressed in terms of ε_{eff} [86], has a plot similar to the one of Fig. 5.1, in the PSAW case, where both v_p and α must be accounted for. The consideration of ε_{eff} as a function of a complex constant of propagation in the Green's method for determining PSAW or HVPSAW excitation, although more complex, may lead to a better understanding of the interactions between modes in the acoustic transducer structures and thus deserves further attention. In Fig. 5.7 ε_{eff} is plotted as a function of the real phase velocity, v_p, thus neglecting the attenuation α for the same material and orientation as in Figs. 5.1. Other than allowing the determination of the SAW free and metallized solutions [16,70], this plot permits, in many cases the identification of the PSAW phase velocity solution vicinity.

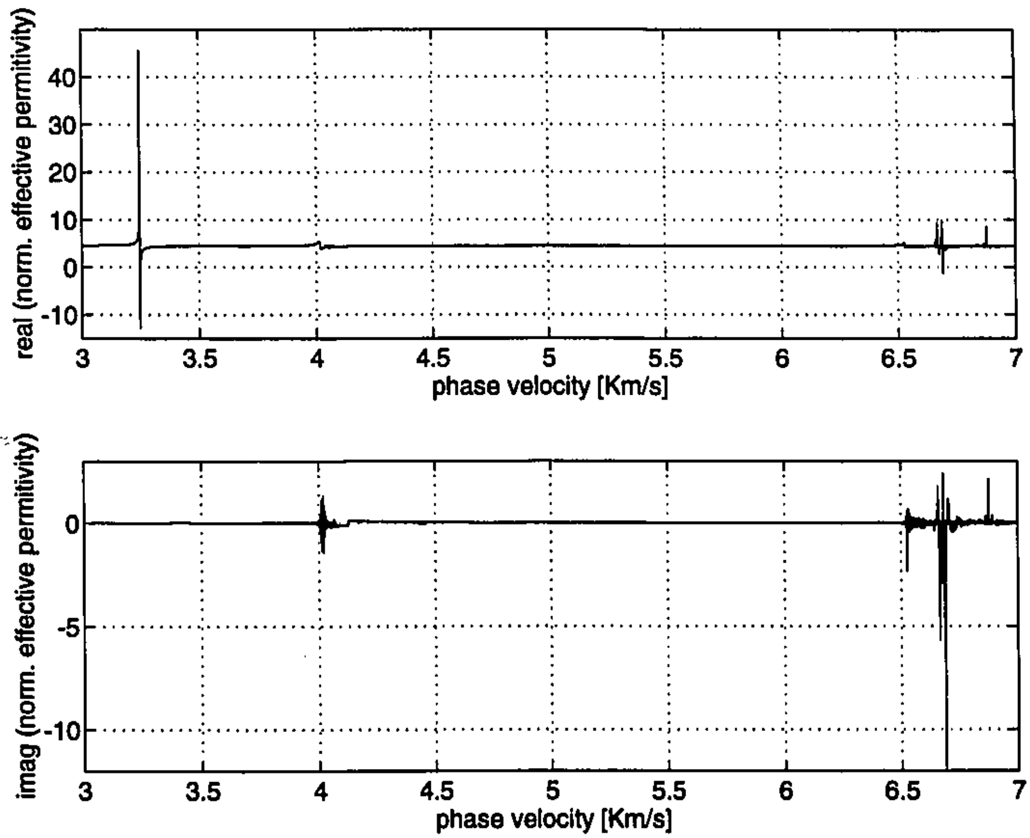

Fig. 5.7 Plot of the normalized effective permittivity function, $\varepsilon_{eff}/\varepsilon_0$, versus the phase velocity, v_p, (quartz, Euler angles:[0° 132.75° 25°]).

In Tables 5.1 and 5.2 solutions for the PSAW and the HVPSAW, respectively, are presented for some selected materials and orientations. As can be noted from these tables, the polarization for the PSAW has a large shear horizontal component, whereas the HVPSAW has a predominant longitudinal component. For quart ST-25° and GaAs (Euler angles: [45° 54.74° 20°]) free surface solutions are missing in Table 5.2, since no success has been obtained in finding them using the multivariable search procedure for minimizing the boundary condition, mentioned in the previous section. If these free surface HVPSAW exist along these orientations, the reason for not finding them certainly lies on degree of difficulty encountered in locating the global minimum, as mentioned previously (see Fig. 5.2, for instance). It is worth noting that for the orientations presented in Table 5.2, the attenuation of the HVPSAW wave is smaller than 0.01 dB/λ; for the $Li_2B_4O_7$ orientation chosen as an example, one can see a $2|\Delta v_p|/v_p$= 1.34 % (with Δv_p the free to metallized phase velocities difference), on the top of a small attenuations (0.011 and .0003 dB/λ for short/open surfaces), indicating the suitability of this orientation for high-frequency low-loss devices applications.

Fig. 5.8 shows plots of phase velocity and attenuation versus propagation angle ψ from the X-axis for the HVPSAW on a mechanically free short-circuited surface on the **ST cut quartz plane** [Euler angles: 0° 132.75° ψ]. Notice that the mode exists over the entire plane and that the attenuation of the wave decreases significantly near ψ=29°. Certainly, directions where the attenuation is significantly small are attractive for practical devices, especially in the case of the high velocity pseudo-SAWs, which would allow the fabrication of high-frequency devices with reduced losses.

Fig. 5.9 depicts the situation for an aluminum layered quartz substrate for propagation at ψ=25° . The top part of this figure shows the phase velocities for the first and the second generalized Rayleigh modes, together with the phase velocities of the PSAW and the HVPSAW modes, as a function of the layer thickness-frequency product (hf). As the layer thickness is reduced, the PSAW phase velocity approaches from below that of the bulk fast shear, whereas the HVPSAW velocity approaches that of the bulk longitudinal. The lower part of this figure shows plots of the attenuation for both pseudo-modes versus hf. It is interesting to notice from these curves that as hf increases the PSAW mode dispersion curve appears to merge continuously with the (lossless) second generalized Rayleigh mode, which has a cut off at hf close to 1.5. At this thickness the PSAW mode has a negligible loss which rapidly increases for lower thicknesses, exhibiting a minimum of 0.007 dB per wavelength at about hf=.35 ($h/\lambda \approx 8.9\%$). For the orientation and thickness range considered here, the attenuation of the layered HVPSAW mode has a different behaviour from that of the PSAW mode, in the sense that the attenuation decreases monotonically as hf goes to zero. The polarization of the PSAW mode for this orientation is predominantly shear horizontal, whereas that of the HVPSAW mode is essentially longitudinal.

Figs. 5.10 is a measured delay line insertion loss plot on quartz ST-X (Euler angles: [0° 132.75° 0°]) over a wide bandwidth. Both IDTs consist of 60 finger pairs, with metallization ratio equal to a half, η=0.5, finger width of 16 μm, aperture W of 3,2 mm; and their center to center distance is 8 mm. The SAW response is at about 49.3 MHz. The other two responses, at 79.3 MHz and 89.8 MHz, show excellent agreement with the predicted PSAW and HVPSAW solutions. These measurements could be claimed to be irrefutable practical evidence of the pseudo-modes. Unfortunately these solutions have values of phase velocities which are very close to the shear and longitudinal bulk waves velocities, respectively. One could then argue that these measured responses are bulk waves generated by the IDT which travel close to the surface, but not at the surface since the bulk modes do not satisfy the surface boundary conditions. That was the interpretation given to these modes in measurements equivalent to the ones of Fig. 5.10 in [94] for the ST-X quartz and in [87] for the AT-X quartz (Euler angles: [0° -54.7° 0°]). The three spectral components shown in a delay line frequency response measurement on quartz AT-X [Fig. 1 from ref. [87]], are numerically identified in this work with the first GSW, the PSAW (Table 5.1), and the HVPSAW (Table 5.2).

TABLE 5.1

Pseudo-SAW (PSAW) solution for some selected materials and orientations

Material and orientation (Euler angles, [degrees])	v_p [Km/s] short/open	α [dB/λ] short/open	Fields @ z=0 u1,u2,u3 short/open (magnitude [Km])	$2\lvert\Delta v_p\rvert/v_p$ [%]
quartz AT-X [0° -54.7° 0°]	5.0994 5.0996	1.8e-3 1.3e-3	1 6.70 0.33 1 6.66 0.31	0.008
quartz ST-X [0° 132.75° 0°]	5.0781 5.0789	7.9e-2 7.8e-2	1 2.40 0.37 1 2.39 0.36	0.033
quartz ST-25° [0° 132.75° 25°]	4.0166 4.0181	7.8e-2 8.1e-2	1 2.34 0.60 1 2.32 0.59	0.078
36°YX-$LiTaO_3$ [0° -54° 0°]	4.1091 4.2267	2.7e-4 2.1e-4	1 15.2 1.85 1 26.7 0.47	5.6
GaAs [45° -90° 25°]	3.3742 3.3744	2.8 2.8	1 3.328 2.01 1 3.330 2.01	0.025
GaAs [45° 54.74° 20°]	3.0643 3.0646	2.6e-1 2.6e-1	1 1.96 1.317 1 1.96 1.319	0.025

TABLE 5.2

High velocity pseudo-SAW (HVPSAW) solution for some selected materials and orientations

Material and orientation (Euler angles, [degrees])	v_p [Km/s] short/open	α [dB/λ] short/open	Fields @ z=0 u1,u2,u3 short/open (magnitude [Km])	$2\|\Delta v_p\|/v_p$ [%]
$Li_2B_4O_7$* [0° 45° 90°]	7.0267 7.0740	1.1e-2 2.9e-4	1 0 0.061 1 0 0.037	1.34
quartz AT-X [0° -54.7° 0°]	5.7447 5.7454	1.0e-2 2.5e-3	1 0.12 0.077 1 0.12 0.080	0.023
quartz ST-X [0° 132.75° 0°]	5.7446 5.7449	6.0e-3 1.2e-3	1 0.066 0.081 1 0.056 0.084	0.011
quartz ST-25° [0° 132.75° 25°]	6.5262 -	1.8e-5 -	1 0.35 0.090 -	-
YZ $LiNbO_3$ [0° 90° 90°]	7.1754 7.2840	1.5 0.07	1 0 0.032 1 0 0.031	2.98
GaAs [45° -90° 25°]	5.3987 5.3986	1.9e-2 1.6e-3	1 0.04 0.234 1 0.04 0.233	0.004
GaAs [45° 54.74° 20°]	5.2448 -	5.4e-3 -	1 0.08 0.219 -	-

* This particular $Li_2B_4O_7$ orientation has been added to this table as an extra verification of experimental phase velocity data obtained by T. Shiosaki (personal communication, June 1994), and for calculation of the attenuation constant α.

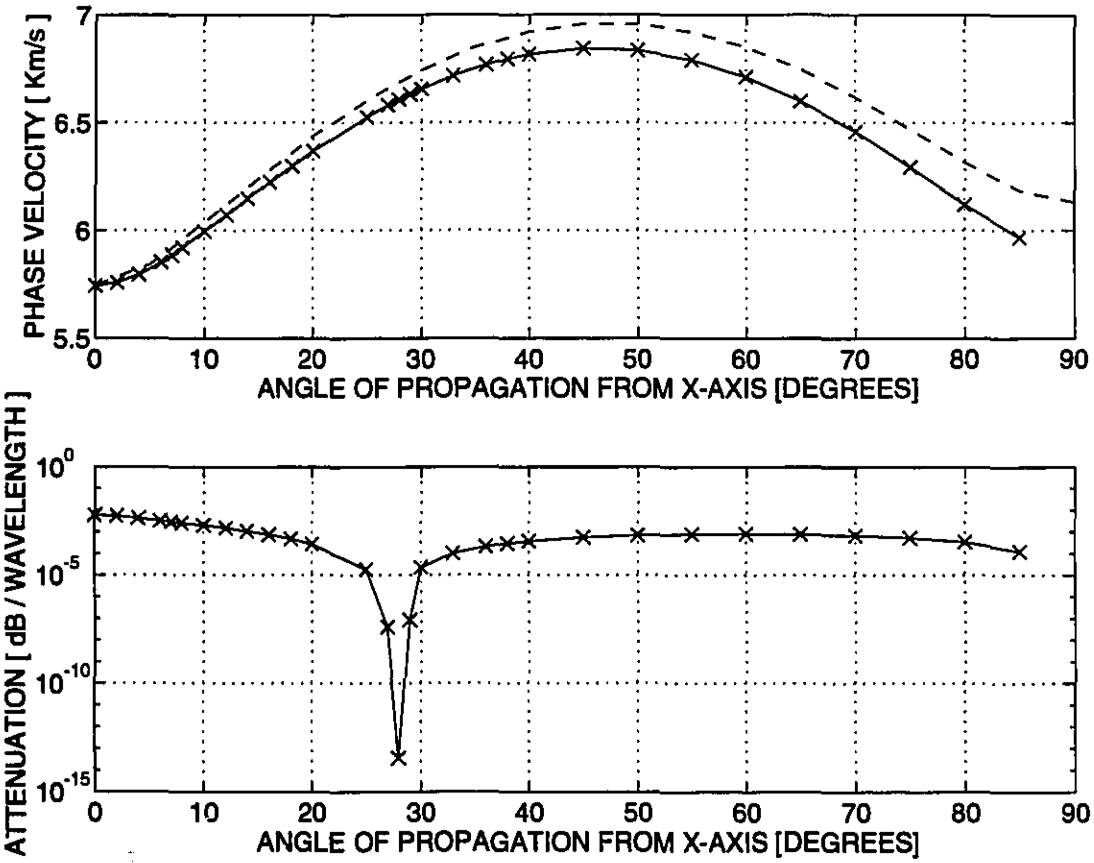

Fig. 5.8 Phase velocity and attenuation for the HVPSAW mode versus the angle of propagation ψ for short-circuited ST cut quartz plane (Euler angles: [0° 132.75° ψ]) (solid and x curves); longitudinal BAW (dashed curve).

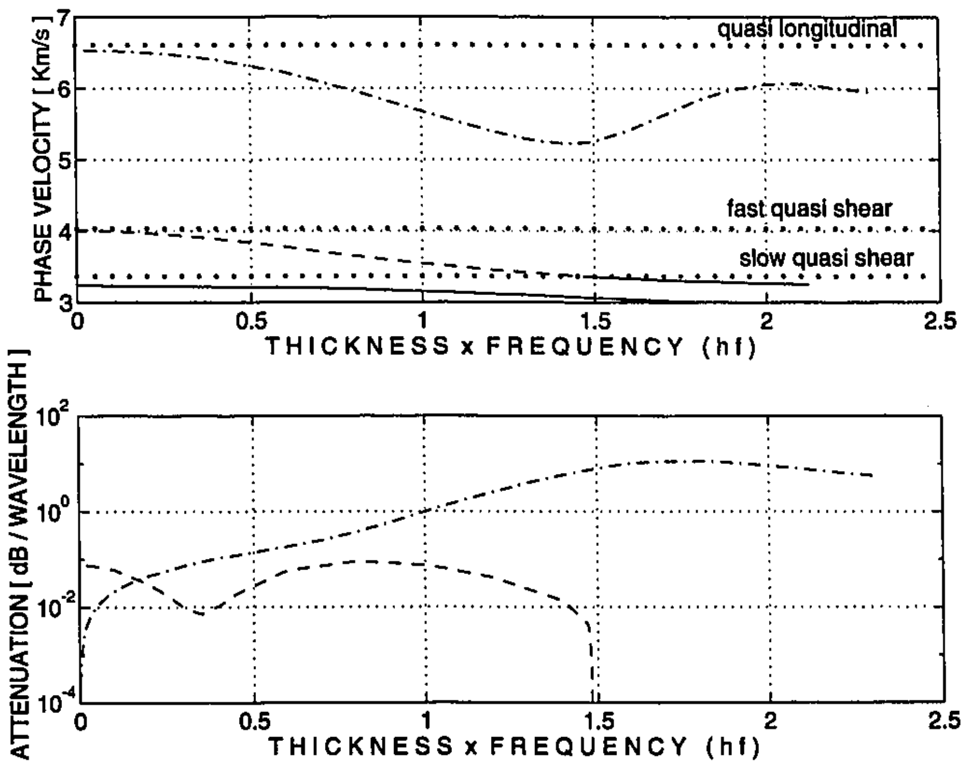

Fig. 5.9 Phase velocity and attenuation versus (thickness x frequency) for an aluminum layered quartz substrate with propagation at (Euler angles: [0° 132.75° 25°]); solid: first and second generalized SAW modes; dashed: PSAW mode; dash-dot: HVPSAW mode; larger-dots: bulk acoustic wave (BAW) velocities for this orientation.

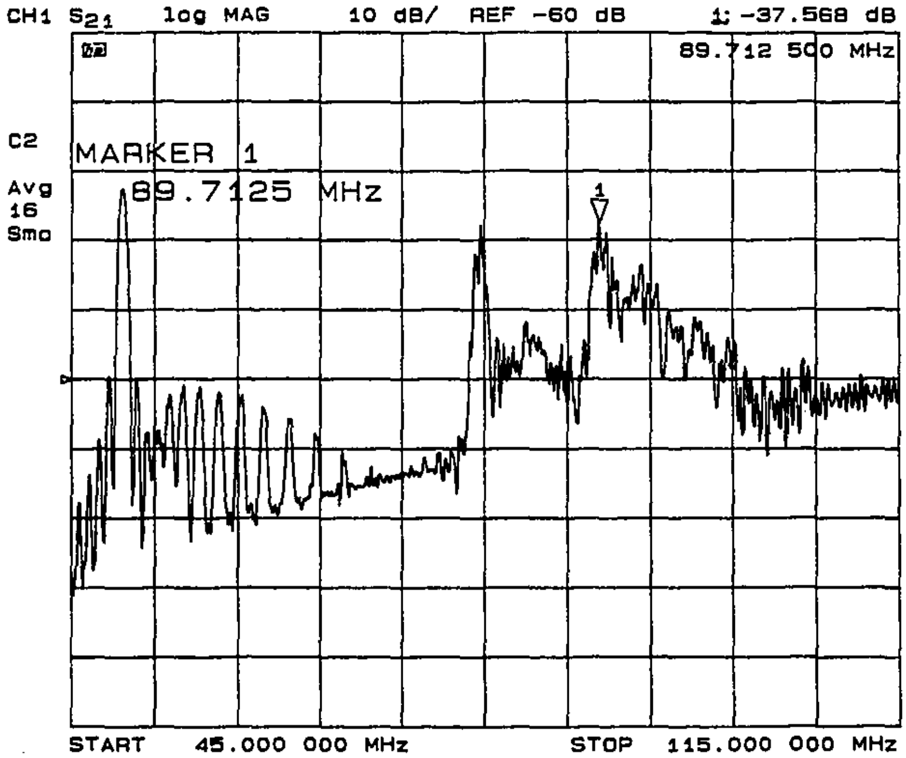

Fig. 5.10 Measured insertion loss frequency response plot for a quartz ST-X delay line (dimensions of the structure described in the text).

In addition to the results on quartz described above, the experimental results on GaAs given in [84] have been numerically confirmed. For the $1\bar{1}1$ plane (metallized surface), for instance at [Euler angles: 45° 54.736° 20°], a phase velocity of 3.065 Km/s and attenuation of 0.26 dB/λ for the PSAW, and a phase velocity of 5.245 Km/s and attenuation of 0.0054 dB/λ for the HVPSAW are obtained.

Some interesting experimental evidence has also been obtained for quartz ST-25° with respect to the calculated and estimated power flow angle. The power-flow angle for the first generalized surface wave (GSW) is calculated unambiguously and is at 5° with respect to the direction of propagation. Regarding the pseudo-modes, the power flow angle concept must be treated with a certain care due to the bulk radiating term(s). For practical purposes, on experiments carried out with substrates of finite thicknesses, the power flow angle can be evaluated approximately by integrating the Poynting vector over a strip of unit width and some finite depth [25]. From previous analyses of how the Poynting vector in the direction of propagation behaves with depth (Fig. 5.11) for this orientation, one can argue that a depth of 14 wavelengths for the PSAW is a reasonable choice, giving a power-flow angle of -29° with respect to the propagation direction. Applying the same procedure for the HVPSAW mode (Fig. 5.12) gives a power flow angle of 14°.

Measurements on a simple delay line fabricated along this orientation, produced experimental evidence of the first GSW and of the HVPSAW. Fig. 5.13 shows a delay line insertion loss plot on quartz ST-25° over a large bandwidth. In addition to the main GSW peak, a HVPSAW response can be identified. One should note that in this delay line no provisions were made for compensating for the beam steering mentioned in the previous paragraph, since the fabrication mask was the same as that used in the ST-X quartz experiment mentioned before (Fig. 5.10). As depicted in Fig. 5.14a, the PSAW mode was detected by means of an additional interdigital transducer positioned parallel to the one excited, but at a sufficiently large offset angle (-23°), that it intercepted some of the PSAW power going at the -29° power-flow angle mentioned above. In Fig. 5.14b, the delay line insertion loss plot over a large bandwidth for the structure depicted in Fig. 5.14a on quartz ST-25° is shown. Some power due to the GSW reflected from the border of the wafer could also be detected by this transducer and is seen in this figure.

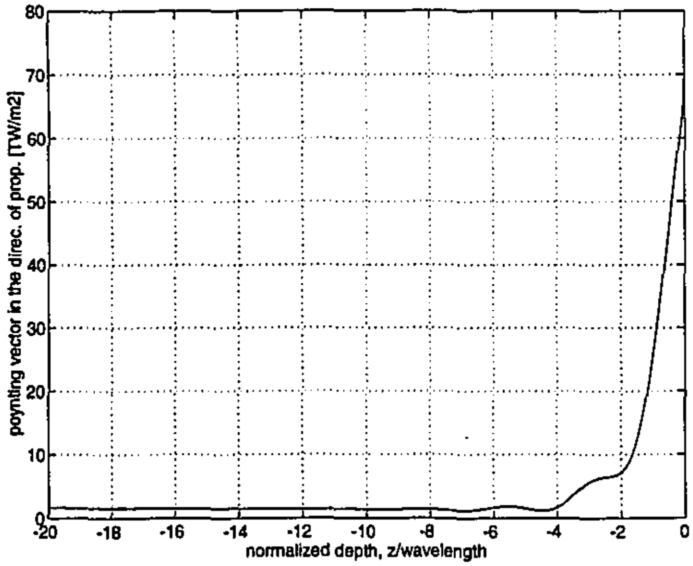

Fig. 5.11 Poynting vector ([TW/m^2]) in the direction of propagation versus the normalized depth inside the substrate for the pseudo-SAW (PSAW) (free surface, quartz, Euler angles: [0° 132.75° 25°], fields normalized with respect to $|u_1|=1$).

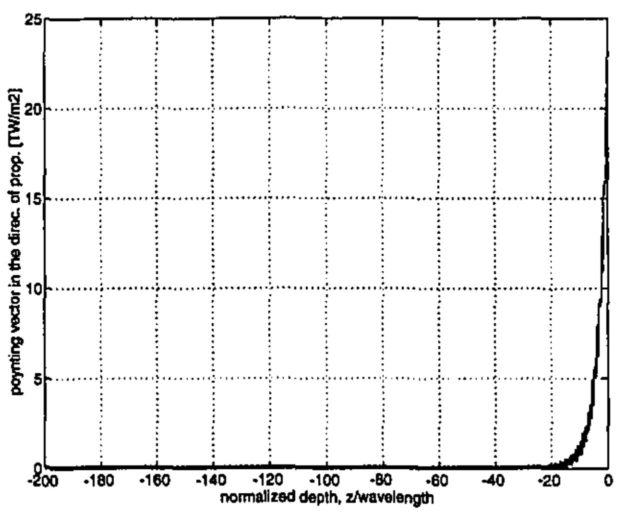

Fig. 5.12 Poynting vector ([TW/m^2]) in the direction of propagation versus the normalized depth inside the st rate for the high velocity pseudo-SAW (HVPSAW) (aluminum layered surface, $h/\lambda_{SAW}=1\%$, quartz, Euler angles: [0° 132.75° 25°], fields normalized with respect to $|u_1|=1$).

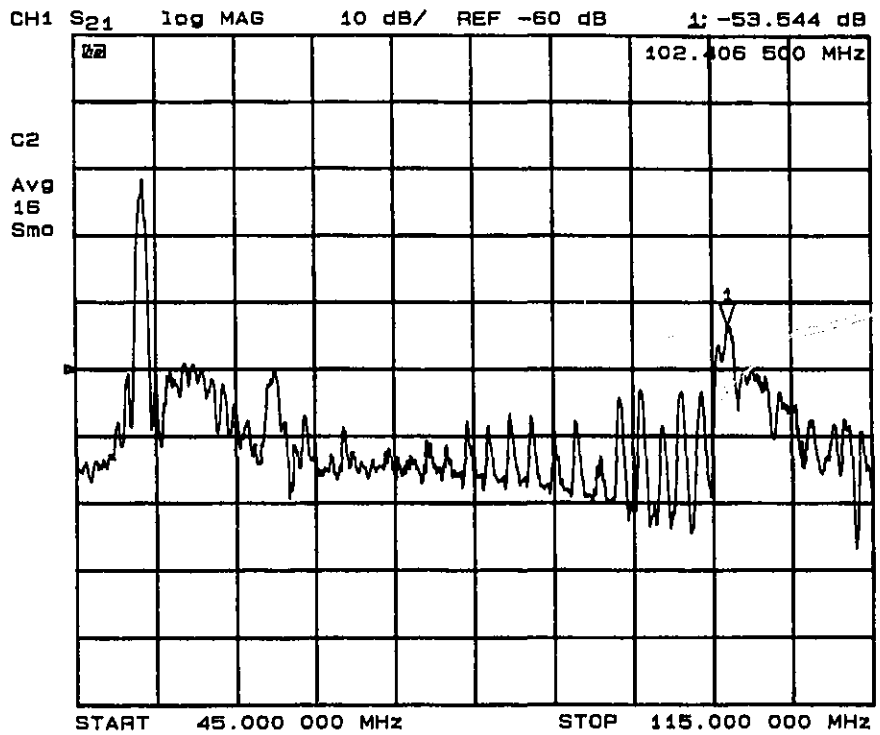

Fig. 5.13 Measured insertion loss frequency response plot for quartz, Euler angles:[0° 132.75° 25°], delay line (dimensions of the structure described in the text).

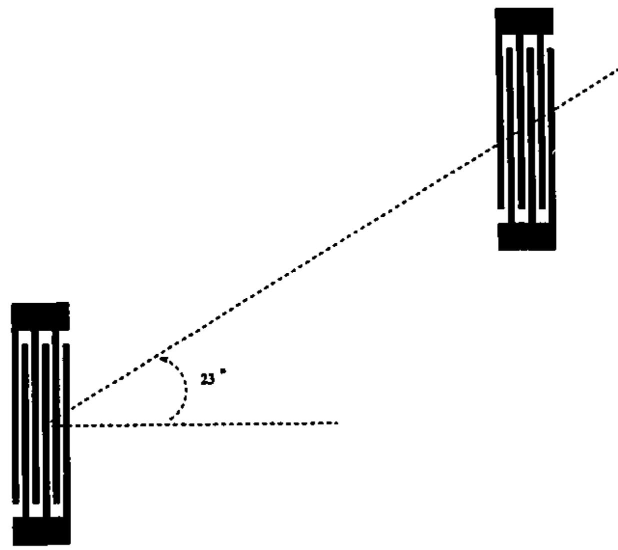

(a)

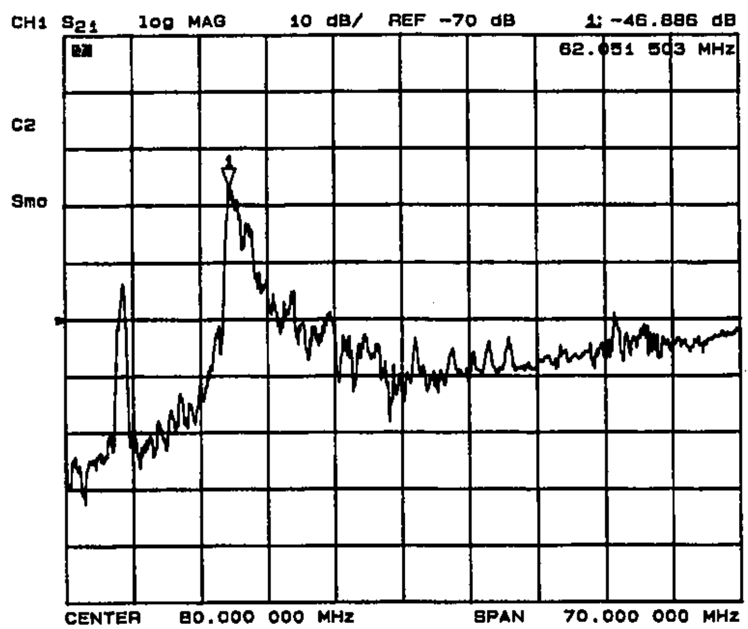

(b)

Fig. 5.14 a) Receiving IDT at an offset angle with respect to the direction of propagation; b) Measured insertion loss frequency response plot on quartz, Euler angles:[0° 132.75° 25°], for the structures positioned as in a).

Figs. 5.15 and 5.16 show the declination of the Poynting vector, or its tilt down into the solid, as a function of depth in the case of two layered (h/λ_{SAW}=1%) surface HVPSAW solutions, namely $Li_2B_4O_7$ (Euler angles: [0° 45° 90°]) and quartz ST-25, in a similar analysis as the one done in [25] for the PSAW modes. In the $Li_2B_4O_7$ situation there is only one growing tilted bulk-like partial wave due to the symmetry in this direction of propagation (symmetry type 3 in the classification of [9]). For this orientation the azimuth angle between the Poynting vector and the propagation direction (x direction) is zero. Close to the surface the Poynting vector is basically parallel to the surface, and at about seven wavelengths below the surface this bulk term tilted at 46° is the only one left. For the quartz ST-25° situation considered in Fig. 5.16, one can see that a more complex behaviour of the Poynting vector with depth takes place due to the existence of two tilted bulk-like partial waves, which are the terms left after about 50 wavelengths. A similar behaviour is found for the azimuth angle, which varies in this case between 10° and -30° after 50 wavelengths.

5.4 MMM2

In Chapter II, Section 2.8, the mode matching technique was introduced and used to calculate mode scattering coefficients; the only modes considered were the lossless generalized Rayleigh waves.

In this section, a generalization of this procedure is described to account for other modes, namely the pseudo-SAW modes described in this chapter. The underlying procedure is as in Chapter II: the waveguide fields at the discontinuity between two guides are written as a superposition of the available modes over the region which is common to both waveguides. Now a SAW incident from the left in Fig. 2.2 is scattered not only into a reflected and a transmitted SAW, but also into reflected and transmitted pseudo-SAW modes. Therefore the continuity statements represented by (2.22) are augmented to include on the left and on the right side of the equations the pseudo-SAW modes which may exist along the desired direction of propagation.

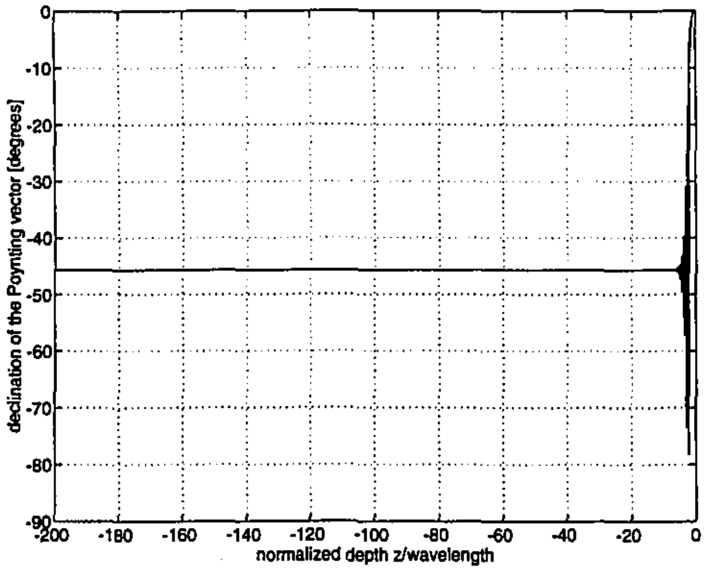

Fig. 5.15 Declination of the Poynting vector as a function of normalized depth for the high velocity pseudo-SAW (HVPSAW); aluminum layered surface, h/λ_{SAW}=1%, $Li_2B_4O_7$, Euler angles:[0° 45° 90°], fields normalized with respect to $| u_1 |$=1.

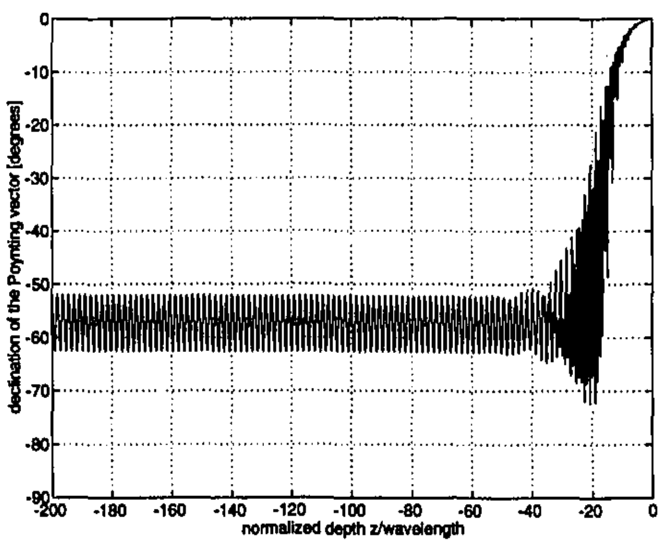

Fig. 5.16 Declination of the Poynting vector as function of normalized depth for the high velocity pseudo-SAW (HVPSAW); aluminum layered surface, h/λ_{SAW}=1%, quartz, Euler angles:[0° 132.75° 25°], fields normalized with respect to $| u_1 |$=1.

The scalar product defined by (2.23) is used without ambiguity, but the τ_p and τ_v vectors now receive new indices to accommodate for the new modes, so that for a SAW wave incident from the left, one ends up with: τ_p^{LFS}, τ_p^{LBS}, τ_p^{LBP}, τ_p^{LBH}, τ_p^{RBS}, τ_p^{RBP}, τ_p^{RBH}; where the superscripts indicate: LFS (left forward SAW), LBS (left backward SAW), LBP (left backward PSAW), LBH (left backward HVPSAW), and RFS (right forward SAW), RFP (right forward PSAW), RFH (right forward HVPSAW). The same set of fields apply for τ_v.

It is worth mentioning that the method applies just as well for an incident PSAW or HVPSAW from the left, τ_p^{LFP} (and τ_v^{LFP}) or τ_p^{LFH} (and τ_p^{LFH}), respectively, which is then scattered into the forward and backward PSAW, SAW and HVPSAW. In order to obtain approximate scattering coefficients in the case of the pseudo-SAWs, their fields are normalized to power as mentioned in the previous section, considering a finite depth, after which the only term left is the "tilted bulk wave", the same depth used in the scalar product of (2.23). This method, as seen from this discussion, clearly allows for coupling between the several modes.

The inner products formed in the case of an incident SAW from the left are still given by (2.24). In calculating the inner products of (2.24), in particular the integration from $-\infty$ to zero, one has to verify if the SAW partial wave which has the less attenuated decay is still larger than the growing tilted mode(s) from the PSAW or HVPSAW. Otherwise a finite depth as mentioned in the previous paragraph should be selected. Now, instead of having the two unknown scalar coefficients of Chapter II, six scalars are involved if all pseudo waves are present in that direction of propagation.

Other four equations are easily added to (2.24) if the inner products are formed with the PSAW fields: τ_v^{RFP}, τ_p^{LFP}, τ_p^{RFP}, τ_v^{LFP}. And similarly other four if the HVPSAW fields are used instead.

The same different constraints on the scattering parameters used in Chapter II were tested in the process of the minimization of (2.24). The step condition assumed, as in Chapter II, considers the fields of the infinitely free surface on the left of the discontinuity and the fields of the infinitely layered surface on the right of the discontinuity plane (Fig. 2.2). Still not considering the δ-function effect present in the RRM method, the reflection coefficient of the minimum found is essentially the same as that of the minimum found without the PSAW modes obtained in Chapter II. Coupling coefficients to other modes are obtained, which satisfy the power inequality constraint $|S_{11}|^2+|S_{21}|^2+|S_{31}|^2+|S_{41}|^2+|S_{51}|^2+|S_{61}|^2-1\leq 0$. The nonzero values of the coefficients confirms that mode coupling exists at the discontinuity.

5.5 SUMMARY AND CONCLUDING REMARKS

In this chapter in addition to the SAW, other propagating modes, namely the pseudo-SAW modes are analyzed. In addition to the pseudo-SAW (PSAW) mode from [25], a high velocity pseudo-SAW mode solution is presented, which along some orientations seem to present low loss. The fact that this quasi-longitudinal mode has a high velocity of propagation together with low loss along certain directions, indeed offers potential applications for higher-frequency low-loss devices.

A procedure for finding these solutions has been discussed and the degree of difficulty in finding solutions illustrated by showing the behaviour of the boundary function to be minimized in the complex plane. The ST-quartz plane has been studied as an example, and directions where the loss is significantly lower with respect to others in the plane have been found. Along the quartz orientation (Euler angles: [0° 132.75° 25°]), the metallic layered PSAW mode presented two interesting features: i.) a range of values for the layer thickness where lower losses with respect to other thicknesses are observed, indicating the potential importance that this parameter may achieve in devices that use PSAW; ii.) second, the PSAW solution seems to merge continuously with the lossless generalized second Rayleigh mode.

Experimental evidences of the these pseudo-SAW modes have been shown and discussed. An approximate power flow angle calculation for the HVPSAW mode following the procedure for the PSAW mentioned in [25] has been carried out in the case of the HVPSAW, and the result of such calculation seems to agree well with experimentally observed data.

These two propagating pseudo-SAW modes have been included in the mode-matching technique developed in Chapter II, in an exploratory attempt to allow this method to describe mode-coupling.

CHAPTER VI

SUMMARY AND CONCLUSIONS

This thesis has been concerned with the propagation of surface acoustic waves (SAWs) and pseudo-SAWs, the analysis of reflectivity from thin metallic layers, and the modelling of SAW structures along arbitrary orientations.

The **main original contributions** of this thesis are:

1. A new shunt susceptance network element has been introduced in a scalar transmission line model to account for the bilateral asymmetry which exists along asymmetric directions. Using this shunt susceptance, a new scalar model is developed for both grating and transducer cells. These cells are then cascaded to successfully represent short-circuited gratings, open-circuited gratings, and IDTs oriented along arbitrary directions (including high directivity orientations).

2. A new high-velocity dominantly longitudinally polarized pseudo-SAW mode has been described and its properties illustrated for a few selected materials. Numerical and experimental results presented in this thesis indicate that this mode, not previously referenced in the SAW device literature, is a potential candidate for high-frequency low-loss devices.

3. A theoretical non-perturbation reciprocity relation analysis has been developed to calculate the SAW reflectivity on arbitrary directions due to the presence of thin metallic films. Based on this analysis, the directions of propagation for the SAWs have been studied classified as symmetric or asymmetric, the latter including high directivity orientations. Necessary conditions for asymmetry are established for the first time, namely anisotropy and absence of mirror symmetry of the sagittal plane bulk-wave slowness curves with respect to the direction of propagation. It has been found that when the surface is a symmetry plane, or when the propagation axis is a two-fold axis, no directivity determined by material properties occurs. A perturbation expression for reflectivity is also derived, the generalized Tiersten Boundary Conditions for anisotropic

layers are given, and limits on the validity of the approximate perturbation expression with respect to the layer thickness established by comparison with the more complete reciprocity relation analysis.

4. A "differential-from-discrete" algebraic method is used to demonstrate that the coupling-of-modes (COM) approximate model for gratings and transducers is derivable from the new scalar network model. Approximate network model parameters are derived, and, from these, approximate explicit analytical expressions for the COM parameters are obtained, which predict the COM approximate model for gratings and transducers dependency on frequency, on material parameters, and on geometry.

5. A procedure is given for identifying high directivity (NSPUDT) orientations, based on physical arguments. The derived intuitive approach takes into consideration the geometry, layer material and SAW properties, and leads to the formulation of strategies for finding high directivity orientations.

6. An alternative method using mode matching is introduced to study reflectivity from thin metallic layer discontinuities. Considering only SAW modes or with the inclusion of other propagating pseudo-modes (mode coupling), this method consistently led to results obtained with the reciprocity relation method when the δ-function contribution to the reflection coefficient is neglected.

A summary of the thesis on a chapter by chapter basis follows:

In Chapter I a comprehensive general review of the background literature to the subject of this thesis is included, together with the objectives and motivations for the thesis.

In Chapter II, a procedure for calculating reflectivity of a thin metal strip, based on the reciprocity relation method, is developed, and from this procedure a perturbation equation for reflectivity is derived. A mode matching method for calculating reflectivity is introduced and its results are compared with the results of the reciprocity relation method and the results of the perturbation approximation. Based on this reflectivity study, directions of propagation are classified into symmetric and asymmetric types, the second including the so-called high directivity or NSPUDT orientations. Along asymmetric orientations the reflectivity is not bilaterally symmetric for forward and backward propagating surface waves. To account for this bilateral asymmetry, a new reactive network element is introduced in a scalar transmission line model.

In Chapters III and IV the new network model developed which accounts for bilateral asymmetry is first used to describe grating structures, and then it is extended to describe transducer structures. A procedure is outlined for finding high directivity orientations in a chosen plane. Computed results based on the transducer network model are in excellent agreement with measured data on devices which exhibit directivity due to asymmetric orientations, and also on devices oriented along symmetric directions. A method is devised to derive the coefficients of the coupling-of-modes (COM) model from the new network model parameters. The consistency between the network model and the COM approach is verified. Using approximate network model parameters, explicit analytical expressions for the COM parameters are given.

In Chapter V, pseudo-surface acoustic waves are re-examined. A new high-velocity pseudo-mode (HVPSAW) is presented. Numerical and experimental data are given which describe the existence and discuss the properties of this new mode, indicating that the HVPSAW is a potential candidate for high-velocity low-loss surface acoustic wave devices.

From the results obtained in this thesis, some topics of research which deserve further consideration are:

Extension of the reciprocity relation method to calculate the reflectivity from grooves, represented by a hollow channel in the substrate surface. Grooves are used in resonators, and with respect to orientations where directivity exists, they may be used to reverse the directivity effect in one of the transducer [34]. The precise control of such phenomenon may lead to a new class of low-loss devices.

Study other strip structures and devices oriented along arbitrary orientations, such as the multistrip couplers; track changers; chirped, apodized, and withdrawal-weighted IDTs. The basic cell concept developed in this thesis can be extended to describe these new structures, together with the consideration of second order effects like: resistivity, damping, diffraction.

Inclusion in the mode matching method introduced in this thesis a means of considering the "δ-function effect" accounted for in the reciprocity relation method. Also an investigation of the existence and description of evanescent modes at a step discontinuity deserves further consideration, since it would permit the calculation of the energy storage network element, B_e.

The search for new materials and orientations for: i.) high directivity or NSPUDT directions using the method devised in this thesis which considers the effects of technological parameters like: variations in the layer thickness, h; variations in the metallization ratio, η; variation in the layer characteristics. In addition to analyzing technological parameters, the search must also aim at orientations with high reflectivity and high piezoelectric coupling. ii.) high velocity pseudo-SAWs, with the additional objective of understanding how this mode interacts with the SAW and the pseudo-SAW, and how these waves are excited by the transducer. A possible way to carry out this study might be the extension of the Green's function method to deal with a complex propagation constant.

APPENDIX I

In this appendix the major statements in the matrix method formalism applied to SAW propagation problems [96] are summarized for reference purposes. One of the key advantages of the method is that it reduces the electroacustic equations to a set of first-order vector-matrix ordinary differential equations of at most size 8 (6 for non-piezoelectrics) in the variables that must be continuous across interfaces. In the layered case, one such matrix exists for each layer, and the interfacial boundary conditions are automatically satisfied by a matrix multiplication that preserves the eight (or six) dimensionality of the problem.

The coordinate system is shown in Fig. I.1. Although the method can handle any number of layers, for simplicity only one layer is shown in this figure. The z axis is normal to the layer interfaces. The assumed solution form, for sinusoidal travelling waves along x at a radian frequency ω radians per second, is

$$f(z)\ \exp[j(\omega t-k_1 x)] = f(z)\ \exp\left[j\omega\left(t-\frac{x}{v_p}\right)\right] \qquad (I.1)$$

with v_p and $k_1=\omega/v_p$ representing the phase velocity and propagation constant along x respectively. The vector of normal stresses, $\mathbf{T_z}$, and the particle velocity vector, **v**, are respectively represented by

$$\boldsymbol{T_z} = \begin{bmatrix} T_{13} \\ T_{23} \\ T_{33} \end{bmatrix} \qquad (I.2)$$

$$\boldsymbol{v} = \begin{bmatrix} v_1 \\ v_2 \\ v_3 \end{bmatrix} \qquad (I.3)$$

These are the six mechanical variables, which must be continuous across interfaces. For piezoelectrics the time derivative of the electric potential ($j\omega\phi$) and the normal electric displacement, D_3, are chosen as the two electric variables which must be continuous.

These 6 or 8 variables are a sufficient independent set and all other variables can be expressed in terms of them, using the set of dynamic and constitutive equations of a material.

For problems unbounded normal to the z plane with the propagation direction along x in the xy plane, the problem is two-dimensional, there are no variations in the y direction, hence d/dy=0 and $d/dx=-j\omega/v_p$. The vector τ is defined as the six-component vector for non-piezoelectric materials

$$\boldsymbol{\tau} = \begin{bmatrix} \boldsymbol{T_z} \\ \boldsymbol{v} \end{bmatrix} = \begin{bmatrix} \boldsymbol{\tau_n} \\ \boldsymbol{\tau_v} \end{bmatrix} \tag{I.4}$$

with $\tau_n=T_z$ and $\tau_v=v$ (3x1 column vectors). For piezoelectric materials the corresponding eight-component vector is defined

$$\boldsymbol{\tau} = \begin{bmatrix} \boldsymbol{T_z} \\ D_3 \\ \boldsymbol{v} \\ j\omega\phi \end{bmatrix} = \begin{bmatrix} \boldsymbol{\tau_n} \\ \boldsymbol{\tau_v} \end{bmatrix} \tag{I.5}$$

with $\tau_n=[\ T_z\ \ D_3\ ]^t$ and $\tau_v=[\ v\ \ j\omega\phi\ ]^t$, and the superscript "t" indicating transpose, such that τ_n and τ_v are 4x1 column vectors. The differential equation at ω radians/second describing transverse, or z, variations in the sinusoidal steady-state for the material is given by

$$\frac{d\boldsymbol{\tau}}{dz} = j\omega\boldsymbol{A}\boldsymbol{\tau} \tag{I.6}$$

where the system matrix **A** is a function of the phase velocity v_p and of material constants rotated to the coordinate system of Fig. I.1. For multilayer problems, (I.6) must be satisfied in each material and τ must be continuous at each interface. The matrix **A** is given by

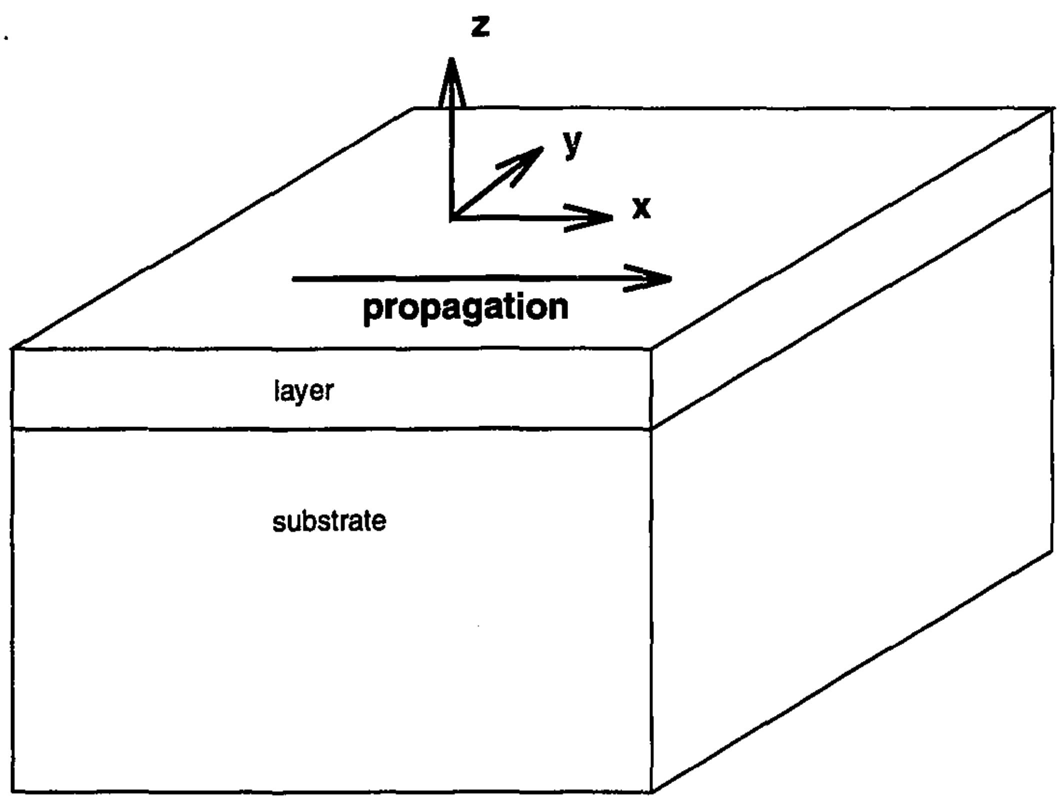

Fig. I.1 Structure considered and coordinate system.

$$
\boldsymbol{A} = \begin{bmatrix} \dfrac{\boldsymbol{\Gamma}^{13}\boldsymbol{X}}{v_p} & G_0 - \dfrac{(\boldsymbol{\Gamma}^{11} - \boldsymbol{\Gamma}^{13}\boldsymbol{X}\boldsymbol{\Gamma}^{31})}{v_p^2} \\ \\ \boldsymbol{X} & \dfrac{\boldsymbol{X}\boldsymbol{\Gamma}^{31}}{v_p} \end{bmatrix} \tag{I.7}
$$

where the submatrices **X** and Γ in the case of **non-piezoelectric** materials are 3x3 containing, respectively, compliance and stiffness constants referred to the coordinate system of Fig. I.1; and the submatrix $\mathbf{G}_0=\rho\mathbf{I}_{3x3}$, with ρ the mass density of the material and $\mathbf{I}_{3x3}$ the 3x3 identity matrix. For **piezoelectric** materials the submatrices **X** and Γ are 4x4 and contain compliance, stiffness, piezoelectric, and permittivity constants; $\mathbf{G}_0$ is also 4x4 having zeros in the fourth row and column. The submatrices **X**, **Γ**, and $\mathbf{G}_0$ are given by

$$
\boldsymbol{\Gamma}^{ik} = \begin{bmatrix} c_{1i1k} & c_{1i2k} & c_{1i3k} & e_{k1i} \\ c_{2i1k} & c_{2i2k} & c_{2i3k} & e_{k2i} \\ c_{3i1k} & c_{3i2k} & c_{3i3k} & e_{k3i} \\ e_{i1k} & e_{i2k} & e_{i3k} & -\epsilon_{ik} \end{bmatrix} \tag{I.8}
$$

$$
\boldsymbol{X} = (\boldsymbol{\Gamma}^{33})^{-1} \tag{I.9}
$$

$$
G_0 = \begin{bmatrix} \rho & 0 & 0 & 0 \\ 0 & \rho & 0 & 0 \\ 0 & 0 & \rho & 0 \\ 0 & 0 & 0 & 0 \end{bmatrix} \tag{I.10}
$$

The solution to (I.6) can be written

$$
\begin{aligned} \boldsymbol{\tau}(z+d_h) &= \exp(j\omega\boldsymbol{A}d_h)\,\boldsymbol{\tau}(z) = \\ &= \boldsymbol{U}\exp(\Lambda d_h)\,\boldsymbol{U}^{-1}\boldsymbol{\tau}(z) \end{aligned} \tag{I.11}
$$

with $\Phi_T=\exp(j\omega\mathbf{A}d_h)$ the material state transition matrix that maps τ across a distance d_h in the z direction within the same material, **U** the 8x8 modal matrix of the jω**A** material matrix (the columns of $\mathbf{U}$ are the eigenvectors of $j\omega\mathbf{A}$), Λ is the diagonal eigenvalue matrix of ($j\omega\mathbf{A}$), and $\bar{\tau}=\mathbf{U}^{-1}\tau$ is the normal mode or uncoupled state vector.

The boundary conditions require that at mechanically free surfaces $\mathbf{T}_z$ vanishes, and for piezoelectric materials with electrically open-circuited surfaces the electric fields must satisfy Laplace's equation in the free space. For short-circuited surfaces the potential must be zero or a constant. The solution for D_3(free space) is given by $\varepsilon_o\omega\phi/v_p$ and using "$D_3'=D_3-D_3$(free space)" as the forth element of τ in formulating the boundary condition equations, since $D_3'=0$, the first four components of τ must vanish at an open-circuited condition. For SAW problems, and considering that the half-space occupies $z<0$, all fields must vanish as z goes to negative infinity. For the substrate, since only four of the eigenvalues decay with depth, it follows that at a semi-infinite substrate surface the state vector is

$$\tau(0) = U_{Sp}\,\overline{\tau_u}(0) \qquad \text{(I.12)}$$

where $\mathbf{U}_{Sp}$ is the 8x4 submatrix of $\mathbf{U}_S$ corresponding to decaying modes of the substrate and $\bar{\tau}_u$ is the corresponding 4x1 half of the normal state vector $\bar{\tau}$, with the "u" index indicating upper half. From the previous considerations (using D_3' as the forth element of τ), for an open-circuited top surface

$$\begin{bmatrix} 0 \\ 0 \\ 0 \\ 0 \\ v \\ j\omega\phi \end{bmatrix} = \Phi_T\,\tau(0) \qquad \text{(I.13)}$$

Selecting the first four equations and using (I.11), one can write $\mathbf{0}=\{\Phi_T\tau(0)\}_u=\{\Phi_T\mathbf{U}_{Sp}\bar{\tau}_u(0)\}_u$, with the subscript "u" indicating upper half as before. This equation has non-trivial solutions only if $\det[(\Phi_T\mathbf{U}_{Sp})_u]=0$, which is the boundary conditions (BC) determinantal equation for the multilayer on half-space type of problem. For the pure half-space SAW problem, the boundary determinant equation is directly obtained from the previous statement as

$$\det\left[\,(\boldsymbol{U}_{Sp})_u\right] = 0 \tag{I.14}$$

For the short-circuited surface instead of using the equation with D_3', one uses the fact that ϕ=0 at the surface. The resultant numerical procedure consists in searching for v_p such that the boundary conditions, expressed by (I.14), are satisfied.

As mentioned before in this appendix, all the other variables can be expressed in terms of the six (non-piezoelectrics, equation (I.4)) or eight (piezoelectrics, equation (I.5)) variables chosen. For the fields in the direction of propagation, x direction, the vector τ_p is defined and its relation with τ given by

$$\boldsymbol{\tau}_p = \begin{bmatrix} T_{11} \\ T_{12} \\ T_{13} \\ D_1 \end{bmatrix} = \begin{bmatrix} \boldsymbol{\Gamma}^{13}\boldsymbol{X} & \dfrac{\boldsymbol{\Gamma}^{13}\boldsymbol{X}\boldsymbol{\Gamma}^{31} - \boldsymbol{\Gamma}^{11}}{v_p} \end{bmatrix} \begin{bmatrix} \boldsymbol{\tau}_n \\ \boldsymbol{\tau}_v \end{bmatrix} = \boldsymbol{p}\ \boldsymbol{\tau} \tag{I.15}$$

For the fields in the direction normal to the propagation on the surface, y direction, the vector τ_h is defined and its relation with τ given by

$$\boldsymbol{\tau}_h = \begin{bmatrix} T_{12} \\ T_{22} \\ T_{23} \\ D_2 \end{bmatrix} = \begin{bmatrix} \boldsymbol{\Gamma}^{23}\boldsymbol{X} & \dfrac{\boldsymbol{\Gamma}^{23}\boldsymbol{X}\boldsymbol{\Gamma}^{31} - \boldsymbol{\Gamma}^{21}}{v_p} \end{bmatrix} \begin{bmatrix} \boldsymbol{\tau}_n \\ \boldsymbol{\tau}_v \end{bmatrix} = \boldsymbol{h}_t\ \boldsymbol{\tau} \tag{I.16}$$

where both matrices **p** and $\mathbf{h}_t$ defined in (I.15) and (I.16), respectively, are 4x8 for piezoelectric materials and are functions of material constants and phase velocity only. For non-piezoelectric materials, $\tau_p=T_x=[\ T_{11}\ T_{12}\ T_{13}\ ]^t$ and $\tau_h=T_y=[\ T_{12}\ T_{22}\ T_{23}\ ]^t$, and **p** and $\mathbf{h}_t$ are 3x6.

APPENDIX II

In this appendix the $\Gamma_{Taniso}=\Gamma^{11}-\Gamma^{13}X\Gamma^{31}$ 3x3 matrix which allows the calculation of the Tiersten Boundary Condition for an anisotropic overlay is given. This matrix is the anisotropic equivalent to equation (2.14), Chapter II. This expression was obtained using commercially available software (Maple V, Maple is a registred trademark of Waterloo Maple Software, Waterloo, Ontario, Canada).

$$
\begin{aligned}
&GammaTaniso = \\
&\Big[c11 + \big(c15^2\,c44\,c33 - c15^2\,c34^2 - 2\,c15\,c14\,c45\,c33 + 2\,c15\,c14\,c35\,c34 \\
&\quad + 2\,c15\,c13\,c45\,c34 - 2\,c15\,c13\,c35\,c44 + c14^2\,c55\,c33 - c14^2\,c35^2 \\
&\quad - 2\,c14\,c13\,c55\,c34 + 2\,c14\,c13\,c45\,c35 + c13^2\,c55\,c44 - c13^2\,c45^2\big)/(\%1), \\
&c16 + \big(c56\,c15\,c44\,c33 - c56\,c15\,c34^2 - c56\,c14\,c45\,c33 + c56\,c14\,c35\,c34 \\
&\quad + c56\,c13\,c45\,c34 - c56\,c13\,c35\,c44 - c46\,c15\,c45\,c33 + c46\,c15\,c35\,c34 \\
&\quad + c46\,c14\,c55\,c33 - c46\,c14\,c35^2 - c46\,c13\,c55\,c34 + c46\,c13\,c45\,c35 \\
&\quad + c36\,c15\,c45\,c34 - c36\,c15\,c35\,c44 - c36\,c14\,c55\,c34 + c36\,c14\,c45\,c35 \\
&\quad + c36\,c13\,c55\,c44 - c36\,c13\,c45^2\big)/(\%1), 0\Big] \\
&\Big[c16 + \big(c56\,c15\,c44\,c33 - c56\,c15\,c34^2 - c56\,c14\,c45\,c33 + c56\,c14\,c35\,c34 \\
&\quad + c56\,c13\,c45\,c34 - c56\,c13\,c35\,c44 - c46\,c15\,c45\,c33 + c46\,c15\,c35\,c34 \\
&\quad + c46\,c14\,c55\,c33 - c46\,c14\,c35^2 - c46\,c13\,c55\,c34 + c46\,c13\,c45\,c35 \\
&\quad + c36\,c15\,c45\,c34 - c36\,c15\,c35\,c44 - c36\,c14\,c55\,c34 + c36\,c14\,c45\,c35 \\
&\quad + c36\,c13\,c55\,c44 - c36\,c13\,c45^2\big)/(\%1), c66 - \big(-c56^2\,c44\,c33 + c56^2\,c34^2 \\
&\quad + 2\,c56\,c46\,c45\,c33 - 2\,c56\,c46\,c35\,c34 - 2\,c56\,c36\,c45\,c34 \\
&\quad + 2\,c56\,c36\,c35\,c44 - c46^2\,c55\,c33 + c46^2\,c35^2 + 2\,c46\,c36\,c55\,c34 \\
&\quad - 2\,c46\,c36\,c45\,c35 - c36^2\,c55\,c44 + c36^2\,c45^2\big)/(\%1), 0\Big] \\
&[0, 0, 0]
\end{aligned}
$$

$$\%1 := -c55\,c44\,c33 + c55\,c34^2 + c45^2\,c33 - 2\,c45\,c35\,c34 + c35^2\,c44$$

REFERENCES

[1] Lord Rayleigh, "On waves propagating along the plane surface of an elastic solid," in *Proc. London Math. Soc.,* vol. 7, pp. 4-11, Nov. 1885.

[2] A. E. H. Love, *Some problems in geodynamics,* Cambridge University Press , London, 1911, 1926.

[3] R. Stoneley, "Elastic waves at the surface of separation of two solids," *Roy. Soc. Proc. London,* series A 106, 416 (1924).

[4] B. A. Auld, "Rayleigh wave propagation," in *Rayleigh-Wave Theory and Application,* vol. 2, E. A. Ash and E. G. S. Paige, Ed., *Springer series on Wave phenomena,* Leopold B. Felsen, Ed., Germany, Springer-Verlag Berlin Heidelberg, 1985, pp. 12-28.

[5] M. F. Lewis, "On Rayleigh waves and related propagating acoustic waves," in Rayleigh-Wave Theory and Application, vol. 2, E. A. Ash and E. G. S. Paige, Ed., *Springer series on Wave phenomena,* Leopold B. Felsen, Ed., Germany, Springer-Verlag Berlin Heidelberg, 1985, pp. 37-58.

[6] R. M. White and F. W. Voltmer, "Direct piezoelectric coupling to surface elastic waves," *Appl. Phys. Lett.,* vol. 17, pp. 314-316, 1965.

[7] T. C. Lim and G. W. Farnell, "Search for forbidden directions of elastic surface-wave propagation in anisotropic crystals," *Journal of Applied Physics,* vol. 39, no. 9, pp. 4319-4325, August 1968.

[8] G. W. Farnell, "Properties of elastic surface waves," *Physical Acoustics,* vol. 6, W. P. Mason and R. N. Thurston, Ed., New York, Academic Press, 1970, pp. 109-166.

[9] G. W. Farnell and E. L. Adler, "Elastic wave propagation in thin layers," *Physical Acoustics,* vol. 9, W. P. Mason and R. N. Thurston, Ed., New York, Academic Press, 1972, pp. 35-127.

[10] J. J. Campbell and W. R. Jones, "A method for estimating optimal crystal cuts and propagation directions for excitation of piezoelectric surface waves," *IEEE Trans. on Sonics and Ultrason.,* vol. su-15, no. 4, October 1968.

[11] C. K. Campbell, "Applications of surface acoustic and shallow bulk acoustic wave devices," *Proc. of the IEEE,* vol. 77, no. 10, October 1989.

[12] D. P. Morgan, "Rayleigh wave transducers," in *Rayleigh-Wave Theory and Application*, vol. 2, E. A. Ash and E. G. S. Paige, Ed., *Springer series on Wave phenomena*, Leopold B. Felsen, Ed., Germany, Springer-Verlag Berlin Heidelberg, 1985, pp. 60-77.

[13] R. H. Tancrell and M.G. Holland, "Acoustic surface wave filters," *Proc. of the IEEE*, vol. 59, no. 3, March 1971, pp. 393-409.

[14] W. R. Smith, H. M. Gerard, J. H. Collins, T. M. Reeder, and H.J. Shaw, "Analysis of interdigital surface wave transducers by use of an equivalent circuit model," *IEEE Trans. on Micr. Theory and Tech.*, vol. MTT-17, no. 11, November 1969, pp. 856-864.

[15] D. A. Leedom, R. Krimholtz, and G. L. Matthaei, "Equivalent circuits for transducers having arbitrary even- or odd-symmetry piezoelectric excitation," *IEEE Trans. on Sonics and Ultrason.,* vol. su-18, no. 3, July 1971.

[16] R. F. Milsom, N. H. C. Reilly, and Martin Redwood, "Analysis of generation and detection of surface and bulk acoustic waves by interdigital transducers," *IEEE Trans. on Sonics and Ultrason.,* vol. su-24, no. 3, May 1977.

[17] C. S. Hartmann, "Systems impact of modern Rayleigh wave technology," in *Rayleigh-Wave Theory and Application*, vol. 2, E. A. Ash and E. G. S. Paige, Ed., *Springer series on Wave phenomena*, Leopold B. Felsen, Ed., Germany, Springer-Verlag Berlin Heidelberg, 1985, pp.238-253.

[18] T. P. Cameron, J. C. B. Saw, and M.S. Suthers, "Applications of SAW technology in a SONET-compatible high capacity digital microwave radio," in *Proc. IEEE Ultrason. Symp.,* 1992, pp. 237-240.

[19] P. V. Wright, "A review of saw resonator filter technology," in *IEEE Ultrason. Symp.,* 1992, pp. 29-43.

[20] C. C. W. Ruppel, R. Dill, A. Fischerauer, G. Fischerauer, W. Gawlik, J. Machui, F. Muller, L. Reindl, W. Ruile, G. Scholl, I. Schropp, and K. Ch. Wagner, "Saw devices for consumer communication applications," *IEEE Trans. on Ultrason.*

Ferroelec. Freq. Contr., vol. 40, no. 5, September 1993, pp. 438-452.

[21] Several papers, in *Proc. IEEE Ultrason. Symp.*, 1993, pp. 59-142.

[22] H. Gautier and C. Maerfeld, "Current applications and trends of SAW components in France," in *Proc. IEEE Ultrason. Symp.*, 1988, pp. 67-75.

[23] Y. Ebata and H. Satoh, "Current applications and future trends for SAW in Asia," in *Proc. IEEE Ultrason. Symp.*, 1988, pp. 195-202.

[24] J. Heighway and D. P. Morgan, "1991 and beyond: the current status and future trends for SAW in Europe," in *Proc. IEEE Ultrason. Symp.*, 1991, pp. 217-223.

[25] T. C. Lim and G. W. Farnell, "Character of pseudo surface waves on anisotropic crystals," *The Journal of the Acoustic Society of America*, April 1969, vol. 45, No. 4, pp. 845-851.

[26] K. Yamanouchi and M. Takeuchi, "Applications for piezoelectric leaky surface waves," in *Proc. IEEE Ultrason. Symp.*, 1990, pp. 11-18.

[27] C. S. Hartmann, P. V. Wright, R. J. Kansy, and E. M. Garber, "An analysis of saw interdigital transducers with internal reflections and the application to the design of single-phase unidirectional transducers," in *Proc. IEEE Ultrason. Symp.*, 1982, pp. 40-45.

[28] P.V. Wright, "The natural single- phase unidirectional transducer: a new low-loss SAW transducer," in *Proc. IEEE Ultrason. Symp.*, 1985, pp. 58-63.

[29] T. Kojima and K. Shibayama, "An analysis of an equivalent circuit model for an interdigital surface-acoustic-wave transducer," *Japan. Jour. of Appl. Phys.*, vol. 27, suppl. 27-1, pp. 163-165, 1988.

[30] D. F. Thompson and P. V. Wright, "Wide bandwidth NSPUDT coupled resonator filter design," in *Proc. IEEE Ultrason. Symp.*, 1991, pp. 181-184.

[31] T. Thorvaldsson, "Analysis of the natural single phase unidirectional transducer," in *Proc. IEEE Ultrason. Symp.*, 1989, pp. 91-96.

[32] T. Thorvaldsson and B.P. Abbott, "Low loss SAW filter utilizing the natural single phase unidirectional transducer (NSPUDT)," in *Proc. IEEE Ultrason. Symp.*, 1990, pp. 43-48.

[33] C. S. Hartmann, J. C. Andle and M. B. King, "Saw notch filters," in *Proc. IEEE*

Ultrason. Symp., 1987, pp. 131-138.

[34] C. S. Lam and D. Gunes, "A low-loss SAW filter using two-finger per wavelength electrodes on the NSPUDT orientation of Quartz," in *Proc. IEEE Ultrason. Symp.*, 1993, pp. 185-188.

[35] B.A. Auld, *Acoustic Fields and Waves in Solids*, vols. I & II, Robert E. Krieger Publishing Company, Malabar, Florida, 1990, 2nd. edition.

[36] M. Pereira da Cunha and E. L. Adler, "Scattering of SAW at discontinuities: some numerical experiments," in *Proc. IEEE Ultrason. Symp.*, 1993, pp. 89-94.

[37] H. F. Tiersten, "Elastic surface waves guided by thin films," *J. App. Phys.*, vol. 40, no. 2, 1969, pp. 770-789.

[38] S. Datta and B. J. Hunsinger, "First-order reflection coefficient of surface acoustic waves from thin-strip overlays," *J. Appl. Phys.*, vol. 50, no. 9, September 1979, pp. 5661-5665.

[39] R. C. M. Li and J. Melgainlis, "Second order effects in SAW devices due to stored energy at step discontinuities," in *Proc. IEEE Ultrason. Symp.*,1973, pp. 503-505.

[40] R. C. M. Li and J. Melngailis, "The influence of stored energy at step discontinuities on the behaviour of surface-wave gratings," *IEEE Trans. on Sonics and Ultrasonics*, vol. SU-22, no. 3, May 1975, pp. 189-198.

[41] W. J. Tanski, "Developments in resonators on quartz," in *Proc. IEEE Ultrason. Symp.*, 1977, pp. 900-904.

[42] W. R. Shreve, "Surface wave resonator and their use in narrowband filters," in *Proc. IEEE Ultrason. Symp.*, 1976, pp. 706-713.

[43] T. Thorvaldsson and F.M. Nyffeler, "Rigorous derivation of the Mason equivalent circuit parameters from the coupled mode theory," in *Proc. IEEE Ultrason. Symp.*, 1986, pp. 91-96.

[44] H. Shimizu and M. Takeuchi, "Theoretical studies of the energy storage effects and the second harmonic responses of the SAW reflection gratings," in *Proc. IEEE Ultrason. Symp.*, 1979, pp. 667-672.

[45] S. Datta and B. J. Hunsinger, "An analysis of energy storage effects on SAW propagation in periodic arrays," *IEEE Trans. on Sonics and Ultrasonics*, vol. SU-

27, no. 6, Nov. 1980, pp. 333-341.

[46] H. Robinson and Y. Hahn, "A comprehensive analysis of surface-acoustic-wave reflections. II. Second-order effects," *J. Appl. Phys.*, vol. 68, no. 9, Nov. 1990, pp. 4426-4437.

[47] C. M. Panasik and B. J. Hunsinger, "Scattering matrix analysis of surface acoustic wave reflectors and transducers," *IEEE Trans. on Sonics and Ultrasonics,* vol. SU-28, no. 2, Mar. 1981, pp. 79-91.

[48] K. Inagawa and M. Koshiba, "Equivalent networks for SAW interdigital transducers," *IEEE Trans. on Ultrason. Ferroelec. Freq. Contr.*, vol. 41, no. 3, May 1994, pp. 402-411.

[49] M. Koshiba and S. Mitobe, "Equivalent network for SAW gratings," *IEEE Trans. on Ultrason. Ferroelec. Freq. Contr.*, vol. 35, no. 5, Sep.1988, pp. 531-535.

[50] G. W. Farnell, "Surface wave reflectors and resonators," *Canadian Elec. Eng. J.*, vol. 1, no. 3, pp. 3-13, 1976.

[51] O. Schwelb, E. L. Adler, and J. Slaboszewicz, "Modelling, simulation and design of SAW grating filters," *IEEE Trans. Ultrason. Ferroelec. Freq. Contr.*, vol. UFFC-37, no. 3, pp. 205-214, May 1990.

[52] E. L. Adler, M. Pereira da Cunha, O. Schwelb, "Network model versus COM description of SAW devices," in *Proc. IEEE Ultrason. Symp.*, 1990, pp. 19-24.

[53] M. Pereira da Cunha and E. L. Adler, "A network model for arbitrarily oriented IDT structures," in *Proc. IEEE Ultrason. Symp.*, 1992, pp. 89-94.

[54] K. Nakamura and K. Hirota, "Equivalent circuits for directional SAW-IDT's based on the coupling-of-modes theory," in *Proc. IEEE Ultrason. Symp.*, 1993, pp. 215-218.

[55] R. Sorrentino, Ed., *Numerical Methods for Passive Microwave and Millimeter Wave Structures*, New York: IEEE Press, 1989, pp. 301-351.

[56] M. Pereira da Cunha and E.L. Adler, "A Network Model for Arbitrarily Oriented IDT Structures," *IEEE Trans. Ultrason. Ferroelec. Freq. Contr.*, vol. UFFC-40, no. 6, november 1993, pp. 622-629.

[57] E. L. Adler, M. Pereira da Cunha, and O. Schwelb, "Arbitrarily oriented SAW

gratings: network model and the coupling-of-modes description," *IEEE Trans. Ultrason. Ferroelec. Freq. Contr.*, vol. UFFC-38, no. 3, pp. 220-230, May 1991.

[58] W. J. Tanski and H. van der Vaart, "The design of SAW resonators on quartz with emphasis on two ports," in *Proc. IEEE Ultrason. Symp.*, 1976, pp. 2

[59] P. S. Cross and R. V. Schmidt, "Coupled SAW resonators, " Bell Syst. Tech. J., vol. 56, Oct. 1977, pp. 1447-1482.

[60] D. P. Chen and H. A. Haus, "Analysis of metal-strip SAW gratings and transducers," *IEEE Trans. Sonics Ultrason.*,vol. SU-32, no. 3, pp. 395-408, May 1985.

[61] E. Akçakaya, "A new analysis of single-phase unidirectional transducers," *IEEE Trans. Ultrason. Ferroelec. Freq. Contr.*, vol. UFFC-34, no. 1, pp. 45-52, Jan. 1987.

[62] P. V. Wright, "Analysis and design of low-loss SAW devices with internal reflections using coupling of modes theory," in *Proc. IEEE Ultrason. Symp.*, 1989, pp. 141-152.

[63] Z. H. Chen and K. Yamanouchi, "Theoretical analysis of relations between directivity of SAW transducer and its dispersion curves," in *Proc. IEEE Ultrason. Symp.*, 1989, pp. 71-74.

[64] G. Scholl et al., "Efficient design tools for SAW resonator filters," in *Proc. IEEE Ultrason. Symp.*, 1989, pp. 135-140.

[65] T. Aoki and K.A. Ingebrigtsen, "Equivalent circuit parameters of interdigital transducers derived from dispersion relations for surface acoustic waves in periodic metal gratings," *IEEE Trans. on Sonics and Ultrason.*, vol. SU-24, no. 3, May 1977, pp. 167-178.

[66] P. V. Wright, "Low-cost high-performance resonator and coupled-resonator design: NSPUDT and other innovative structures," in *Proc. 43th Annual Symposium on Frequency Control*, May 1989, pp. 574-587.

[67] B.P. Abbott, C.S. Hartmann, D.C. Malocha, "Transduction magnitude and phase for COM modeling of SAW Devices," *IEEE Trans. Ultrason. Ferroelec. Freq. Contr.*, vol. UFFC-39, no. 1, Jan. 1992, pp. 54-60.

[68] K. Hashimoto and M. Yamaguchi, "Derivation of coupling-of-modes parameters for SAW device analysis by means of boundary element method," in *Proc. IEEE Ultrason. Symp.*, 1991, pp. 21-26.

[69] M. Pereira da Cunha, "Desenvolvimento de convolutores elásticos empregando tecnologia de ondas acústicas superficiais," M.E. Thesis Dept. of Eletrical Eng., Escola Politécnica da Universidade de São Paulo, São Paulo, Brazil, 1989, (in portuguese).

[70] D.P. Morgan, *Surface wave devices for signal processing*, Elsevier, Amsterdam, 1985.

[71] F. G. Marshall, C. O. Newton, and E. G. S. Paige, "Theory and design of the surface acoustic wave multistrip coupler," *IEEE Trans. on Microwave Theory and Techniques*, vol. MTT-21, no.4, pp. 206-215, April 1973.

[72] F. G. Marshall, C. O. Newton, and E. G. S. Paige, "Surface acoustic wave multistrip components and their applications," *IEEE Trans. on Microwave Theory and Techniques*, vol. MTT-21, no.4, pp. 216-224, April 1973.

[73] C. Maerfeld and G. W. Farnell, "Nonsymmetrical multistrip coupler as a surface wave beam compressor of large bandwidth,"*Electronics Letters*, vol. 9, no.18, pp. 432-434, 1973.

[74] R. V. Schmidt and L. A. Coldren, "Thin film acoustic surface waveguides on anisotropic media," *IEEE Trans. on Sonics and Ultrason.*, vol. SU-22, no. 2, March 1975, pp. 115-122.

[75] H. F. Tiersten and R. C. Smythe, "Guided acoustic surface wave filters," *Appl. Phys. Lett.*, vol. 28, pp. 111-113, 1976.

[76] T. Kodama, H. Kawabata, Y. Yasuhara, and H. Sato, "Design of low-loss SAW filters employing distributed acoustic reflection transducers," in *Proc. IEEE Ultrasonics Symp.*, 1986, pp. 59-64.

[77] M. Lewis, "SAW filters employing interdigitated interdigital transducers, IIDT," in *Proc. IEEE Ultrasonics Symp.*, 1982, pp. 12-17.

[78] Z. H. Chen, M. Takeuchi, K. Yamanouchi, "Analysis of the film thickness dependence of a single-phase unidirectional transducer using the coupling-of-

modes theory and the finite-element method," *IEEE Trans. Ultrason. Ferroelec. Freq. Contr.*, vol. UFFC-39, n° 1, pp. 82-94, january 1992.

[79] A.R. Baghai-Wadji, H. Reichinger, H. Zidek, Ch. Mecklenbräuker, "Green's Function Applications in SAW Devices," in *Proc. IEEE Ultrason. Symp.*, 1991, pp. 11-20.

[80] H. Robinson and Y. Hahn, "A comprehensive analysis of surface-acoustic-wave reflections. III. Oblique incidence grooved and metallic gratings," *J. Appl. Phys.*, vol. 71, no. 6, March 1992, pp. 2536-2548.

[81] C. S. Hartmann, D. P. Chen, J. Heighway, "Experimental determination of COM model parameters for SAW transversely coupled resonator filter," in *Proc. IEEE Ultrason. Symp.*, 1992, pp. 211-214.

[82] W. P. Mason, *Electromechanical transducers and wave filters*, second ed., Princeton, N.J., D. van Nostrand, 1948, pp. 185-209 and 399-412.

[83] C. Campbell, *Surface acoustic wave devices and their signal processing applications*, Academic Press, CA, USA, 1989.

[84] G. Carlotti, D. Fioretto, L. Giovannini, F. Nizzoli, G. Socino, and L. Verdini, "Brillouin scattering by pseudosurface acoustic modes on $(1\bar{1}1)$ GaAs," *Journal of Physics: Condensed Matter,* 1992, Vol. 4, pp. 257-262.

[85] N. F. Naumenko, "Quasihorizontal polarized quasibulk acoustic surface waves piezoelectric crystals," *Sov. Phys. Crystallogr.*, Vol. 37, No. 2, March-April 1992, pp. 220-223.

[86] E. L. Adler, "SAW and Pseudo-SAW properties using matrix methods," *1992 IEEE Ultrasonics Symposium Proceedings,* Vol. 1, IEEE cat. No. 92CH3118-7, pp. 455-460.

[87] T. I. Browning and M. F. Lewis, "New family of bulk-acoustic-wave devices employing interdigital transducers," *Electronics Letters,* March 1977, Vol. 13, No. 5, pp. 128-130.

[88] K. A. Ingebrigtsen, "Surface Waves in Piezoelectrics," *J. App. Phys.,* Vol. 40, No. 7, 1969, pp. 2681-2686.

[89] M. Feldmann and J. Hénaff, "Surface acoustic waves for signal processing," *Artech House,* 1989, Boston, USA.

[90] L. Boyer, J. Desbois, Y. Zhang, J. M. Hodé, "Theoretical determination of the pseudo surface acoustic characteristic parameters," in *Proc. IEEE Ultrason. Symp.,* 1991, pp. 353-358.

[91] K. Hashimoto and M. Yamaguchi, "Effective electromechanical coupling to leaky SAW on 36° YX-$LiTaO_3$," *Japanese Journal of Applied Physics,* Vol. 26(1987), Supplement 26-1, pp. 159-161.

[92] V. P. Plessky and T. Thorvaldsson, "Rayleigh waves and leaky SAWs in periodic systems of electrodes: periodic Green functions analysis," *Electronics Letters,* July 1992, Vol. 28, No. 14, pp. 1317-1319.

[93] Y. Zhang, J. Desbois, L. Boyer, "New method to characterize the surface-generated bulk acoustic waves in piezoelectric substrates," *J. Acoust. Soc. Am.,* Vol. 92, No. 5, 1992, pp. 2499-2508.

[94] C. A. Flory and R. L. Bauer, "Surface transverse wave mode analysis and coupling to interdigital transducers," 1987 *IEEE Ultrasonics Symposium Proceedings,* Vol. 1, IEEE cat. No. 87CH2492-7, pp. 313-318.

[95] E. L. Adler, "Matrix Methods Applied to Acoustic Waves in Multilayers," *IEEE Trans. Ultrason. Ferroelec. Freq. Contr.,* Vol. UFFC-37, No 6, pp. 485-490, November 1990.